

A NUMERICAL MODEL OF GAS-DRIVEN
DYNAMIC FRACTURES WITH AN APPLICATION
TO BOREHOLE STIMULATION

BY

JEFFERY M. ROBERTS
B.S. Emporia State University

A MASTER'S THESIS

submitted in partial fulfillment of the
requirement for the degree

MASTER OF SCIENCE

Department of Mechanical Engineering
KANSAS STATE UNIVERSITY
Manhattan, Kansas

1988

APPROVED BY:



Major Professor

ACKNOWLEDGEMENTS

Before all other acknowledgements should come my thanks to my wife, Cheryl. She has helped me through my experiences in the military and graduate school. The support I received from her has been indispensable.

Other graduate students have also been very important. I would like especially to thank Mark James and Shung Lung Su for their technical assistance and, most important of all, their friendship.

Thanks should be given to Dr. Paul Miller of the Mechanical Engineering Department and George Lea of the National Science Foundation for the financial support received for this project (NSF grant EET-8708823).

Finally, I thank Daniel Swenson, my major professor, for the patience and technical expertise he shared with me.

TABLE OF CONTENTS

1.0 - INTRODUCTION.	1
1.1 - Experimental Data	4
1.2 - Existing Analysis	5
1.3 - Objectives and Scope.	6
 2.0 - FINITE DIFFERENCE GAS DYNAMICS	
2.1 - Governing Equations	8
2.2 - Crack Tip Boundary Condition.	14
2.3 - Crack Mouth Boundary Condition.	15
2.4 - Loss Mechanisms	16
2.5 - Finite Difference Approximation	18
2.5.1 - Stability	19
2.6 - Burn Model.	20
 3.0 - GAS_SOLVE	24
3.1 - Gas Parameters.	24
3.2 - GAS_SOLVE	27
 4.0 - VERIFICATION PROBLEMS	
4.1 - Burn Model.	29
4.2 - Shock Tube Problem.	29
4.3 - Simplified Crack Problem.	37

5.0 - APPLICATIONS.	43
5.1 - Case 1 - Specified Borehole Pressure With No Losses in the Fracture.	47
5.2 - Case 2 - Specified Borehole Pressure With Friction, Heat Transfer, and Seepage Included.	61
5.3 - Case 3 - Specified Borehole Pressure With Friction in the Fracture Included($\epsilon = 20\mu\text{m}$)	68
5.4 - Case 4 - Specified Borehole Pressure With Friction in the Fracture Included($\epsilon = 4\mu\text{m}$).	79
5.5 - Case 5 - Burn Model With Friction, Heat Transfer, and Seepage included.	91
6.0 - CONCLUSIONS AND RECOMMENDATIONS	
6.1 - Conclusions	105
6.2 - Recommendations	106

LIST OF TABLES

4.1	Burn Model Verification Parameters.	32
4.2	Verification Problems	38
5.1	Material Properties for Sandstone	45
5.2	Parameters Used in Gas Model.	46

LIST OF FIGURES

1.1	Stimulation of Naturally Fractured Reservoirs (After Schmidt et al., 1981).	2
2.1	Differential Element for Conservation of Mass	9
2.2	Differential Element for Conservation of Energy	9
2.3	Differential Element for Conservation of Momentum	12
2.4	Control Volume for Crack Tip Boundary Condition	12
2.5	Graphical Representation of Stability (After Press et al., 1986).	21
2.6	Web Thickness and Route of Burning Through a Mult-Perf Progressively Burning Grain (After Mniszewski and Napadensky, 1985).	23
3.1	Sample of Gas Parameters Page	25
3.2	The GAS_SOLVE subroutine.	28
4.1	Closed Bomb Test Results (After Mniszewski and Napadensky, 1985).	30
4.2	Numerical Results of Closed Bomb Test	31
4.3	Shock Tube $t = 0$ (After Sod, 1978) Shock Tube $t > 0$	34
4.4	Pressure Profile of Riemann Problem Using Lax Method.	35
4.5	Density Profile of Riemann Problem Using Lax Method	36
4.6	Velocity Profile of Riemann Problem Using Lax Method.	36
4.7	Profiles for Verification Case 1 a. Pressure b. Velocity.	39
4.8	Profiles for Verification Case 2 a. Pressure b. Velocity.	40

4.9	Profiles for Verification Case 3	
	a. Pressure	
	b. Velocity.	42
5.1	Model Geometry.	44
5.2	Assumed Dynamic Stress Intensity for Sandstone.	44
5.3	Borehole Time Histories	
	a. Pressure	
	b. Temperature	48
5.4	Displaced Mesh Results for Case 1 at 12 msec.	49
5.5	Crack Opening Displacement for Case 1 at 12 msec.	50
5.6	Crack Length for Case 1	51
5.7	Crack Velocity for Case 1	53
5.8	KID During Propagation for Case 1	54
5.9	KIID During Propagation for Case 2.	55
5.10	Gas Velocity for Case 1 at 6.5, 9.5, and 12 msec.	56
5.11	Gas Temperature for Case 1 at 6.5, 9.5, and 12 msec	56
5.12	Gas Pressure for Case 1 at 6.5, 9.5, and 12 msec.	57
5.13	Gas Density for Case 1 at 6.5, 9.5, and 12 msec	58
5.14	Mach Number for Case 1 at 6.5, 9.5, and 12 msec	58
5.15	Normal Stress along Crack Face at 12 msec	59
5.16	Crack Entrance Energy for Case 1.	60
5.17	Energy Required to Perform Boundary Work for Case 1 (Initialized at 45.7E7 J).	62
5.18	Energy Present in Gas for Case 1.	63
5.19	Crack Opening Displacement for Case 2 at 12 msec.	64
5.20	Crack Length for Case 2	65
5.21	Displaced Mesh Results for Case 2 at 12 msec.	66

5.22	Crack Entrance Energy for Case 2.	67
5.23	Heat Transfer Results for Case 2 at 6.5, 9.5, and 12 msec	69
5.24	Seepage Results for Case 2 at 6.5, 9.5, and 12 msec . .	69
5.25	Gas Pressure for Case 2 at 6.5, 9.5, and 12 msec. . . .	70
5.26	Gas Velocity for Case 2 at 6.5, 9.5, and 12 msec. . . .	71
5.27	Gas Temperature for Case 2 at 6.5, 9.5, and 12 msec . .	71
5.28	Gas Density for Case 2 at 6.5, 9.5, and 12 msec	72
5.29	Mach Number for Case 2 at 6.5, 9.5, and 12 msec	72
5.30	KID During Propagation for Case 2	73
5.31	Crack Length for Case 3	74
5.32	KID During Propagation for Case 3	75
5.33	Displaced Mesh Results for Case 3 at 12 msec.	76
5.34	Crack Velocity for Case 3	77
5.35	Crack Entrance Energy for Case 3.	78
5.36	Gas Pressure for Case 3 at 6.5, 9.5, and 12 msec. . . .	80
5.37	Gas Velocity for Case 3 at 6.5, 9.5, and 12 msec. . . .	81
5.38	Gas Temperature for Case 3 at 6.5, 9.5, and 12 msec . .	81
5.39	Gas Density for Case 3 at 6.5, 9.5, and 12 msec	82
5.40	Mach Number for Case 3 at 6.5, 9.5, and 12 msec	82
5.41	Displaced Mesh Results for Case 4 at 12 msec.	83
5.42	Crack Length for Case 4	84
5.43	Crack Opening Displacement for Case 4 at 12 msec. . . .	85
5.44	KID During Propagation for Case 4	86
5.45	Crack Velocity for Case 4	87

5.46	Gas Pressure for Case 4 at 6.5, 9.5, and 12 msec. . . .	88
5.47	Gas Velocity for Case 4 at 6.5, 9.5, and 12 msec. . . .	89
5.48	Gas Temperature for Case 4 at 6.5, 9.5, and 12 msec . .	89
5.49	Gas Density for Case 4 at 6.5, 9.5, and 12 msec	90
5.50	Mach Number for Case 4 at 6.5, 9.5, and 12 msec	90
5.51	Crack Entrance Energy for Case 4.	92
5.52	Displaced Mesh Results for Case 5 at 12 msec.	93
5.53	Crack Opening Displacement for Case 5 at 12 msec. . . .	94
5.54	Crack Length for Case 5	95
5.55	Borehole Pressure History Using Burn Model.	96
5.56	Crack Velocity for Case 5	97
5.57	KID During Propagation for Case 5	98
5.58	Gas Pressure for Case 5 at 6.5, 9.5, and 12 msec. . . .	99
5.59	Heat Flux for Case 5 at 6.5, 9.5, and 12 msec	100
5.60	Mach Number for Case 5 at 6.5, 9.5, and 12 msec	100
5.61	Gas Density for Case 5 at 6.5, 9.5, and 12 msec	101
5.62	Gas Seepage for Case 5 at 6.5, 9.5, and 12 msec	101
5.63	Gas Velocity for Case 5 at 6.5, 9.5, and 12 msec. . . .	102
5.64	Gas Temperature for Case 5 at 6.5, 9.5, and 12 msec . .	102
5.65	Crack Entrance Energy for Case 5.	104

NOMENCLATURE

ρ = density, Kg/m³

u = one dimensional velocity, m/sec

w = crack opening displacement, m

v = gas seepage velocity normal to crack, m/sec

e = specific energy, J/m³

C_v = constant volume specific heat, J/Kg-K

\dot{m} = mass flow rate, Kg/sec

P = gas pressure, Pa

q'' = heat transfer into crack wall, W/m²

T = temperature, K

f = fanning friction factor

σ = stress, Pa

k = permeability, m²

Φ = porosity

μ = viscosity, kg/m-sec

t = time, sec

Pr = Prandtl number

α = thermal diffusivity, m²/sec

K_t = thermal conductivity, J/m-K-sec

ϵ = fracture roughness, m

Re = Reynolds number

n = burn rate exponent

NOMENCLATURE

B = burn rate constant, m/sec-Pa^{-n}

D = propellant web thickness, m

C = propellant covolume, m^3/Kg

F = propellant energy density, J/Kg

$K_{I,II}$ = stress intensity factors, $\text{Pa}\sqrt{\text{m}}$

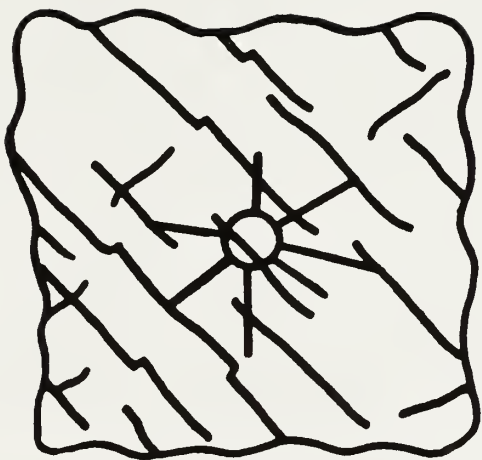
CHAPTER 1

INTRODUCTION

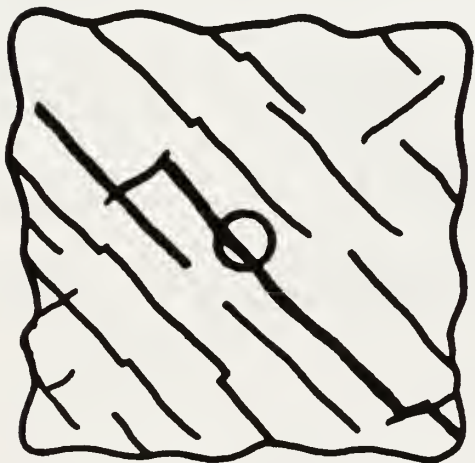
Oil and gas wells have been stimulated using explosives since the late 1800's. Early efforts tended to emphasize the potential of high explosives placed in the wellbore to create an almost instantaneous source of high pressure gas resulting in fractures around the borehole.

Unfortunately, using explosives may result in creating an intensely damaged zone near the borehole that is only rarely associated with the long, radial fractures required for successful stimulation. A simple explanation is when detonation occurs, nearby rock may yield and plastically deform. When the stress wave passes, the rock unloads elastically. This leaves an increased borehole diameter and a residual stress field, sometimes called a stress cage, which is compressive near the borehole. The existence of residual stress regions around boreholes that have been subjected to explosive detonations is a well-documented phenomenon (Schmidt, et al., 1981). Some of these observations have been made as a result of field experiments at the Nevada Test Site by Sandia National Laboratories.

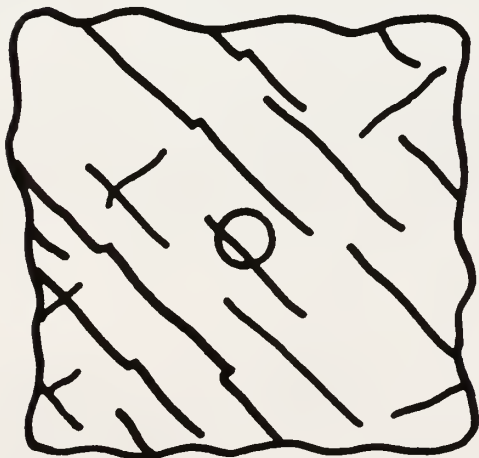
Multiple fractures are highly desirable in formations which have naturally occurring fractures such as Devonian shale. This can be seen in Figure 1.1. The production from the unstimulated well depends primarily on the number of fractures intersected during drilling. Hydraulic fracturing typically produces a single fracture that is likely to run parallel to most of the existing fractures since its orientation is governed by in-situ stresses that probably also govern



DYNAMIC FRACTURING



HYDRAULIC FRACTURING



NO STIMULATION

Figure 1.1: Stimulation of Naturally Fractured Reservoirs
(After Schmidt et al., 1981)

the pattern of the natural fractures. The advantage of multiple fractures is that although they may not extend as far as a hydraulic fracture, they may connect the well to naturally occurring fractures.

An alternative to explosives is to tailor the pressure-time behavior of the explosive or a suitable propellant so as to keep the peak pressure and the loading rate below the level that would result in a stress cage. Unfortunately, the combination of loading parameters that will produce optimal multiple fracturing and avoid the formation of a stress cage is not well known.

When compared to conventional hydraulic fracturing, tailored-pulse loading has several possible advantages. Hydraulic fractures, which are propagated at pressures that are slightly higher than the minimum in-situ stress and pumping times that are on the order of hundreds of seconds to hours, typically produce only a single fracture whose orientation is perpendicular to the minimum principal stress. The higher wellbore pressures, which are achieved in tailored-pulse loading, are needed to drive cracks in less favorable directions with respect to the in-situ stresses in order to produce multiple fractures.

In addition, tailored-pulse loading with propellants is likely to produce little formation damage due to the interaction of the working fluids with the rock. Little water is produced by these propellant materials, and the products have very little time to react with the rock. Some hydraulic fracturing fluids, however, can cause swelling of the rock. Economic considerations may also make the techniques more feasible since igniting an explosive or a propellant charge in a well can be relatively inexpensive. Very little equipment

or time may be required when compared to even a small hydraulic fracture job.

If tailored pulse loading is to be successful, the fractures generated must extend a significant distance from the wellbore. It has been estimated (Jean-Claude Rogiers, 1987) that lengths on the order of 100-200 meters are required. Alternatively, if the procedure is used only as a clean up tool for damaged boreholes, much shorter lengths would be acceptable.

1.1 Experimental Data

Experiments relating to the multi-fracturing process have either been full field experiments or scaled down laboratory tests. At the Sandia National Laboratories, Schmidt et al. (1981) performed a series of five full-scale tests to evaluate various multi-fracture concepts. The tests were conducted at the Nevada Test Site in horizontal boreholes drilled from a tunnel in ash-fall tuff.

Various propellants and explosives were tested. After the shots, the rock was mined back along the borehole which allowed direct observation of the fracture patterns. Sandia's results led to a better understanding of the pressure loading rates required for successful stimulation. It should be noted that no field tests have observed fractures greater than about 10 meters.

Previous laboratory work on multiple radial fracturing is not extensive, because of the difficulties of working with realistic energy sources on a lab scale and making appropriate pressure measurements and fracture observations. Through laboratory scale tests it has been shown that multiple fractures do occur under proper

conditions. This can be seen in Swift et al. (1981), and Fourney et al. (1981, 1983). However, small scale experiments are not adequate to address the fundamental problem of crack length.

1.2 Existing Analysis

The most complete gas model that has been developed with the gas-driven fracture problem in mind is the work of Nilson and Griffiths [Nilson, et al., (1985, 1986), Griffiths, et al., (1986)]. In their approach, similarity solutions are obtained for the problem of a planar gas-driven fracture propagating into a brittle elastic solid. Local values of the fluid pressure, temperature and speed are computed from the one-dimensional mass, momentum and energy equation governing the turbulent flow of a ideal gas. The equations used are very similar to the ones that will be derived in Chapter 2. Crack opening displacements and the stress intensity at the crack tip are calculated from the gas pressure distribution, in accordance the quasi-steady integral relations from linear/elastic fracture mechanics.

The geometry is presumed to be either planar or axisymmetric. The appropriate assumption depends on the relative length of the fractures compared to the pressurized length of the borehole. Opening displacements are calculated from the theory of linear elasticity (Sneddon and Lowengrub, 1969) using the following quasi-steady formula:

$$w(x) = \frac{4(1-\nu)}{\pi G} \int_x^L \int_0^\xi \frac{P(\zeta) - \sigma}{(\xi^2 - \zeta^2)^{1/2}} \left(\frac{R+\zeta}{R+\xi} \right) d\zeta \frac{\xi d\xi}{(\xi^2 - x^2)^{1/2}}$$

where P is the internal pressure which varies along the fracture, R is the radius of the cavity, G and ν are the shear modulus and Poisson's ratio, and σ is the in-situ stress acting normal to the plane of the fracture. The aperture, w , at any given location, x , depends upon the entire pressure distribution along the fracture.

The stress intensity at the tip of the fracture also depends upon the pressure loading everywhere along the fracture. Propagation occurs when the stress intensity factor reaches the critical value. The propagation may be viewed as an equilibrium process, in which the stress intensity is maintained at the critical value as the fracture propagates.

Nilson, in the above described work, leaves out inertia terms in the conservation of momentum equation. Swenson and Taylor (1983) developed a finite element code that uses a smeared crack approach. This model doesn't have the capability to model gas flow in the fracture. CRACKER (Swenson, 1985) allows the crack to be a distinct part of the mesh, with finite elements on both sides of the crack face. This allows a clean implementation of fracture mechanics concepts. However, the pressure distribution along the crack face is not known. Therefore a pressure profile is assumed.

1.3 Objectives and Scope

The primary objective of this thesis is to develop a fully coupled dynamic model of gas-driven fractures and then to use this model to address the fundamental question of maximum obtainable crack lengths. This will allow a more realistic evaluation of tailored pulse loading. In addition, the model of gas-driven dynamic fracture

provides a general tool to be used in other areas such as rock blasting and containment of nuclear blasts. This objective was met by coupling a model of compressible gas flow to an existing finite element code which models dynamic fracture (Swenson, 1985). The program, including the modifications made for this thesis, is completely menu driven with preprocessing, analysis, and postprocessing available to the user.

The remainder of this thesis is arranged in five chapters. Chapter 2 shows the derivation of all equations and the implementation into finite difference form. Chapter 3 is a discussion on the subroutine GAS_SOLVE and some of the interactive features available. Chapter 4 briefly describes the problems used to verify the model. Chapter 5 outlines the results found and Chapter 6 gives some conclusions and recommendations for future work.

CHAPTER 2

FINITE DIFFERENCE GAS DYNAMICS

2.1 Governing Equations

Consider the elemental control volume shown in Figure 2.1. We can derive the continuity equation by doing a mass balance on this element. For this analysis we will assume compressible, one dimensional unsteady flow. There will be no property variations in the direction perpendicular to flow. The mass entering the left face of the element per unit time is:

$$\rho u w \quad (2.1)$$

where ρ is the density, u is the one dimensional velocity, and w is the crack opening displacement. The mass leaving the right face of the element per unit time is:

$$\rho u w + \frac{\partial(\rho u w)}{\partial x} dx \quad (2.2)$$

The mass leaving the top and bottom faces of the element per unit time is:

$$2\rho v dx \quad (2.3)$$

where v is the seepage velocity.

The time rate of change of mass inside the element is:

$$\frac{\partial(\rho w)}{\partial t} dx = (w \frac{\partial \rho}{\partial t} + \rho \frac{\partial w}{\partial t}) dx \quad (2.4)$$

where $\frac{\partial w}{\partial t}$ is the crack opening velocity. A mass balance on this system yields the conservation of mass equation:

$$\frac{\partial \rho}{\partial t} = - \frac{1}{w} \left\{ \frac{\partial(\rho u w)}{\partial x} + 2\rho v + \rho \frac{\partial w}{\partial t} \right\} \quad (2.5)$$

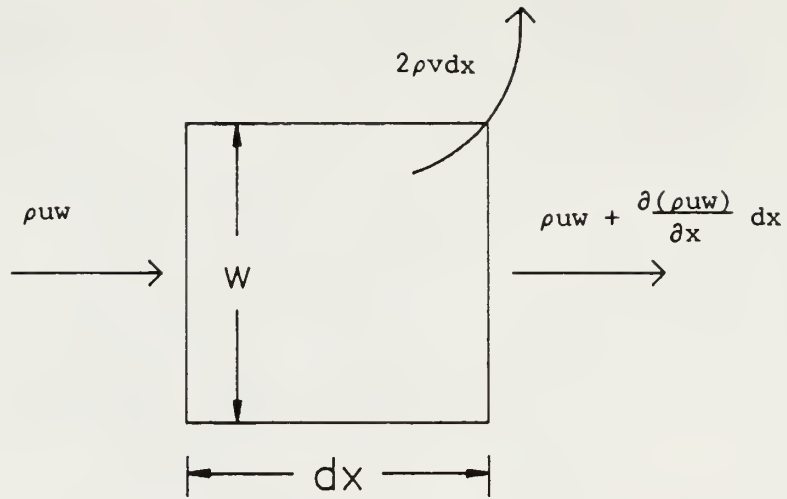


Figure 2.1: Differential Element for Conservation of Mass

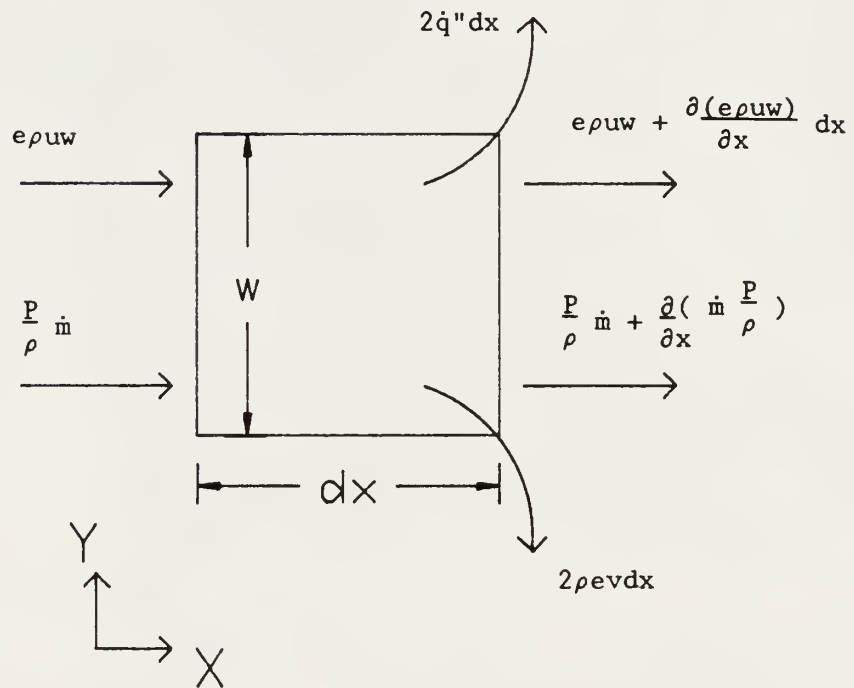


Figure 2.2: Differential Element for Conservation of Energy

Using the elemental control volume shown in Figure 2.2 the conservation of energy equation is derived. We will assume constant viscosity, thermal conductivity, and specific heats. Then, for the element shown, the energy balance may be written: Energy convected in left face - energy convected out the

top and bottom faces + net work done on the element
- energy convected out the right face = time rate of change
of energy in the element

The energy entering the left face per unit time is:

$$e\rho uw \quad (2.6)$$

where $e = C_v T + \frac{u^2}{2}$, T is the temperature, and C_v is the constant volume specific heat. The flow work done on the left face can be found in the following manner:

The volume flow rate (Q) = $\frac{\dot{m}}{\rho}$

The velocity (u) = $\frac{Q}{A} = \frac{\dot{m}}{\rho w}$

The force applied on the left face = Pw

The flow work per unit time (\dot{W}) is the product of the force exerted and the velocity:

$$\dot{W} = \frac{\dot{m}}{\rho w} (Pw) = \frac{\dot{m}}{\rho} P \quad (2.7)$$

The energy leaving the right face of the element per unit time:

$$e\rho uw + \frac{\partial(e\rho uw)}{\partial x} dx \quad (2.8)$$

The flow work done on the right face per unit time is:

$$\dot{m} \frac{P}{\rho} + \frac{\partial}{\partial x} \left(\dot{m} \frac{P}{\rho} \right) \quad (2.9)$$

Energy leaving the top and bottom faces, due to seepage, per unit time is:

$$2e\rho v dx \quad (2.10)$$

Time rate of change of energy inside the element:

$$\frac{\partial(Ew)}{\partial t} dx = (w \frac{\partial E}{\partial t} + E \frac{\partial w}{\partial t}) dx$$

where $E = e\rho$. The work done to expand the crack and by friction:

$$\dot{W} = -P \frac{\partial w}{\partial t} dx + 2\tau Au \quad (2.11)$$

Writing the energy balance corresponding to the quantities shown in Figure 2.3 yields the conservation of energy equation:

$$-\frac{1}{w} \left\{ \frac{\partial(uw(E + P))}{\partial x} + (E + P)\dot{w} + 2v(E + P) + 2\dot{q}'' - 2\tau Au \right\} = \frac{\partial E}{\partial t} \quad (2.12)$$

where \dot{q}'' is the heat transfer into the crack wall.

Doing the same type of analysis on the element shown in Figure 2.3 we can find an expression for the conservation of momentum.

The force balance on the element is:

$$\Sigma F = \text{increase in momentum flux} + \text{rate of change of momentum in the element}$$

The momentum flux in the x direction is the product of the mass flow through a particular side of the control volume and the x component of velocity at that point. The mass entering the left face of the element per unit time is:

$$\rho uw \quad (2.13)$$

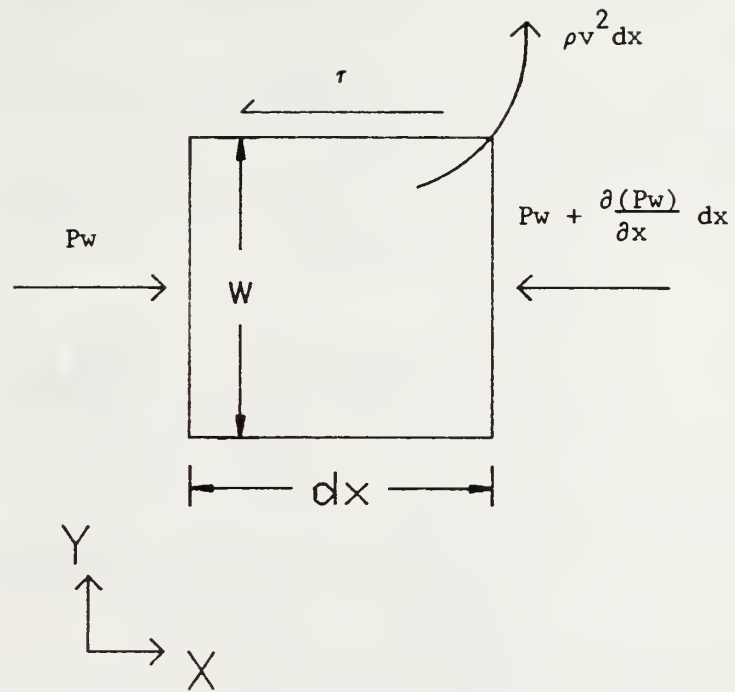


Figure 2.3: Differential Element for Conservation of Momentum

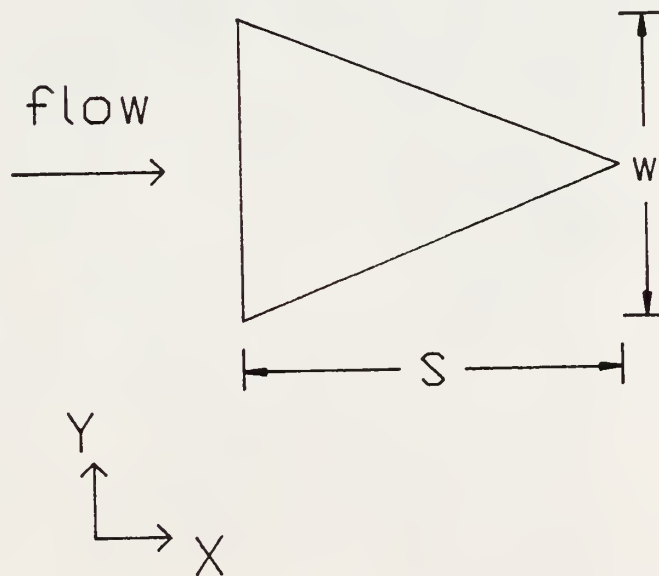


Figure 2.4: Control Volume for Crack Tip Boundary Condition

if we assume a unit depth in the z direction. Thus the momentum entering the left face per unit time is:

$$(\rho u w)u = \rho u^2 w \quad (2.14)$$

The momentum leaving the right face per unit time is:

$$\rho u^2 w + \frac{\partial(\rho u^2 w)}{\partial x} dx \quad (2.15)$$

The momentum leaving the top and bottom faces per unit time is:

$$2\rho u v \, dx \quad (2.16)$$

NOTE: In the computer coding, Eq 2.16 was incorrectly coded as $2\rho u^2$.

For the conditions considered in this thesis, it was determined that this error was inconsequential.

By defining a fanning type friction factor to be:

$$f = \frac{\tau}{.5\rho u^2} \quad (2.17)$$

where τ is the shear stress on the top and bottom sides, we can find the force applied as a result of this shear stress:

$$F_s = \tau \times (\text{area}) = \left(\frac{1}{2} \rho u^2 f\right) 2dx = f\rho u^2 dx \quad (2.18)$$

The force resulting from the pressure on the left face is:

$$Pw \quad (2.19)$$

The force resulting from the pressure on the right face is:

$$Pw + \frac{\partial(Pw)}{\partial x} dx \quad (2.20)$$

Therefore, the sum of all forces being considered is:

$$\Sigma F = \left(-f\rho u^2 - \frac{\partial(Pw)}{\partial x} \right) dx \quad (2.21)$$

Then, by doing a force and momentum balance on the element, we find the conservation of momentum equation:

$$\begin{aligned}
- \frac{1}{w} \left\{ \frac{\partial(Pw)}{\partial x} + f\rho u^2 + \frac{\partial(\rho u^2 w)}{\partial x} + 2\rho uv \right. \\
\left. + \rho u \frac{\partial w}{\partial t} \right\} = \frac{\partial(\rho u)}{\partial t}
\end{aligned} \tag{2.22}$$

2.2 Crack Tip Boundary Condition

To derive the equations for the crack tip a slightly different approach is used. The control volume used is shown in Figure 2.4. The volume is assumed to be a wedge with $V = \frac{1}{2} ws$ and $\dot{V} = \frac{1}{2} (w\dot{s} + s\dot{w})$, where s is the length of the volume and w is the crack opening displacement. The momentum entering the control volume is:

$$\rho u^2 w \tag{2.23}$$

The mass leaving the volume through seepage is:

$$2\rho vs \tag{2.24}$$

A mass balance on the control volume yields:

$$V \frac{\partial \rho}{\partial t} = \rho u^2 w - 2\rho vs - \rho \frac{\partial V}{\partial t} \tag{2.25}$$

For the conservation of energy equation we first need to find the flow work and energy crossing the boundary. The flow work in is:

$$\frac{\dot{m}}{\rho} P \tag{2.26}$$

The work done to expand the volume is:

$$P \frac{\partial V}{\partial t} \tag{2.27}$$

The conservation of energy expression, therefore, is:

$$\begin{aligned}
V \frac{\partial(e\rho)}{\partial t} = (E + P)uw + f\rho u^2 sw - (P + E) \frac{\partial V}{\partial t} \\
- 2s\dot{q}'' - 2\rho sv(E + P)
\end{aligned} \tag{2.28}$$

For the conservation of momentum expression we need to know the momentum entering and leaving the volume per unit time:

$$(\rho u w)u - (\rho v w)v \quad (2.29)$$

and the net force acting on the volume:

$$(P_{in} - P_n) \frac{w}{2} - f \rho u^2 s \quad (2.30)$$

where P_n is the pressure found at the crack tip node.

The conservation of momentum equation for the crack tip volume is therefore:

$$V \frac{\partial(\rho u)}{\partial t} = \frac{w}{2} (P - P_n) - f \rho u^2 w - \rho u \frac{\partial(\rho u)}{\partial t} \quad (2.31)$$

2.3 Crack Mouth Boundary Condition

At the mouth of the crack, the high pressure gas in the borehole expands and enters the crack. At any time, the current conditions in the borehole and in the crack mouth are known. The task is to predict the flow rate into the crack during the next time step. The difficulty is that the pressure, velocity, and density of the gas entering the crack are not the same as the conditions in the crack and that this state cannot be chosen arbitrarily.

To solve this problem, we pose the crack mouth conditions as a Riemann problem. In the Riemann problem, a diaphragm separates two gases at different states. When the diaphragm is ruptured, a shock wave and rarefaction wave propagate through the gases (See Chapter 4 for an example solution). The solution then provides a complete definition of the gas conditions passing the ruptured diaphragm (crack mouth).

At each time step in the analysis, the conditions in the borehole and in the crack mouth are known. A Riemann problem is solved using these conditions. The solution provides the state of the gas entering the borehole during the next time step. This is then repeated for each time step.

2.4 Loss Mechanisms

Seepage loss, heat transfer, and friction expressions follow the approach given by Nilson et al., (1985). The lateral seepage loss into the wall rock is estimated with a one dimensional (normal to the rock wall) Darcy flow-analysis:

$$v = \frac{(P - P_{\infty})}{\sqrt{t}} \left[\frac{k \Phi}{P \mu} \right] \quad (2.32)$$

where P is the local gas pressure in the fracture, P_{∞} is the ambient pore pressure, t is the time the crack face has been exposed to gas, k is the permeability, Φ is the porosity, and μ is the viscosity.

Heat transfer to the permeable wall rock is approximated by the expression:

$$q'' = \frac{T - T_{\infty}}{R_{\text{conv}} + R_{\text{cond}}} \quad (2.33)$$

where T is the local gas temperature in the fracture, T_{∞} is the ambient temperature of the rock, R_{conv} is the resistance to heat transfer by convection, and R_{cond} is the resistance to heat transfer by conduction. R_{conv} is estimated from:

$$R_{\text{conv}} = \frac{4Pr^{2/3}}{f\rho C_p u} \quad (2.34)$$

where Pr is the Prantdl number, C_p is the constant pressure specific heat of the gas, and u is the local velocity of the gas.

The resistance to heat transfer through conduction based on a one-dimensional lateral diffusion analysis is:

$$R_{\text{cond}} = \frac{(\alpha \pi t)^{1/2}}{k_t} \quad (2.35)$$

where α is the thermal diffusivity, k_t is the thermal conductivity, and t is the time the wall is exposed to the gas.

The frictional effects for both turbulent and laminar flow are incorporated into a single expression:

$$f = \frac{12}{Re} + 0.055 \left(\frac{\epsilon}{w} \right)^{0.472} \quad (2.36)$$

where Re is the Reynolds number $\left(\frac{\rho \mu w}{u} \right)$, μ is the gas viscosity, and ϵ is the fracture roughness. During low Re for laminar flow, the first term is predominant. During high Re for turbulent flow the second term becomes predominant with a smooth transition between the two extremes.

A Sutherland viscosity model used for air is used to estimate the viscosity of the gas (Schlichting, 1968):

$$\frac{\mu}{\mu_o} = \left[\frac{T}{T_o} \right]^{3/2} \frac{T_o + S_1}{T + S_1} \quad (2.37)$$

where μ_o denotes the viscosity at the reference temperature T_o , and S_1 is a constant which for air has the value $S_1 = 110$ K.

2.5 Finite Difference Approximation

Since the equations of gas dynamics are based on conservation laws, researchers in fluid mechanics have often found it useful to use a form of the equations, called the divergence form, which clearly displays the conserved quantities of mass, momentum, and energy (Ames, 1977). It would therefore seem reasonable to try to preserve these conservation properties in the finite difference approximations. A system of equations:

$$\frac{\partial \underline{w}}{\partial t} + \frac{\partial \underline{f}(\underline{w})}{\partial x} = 0 \quad (2.38)$$

where \underline{w} is a vector function (of x and t with n components) and \underline{f} is a nonlinear vector function (of the vector \underline{w} with n components) is called a system of conservation-law form. The original suggestion of Lax was a staggered scheme which, when applied to Equation 2.38, gives:

$$\frac{1}{k} \left(w_{i,j+1} - \frac{1}{2} (w_{i+1,j} + w_{i-1,j}) \right) - \frac{1}{2h} \left(f_{i+1,j} - f_{i-1,j} \right) = 0 \quad (2.39)$$

where i is the node position, j is the current time, k is the time step, and $2h$ is the distance between the $i-1$ and $i+1$ nodes.

Writing conservation Equations 2.5, 2.11, and 2.21 in this form we get (all terms on the right hand side of the following equations are at the current ,or j, time):

$$\rho_{i,j+1} = \frac{1}{2} (\rho_{i+1} + \rho_{i-1}) + \frac{\Delta t}{w} \left\{ \frac{(\rho u w)_{i-1} - (\rho u w)_{i+1}}{\Delta x} - (2v + \frac{\partial w}{\partial t}) \rho_i \right\} \quad (2.40)$$

$$\begin{aligned} \rho^u_{i,j+1} = & \frac{1}{2} (\rho^u_{i+1} + \rho^u_{i-1}) \\ & + \frac{\Delta t}{w} \left\{ \frac{(P + (\rho u)u)_{i-1} - (P + (\rho u)u)_{i+1}}{\Delta x} \right. \\ & \left. - f \rho u - 2\rho u v - \rho u \frac{\partial w}{\partial t} \right\} \end{aligned} \quad (2.41)$$

$$\begin{aligned} E_{i,j+1} = & \frac{1}{2} (E_{i+1} + E_{i-1}) \\ & + \frac{\Delta t}{w} \left\{ \frac{(uw(E + P))_{i-1} - (uw(E + P))_{i+1}}{\Delta x} \right. \\ & \left. - (P + E) \frac{\partial w}{\partial t} - 2v(E + P) - 2q'' \right\} \end{aligned} \quad (2.42)$$

2.5.1 Stability

The nodal staggering enables central space difference and forward time difference to be used without developing instability. These staggered schemes are usually stable if $(a + |v|) < \frac{h}{\Delta t}$ where a is the local sound speed and v is the local gas velocity.

In essence, the replacement of $w_{i,j}$ by the average of neighboring values in Equation 2.39 has the effect of introducing a dissipative term. The Lax scheme is thus said to have numerical dissipation, or numerical viscosity (Press et al., 1986).

For an intuitive explanation for stability, refer to Figure 2.5. The quantity $u_{i,j+1}$ is computed from information at points $i-1$ and $i+1$ at time j (or t). In other words, x_{i-1} and x_{i+1} are the boundaries of the spatial region that is allowed to communicate information to $u_{i,j+1}$. Recall that in a continuum wave equation, information actually propagates with a maximum velocity v . If the point $u_{i,j+1}$ is outside of the shaded region in Figure 2.5, then it requires information from points more distant than the differencing scheme will allow. The lack of that information will result in the instability. Therefore, Δt cannot be made too large.

The goal of recent work on finite differencing schemes is to make the discontinuities from shocks and contact surfaces more accurate. As will be discussed later, when the energy, mass, and momentum losses to be considered are added to the conservation equations, these sharp discontinuities will not be present. Because of this, the Lax method should give sufficiently accurate results.

2.6 Burn Model

The equations used for this procedure are presented from Schatz and Hanson (1986) and Mniszewski and Napadensky (1985). The mass of the propellant burned, $M(t)$, as a function of time may be expressed as:

$$M(t) = M_0 f(t) [1 + K - K f(t)] \quad (2.43)$$

where M_0 is the initial mass of propellant present in the borehole, K is the form coefficient, and $f(t)$ is the fraction of web burned as a

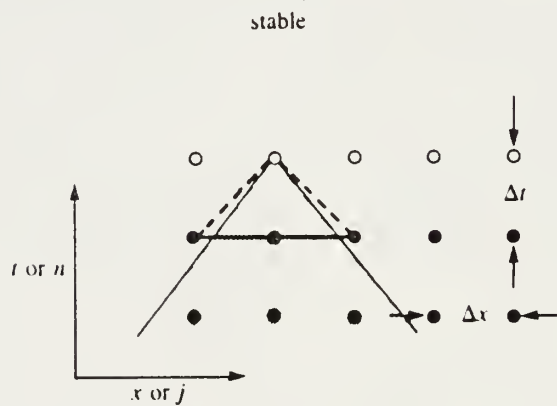
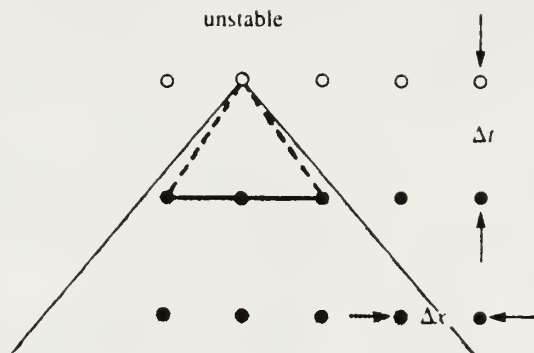


Figure 2.5: Graphical Representation of Stability
(After Press et al., 1986)

function of time. The fraction of web burned, $f(t)$, is expressed by the differential equation:

$$\frac{\partial f(t)}{\partial t} = \frac{2 B P(t)}{D}^n \quad (2.44)$$

where B is the burn rate constant, $P(t)$ is the current borehole pressure, D is the web thickness, and n is the burn rate exponent (See Figure 2.6). The mass of gas in the borehole as a function of time is:

$$M_{bh} = M(t) - M_{ck}(t) \quad (2.45)$$

where $M(t)$ is the mass of gas in the borehole if there was no loss into the crack, and $M_{ck}(t)$ is the mass lost to the crack. The net mass leaving the borehole is accumulated in the subroutine GAS_SOLVE. The borehole volume available for gas expansion is given by:

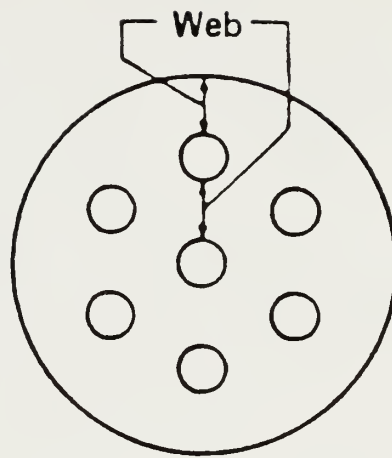
$$V_{bh} = V_i + M_o \left[\frac{1}{\rho_p} + \frac{f(t) - 1}{\rho_s} \right] \quad (2.46)$$

where V_i is the initial volume of air surrounding the propellant canister, ρ_p is the pack density, and ρ_s is the solid density. The change of volume due to expansion of the borehole was ignored.

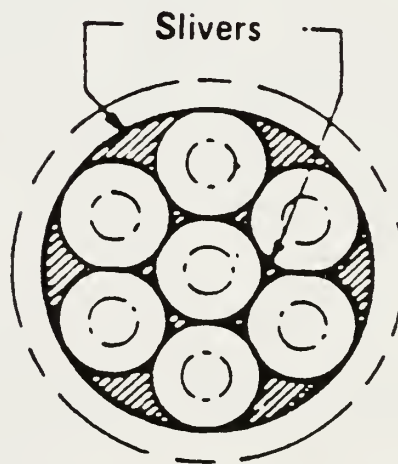
The pressure in the borehole is then found using:

$$P(t) = \frac{M_{bh}(t) F}{V_{bh}(t) - [M_{bh}(t) C]} \quad (2.47)$$

where F is the propellant energy density, and C is the covolume.



a. Unburned Grain



b. Burning Grain

Figure 2.6: Web Thickness and Route of Burning Through a Mult-Perf Progressively Burning Grain (After Mniszewski and Napadensky, 1985)

CHAPTER 3

GAS SOLVE

This chapter will describe the features available to the user to set up a gas flow problem. The Gas_Solve subroutine was incorporated into CRACKER, a finite element code used for modeling dynamic propagation of a discrete crack. CRACKER uses the finite element method to model the continuum and automatically remeshes as the crack propagates. For information on CRACKER and its uses, see Swenson (1985). Also, a description of the solving routine, Gas_Solve, will be given.

3.1 Gas Parameters

Most of the information needed to set up a gas flow problem is found in the gas parameters page. A sample (used in Case 5, Chapter 5), is shown in Figure 3.1. Every value, except the current time step, can be interactively changed by the user.

The user has the option to choose a compressible gas model, or to specify a known pressure distribution along the crack face. If the gas model is chosen, the user is prompted to choose the solution method to be used. The Lax method is currently the only solution method in use, and is illustrated.

The initial gas conditions in the crack are specified to be atmospheric conditions. The gas constants are chosen to be that of nitrogen. If the burn model option is chosen, the values describing the borehole and charge volumes, and propellant properties must be specified. Another option is to specify pressure and temperature time

```

Pressure in cracks..... = GAS MODEL

Method used to solve gas flow equations = LAX
Initial crack pressure(t=0)..... = 0.10000E+06
Initial crack temperature(t=0)..... = 0.30000E+03
Specific heat ratio (k)..... = 0.14000E+01
Ideal gas constant (R)..... = 0.29680E+03
To define borehole conditions we will use A BURN MODEL
Borehole volume..... = 0.78540E-02
Solid density..... = 0.16500E+04
Pack density..... = 0.70000E+03
Form coefficient..... = 0.62000E+00
Burn rate coefficient..... = 0.53968E-07
Burn rate exponent..... = 0.80000E+00
Covolume..... = 0.10000E-02
Web thickness..... = 0.76200E-03
Propellant energy density..... = 0.10387E+07
Charge volume..... = 0.19635E-02
Use friction model..... YES
Friction factor (F)..... = 0.10000E-01
Surface roughness..... = 0.20000E-04
Use seepage model..... YES
Permeability..... = 0.10000E-14
Porosity..... = 0.20000E-01
Reference viscosity..... = 0.18000E-04
Far field pressure(rock)..... = 0.10000E+06
Sutherland constant..... = 0.11000E+03
Reference temperature for S1..... = 0.30000E+03
Use heat transfer model..... YES
Far field temperature(rock)..... = 0.30000E+03
Conductivity..... = 0.20000E+01
Rock thermal diffusivity..... = 0.40000E-05
Time integration factor..... = 0.90000E+00
Damping factor..... = 0.80000E+00
Delta x..... = 0.30000E-01
Default crack width..... = 0.10000E-02
Current (gas) time step..... = 0.15462E-04

```

Figure 3.1: Sample of Gas Parameters Page

histories for the borehole. Examples of these are shown in Figure 5.3 (Case 2, Chapter 5). These plots are input interactively in the boundary conditions page found in CRACKER.

If the friction model is used, then Equation 2.36 will be used. If not used, then the friction factor must be specified. If the factor is zero, then no friction effects will be seen. If the factor is nonzero, then the specified constant friction factor will be used.

If the seepage model is chosen, then the values describing the rock and far field conditions must be specified. If this option is not taken, no seepage effects will be seen.

If the heat transfer model is chosen, then the values describing the rock and far field conditions must be specified. If this option is not taken, no heat transfer effects will be seen.

The time integration factor is multiplied by the calculated time step to result in the time step actually used. This reduction factor should be kept as close to one as possible to prevent smearing of the solution.

The damping factor should also be kept as close to a value of one as possible. It was found that in the early stages of a problem, the model became unstable when friction was introduced. To promote stability, the damping was introduced. For the interior cells, the damping results in $P\%$ of the new value to be added to $(1-P)\%$ of the old value. This sum will be the new value. At the inlet cell $(P-.3)\%$ is used. For this example, damping was 0.8. As will be seen in the verifications chapter, the damping has a minimal effect.

The delta x (node spacing) was chosen to be .03 meters.

If, during the course of the analysis, the crack opening displacement was found to be less than the default crack width, the displacement was set to the default. It was found that when friction was once again introduced, instabilities were a problem at the initial stages of a problem when the crack was short and closed.

3.2 GAS_SOLVE

The flow path and logic used in GAS_SOLVE is shown in Figure 3.2. The GAS_SOLVE routine is inside a larger loop in CRACKER. If new crack face surface tractions are needed, GAS_SOLVE is entered. The first time GAS_SOLVE is used, arrays are initialized which includes initializing gas conditions in the crack. Then a loop over all nodes is entered. Inside this loop all mass, momentum, and energy losses are taken care of on a node by node basis. Once all necessary calculations are finished, a comparison of the current time in GAS_SOLVE (GAS_TCURR) and CRACKER (TCURR) is performed. If GAS_TCURR is greater than TCURR, then an interpolation through time is performed, and GAS_SOLVE is exited. Otherwise, GAS_TCURR is incremented by a time step and the process is repeated.

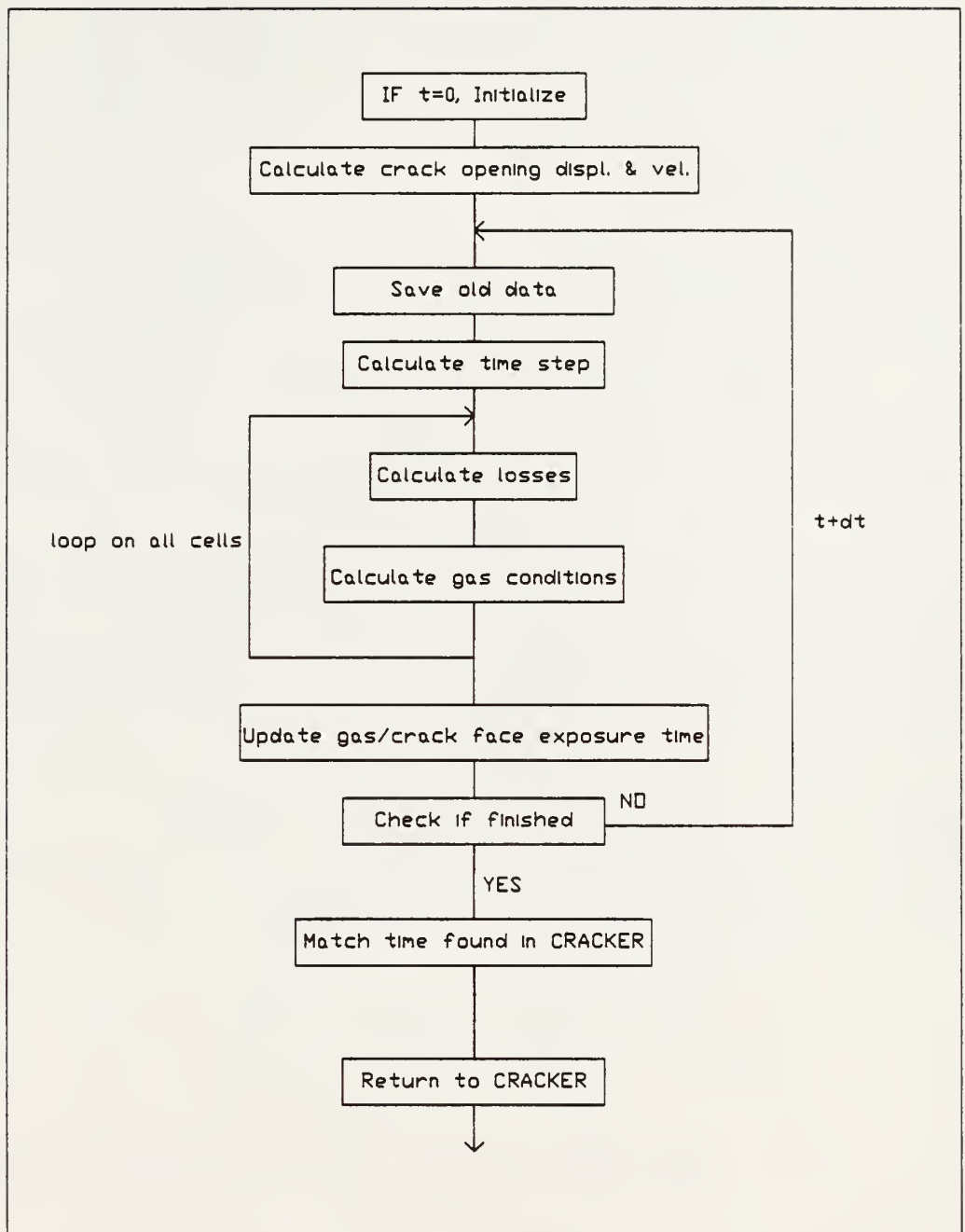


Figure 3.2: The GAS_SOLVE subroutine

CHAPTER 4

VERIFICATION PROBLEMS

4.1 Burn Model

Closed bomb tests were conducted by the Gas Research Institute (Mniszewski and Napadensky, 1985) to determine the properties of various propellants, particularly the burn rate constant and burn rate exponent. The original closed bomb test results are shown in Figure 4.1. Using these results, the burn model used in this thesis was verified. The experimentally determined values for the burn rate exponent and burn rate constant, in addition to the other quantities shown in Table 4.1, were used in the burn model. The verification results are shown in Figure 4.2. Although there is a 14 percent error when comparing the experimentally obtained peak value to the calculated peak pressure, the time at which the peak pressure occurs is in close agreement. All of the differences involved are probably the result of errors encountered when estimating the constant values from the data.

4.2 Shock Tube Problem

The differential equations were cast in finite difference form by using the Lax method. It was thought that with the simplicity gained by using this method, the first order accuracy the Lax method delivers could be accepted. To get a feeling for the accuracy lost, a typical shock tube test problem was run.

The shock tube is a useful research tool in which normal shock waves are generated. They are used in the study of materials that are

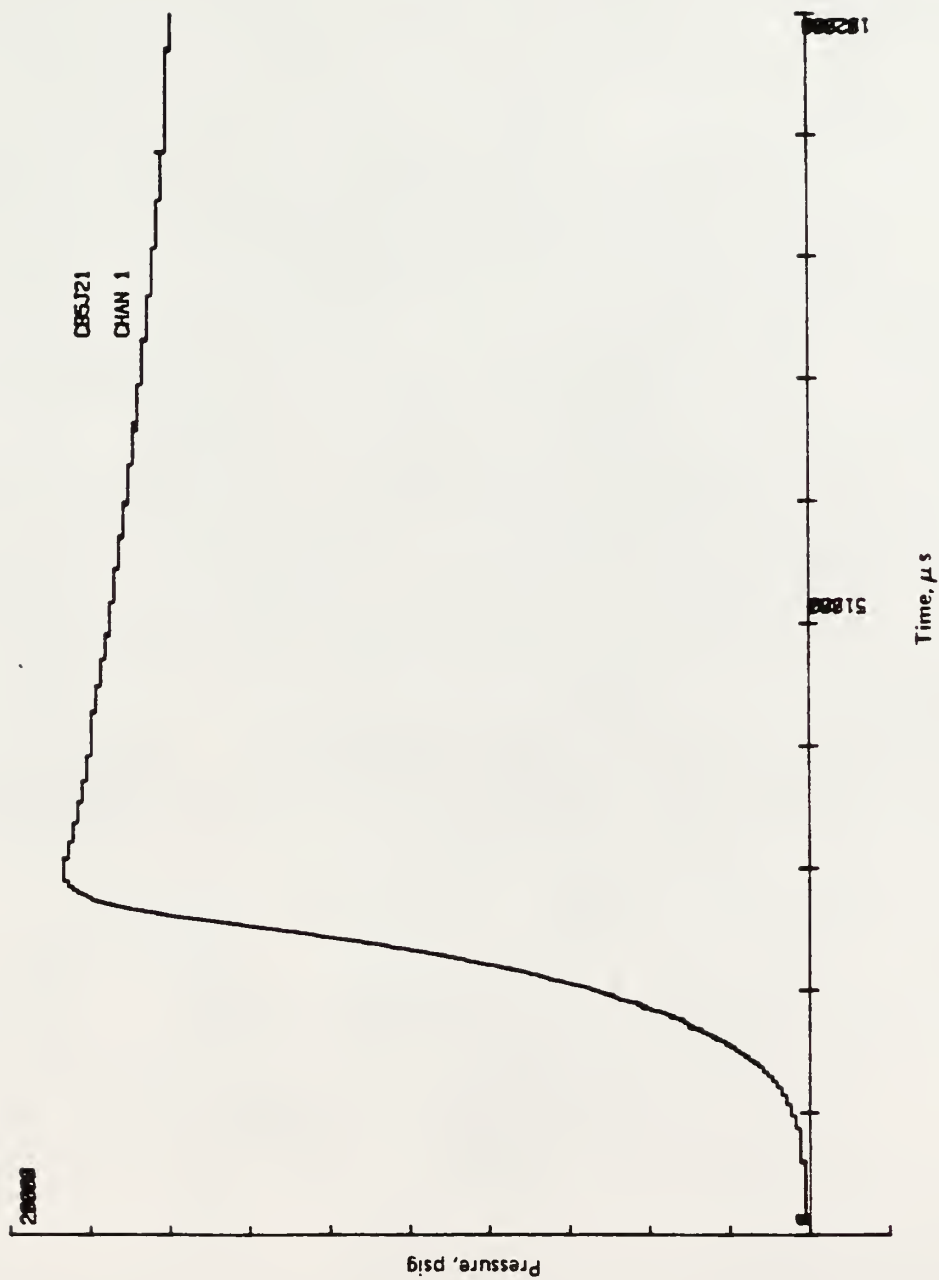


Figure 4.1: Closed Bomb Test Results (After Mniszewski and Napadensky, 1985)

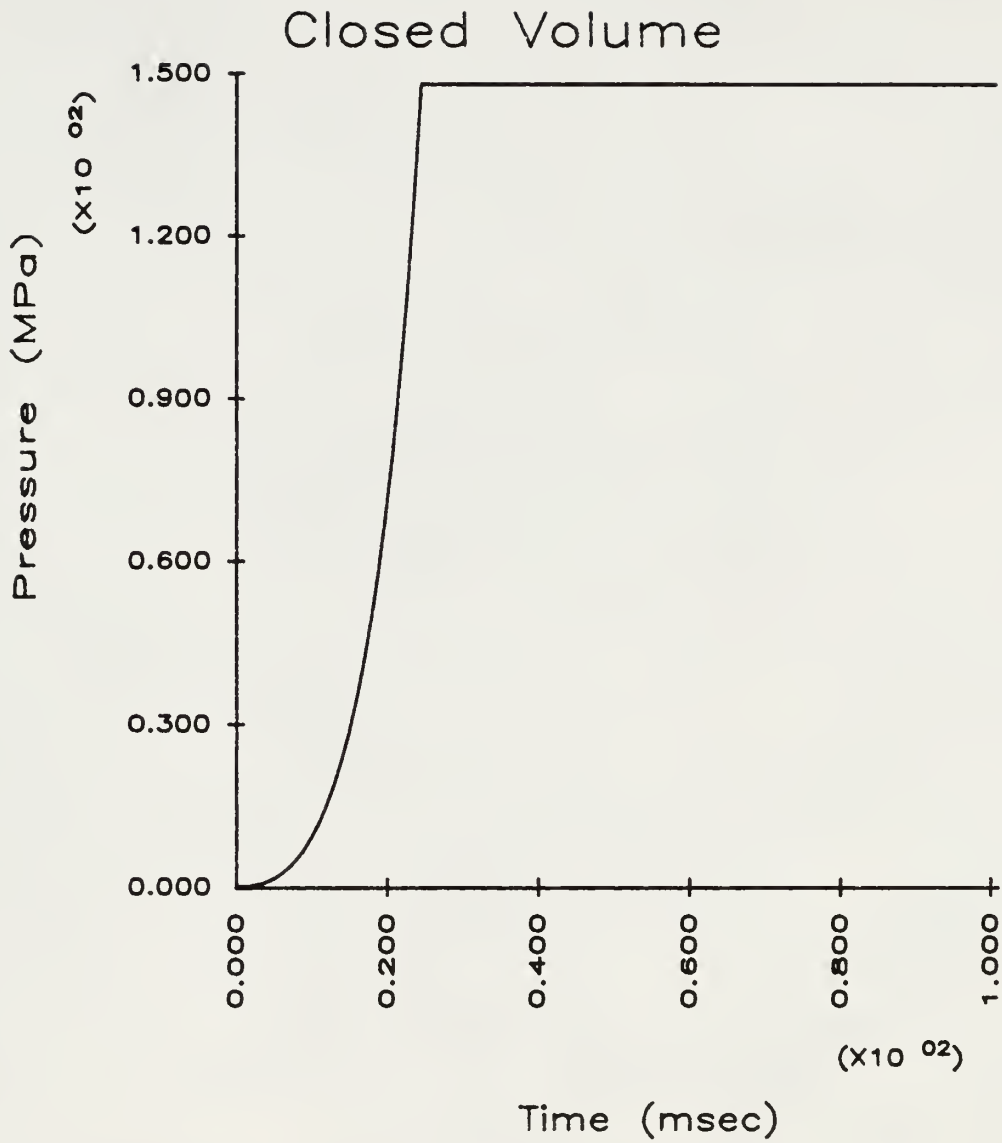


Figure 4.2: Numerical Results of Closed Bomb Test

Propellant	NQ/M
Amount of propellant	10 grams
Web thickness	0.001118*1.15 m
Volume	8.194E-5 m ³
Energy density	1052.5E3 J/Kg
Covolume	0.001085 m ³ /kg
Burn rate constant	4.0653E-7 m/sec/Pa
Burn rate exponent	0.6495
Solid density	1665 kg/m ³
Pack density	750 kg/m ³

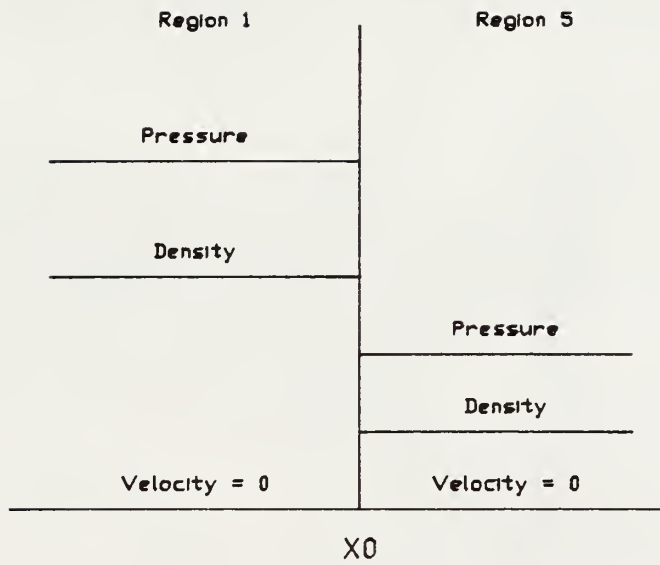
Table 4.1: Burn model verification parameters

subjected to the extreme pressure and temperature conditions found behind a shock wave (John, 1984). This is accomplished by separating a high pressure gas from a low pressure gas using a diaphragm. Typical pressure, density, and velocity profiles shortly after rupture of the diaphragm are shown in Figure 4.3 (Sod, 1978). When the diaphragm is ruptured, a discontinuity in gas properties exists, which is characteristic of a normal shock. This normal shock then moves into the low pressure side, with a series of expansion waves propagating into the high pressure gas. Points x_1 and x_2 represent the location of the head and tail of the expansion, or rarefaction, wave moving to the left. The point x_3 is where the contact discontinuity occurs. The pressure and velocity are continuous across the contact surface. However, the density and temperature are not continuous across a contact surface. Point x_4 is the location of the shock wave moving to the right. Across the shock, all of the quantities (ρ, T, P, U) will be discontinuous.

In this test of the model, the following conditions were used:

$$\begin{array}{lll} \rho_1 = 1.0 & P_1 = 1.0 & u_1 = 0.0 \\ \rho_5 = 0.125 & P_5 = 0.1 & u_5 = 0.0 \end{array}$$

The ratio of specific heats was 1.4 and $\Delta x = .002$ meters. The analytic solution of the hyperbolic system of conservation laws (Riemann problem) was found using a Brent iteration scheme (see Halter, 1985). Figures 4.4, 4.5, and 4.6 compare the pressure, density, and velocity distributions obtained using the Lax and Brent methods.



Shock Tube $t = 0$

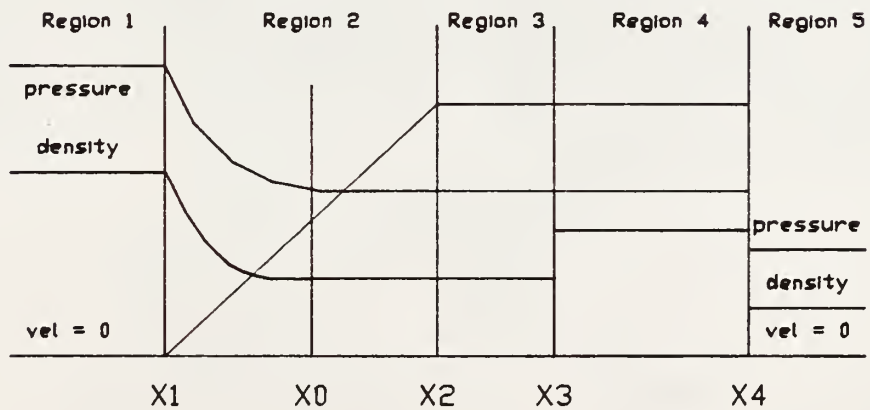


Figure 4.3: Shock Tube $t > 0$ (After Sod, 1978)

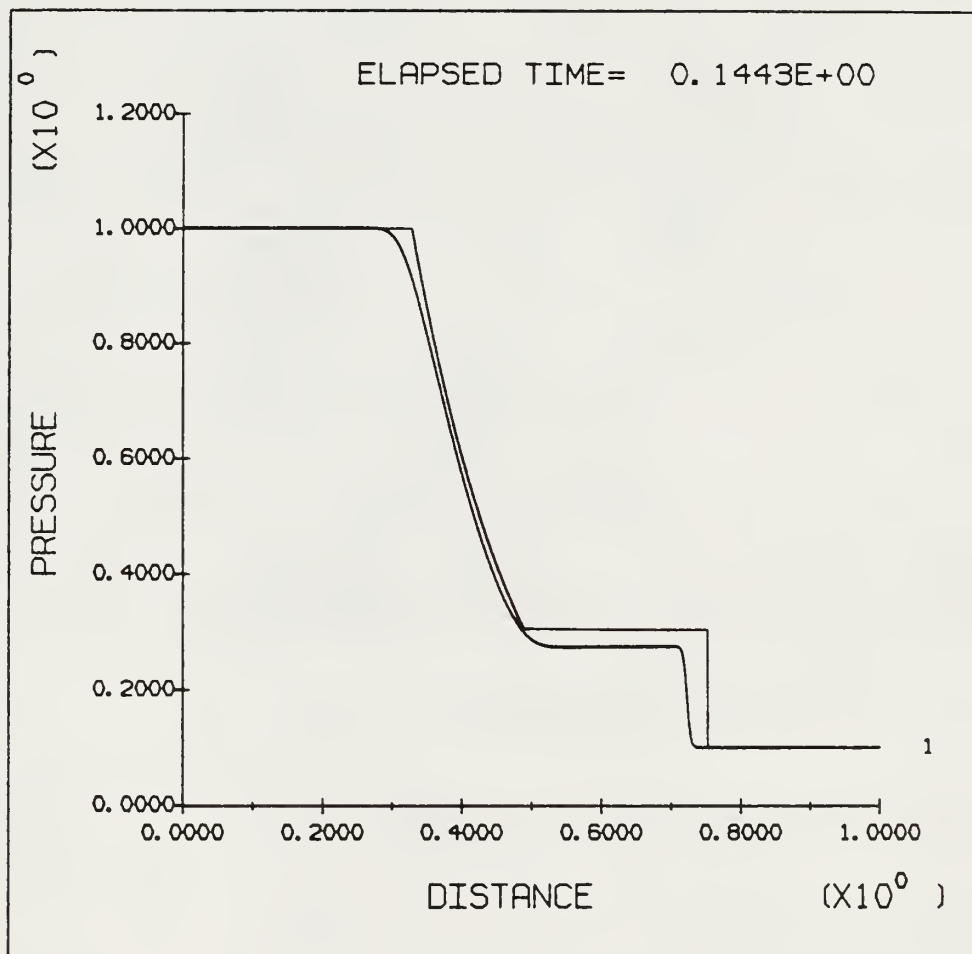


Figure 4.4: Pressure profile of Riemann problem using Lax method

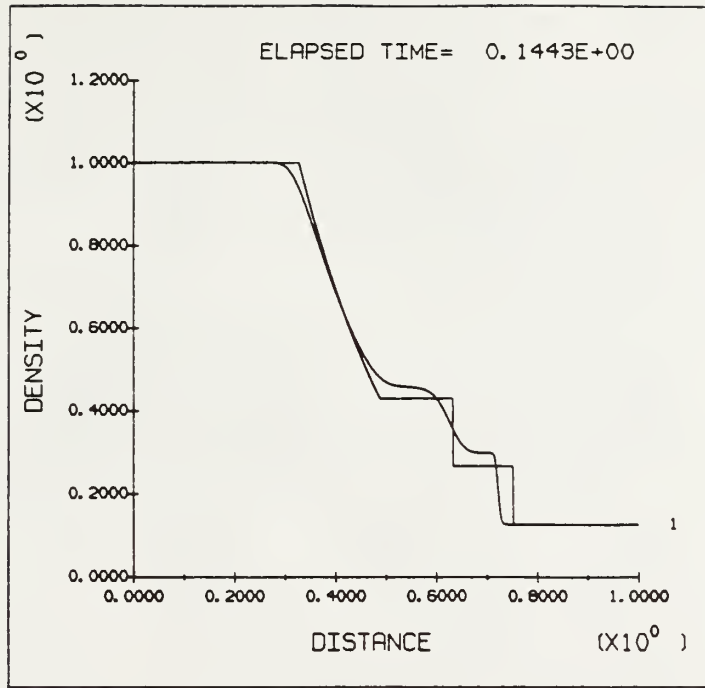


Figure 4.5: Density profile of Riemann problem using Lax method

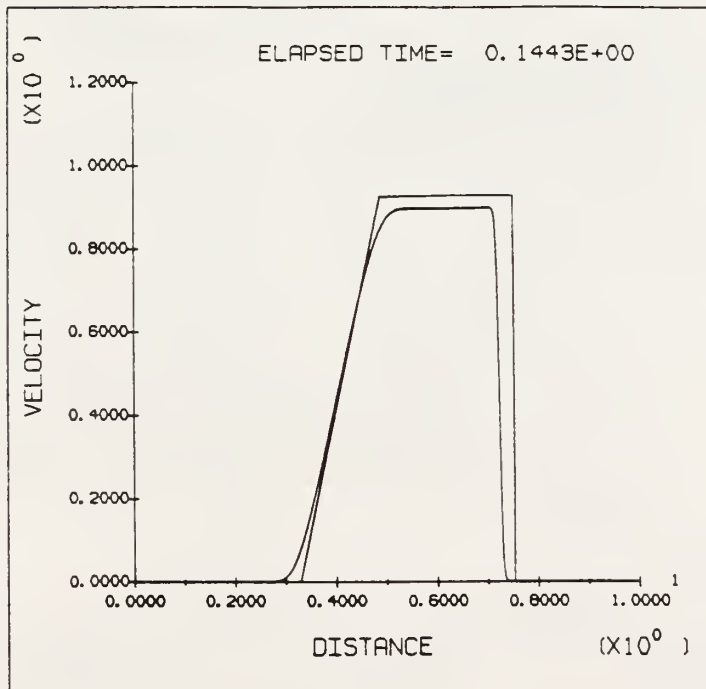


Figure 4.6: Velocity profile of Riemann problem using Lax method

There is relatively close agreement across the rarefaction. However, the corners at the endpoints of the rarefaction are rounded. There is not as close agreement at the contact surface and shock. The reader should keep in mind that the purpose of this model is to predict gas flow under conditions that are definitely not isentropic. Isentropic conditions are assumed for shock tubes. Because of this, the inability of the Lax method to accurately predict sharp discontinuities should not effect the results greatly.

4.3 Simplified Crack Problem

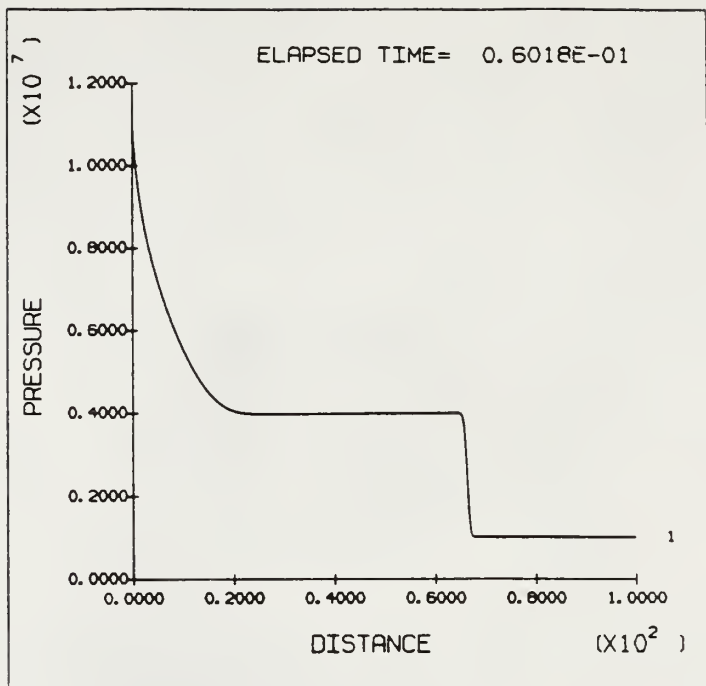
Although this section does not describe a verification problem, it does give some insight into the effects of some of the variables involved. The results to be presented, in addition to others, were used to debug the coding, and also to begin to understand gas flow in a crack before large problems were attempted. Different ideas could be tried and tested with these problems using minutes of computer time. Typical large problems ran in excess of 15 CPU hours on a H800 Harris mini-computer.

A 100 meter crack with uniform cross-sectional area was used. The borehole temperature and initial crack temperature was initially 1000 K. The initial borehole pressure was 40MPa and the initial crack pressure was 1 MPa. The cases considered are displayed in Table 4.2. The variables f , v , and q represent friction, seepage, and heat transfer.

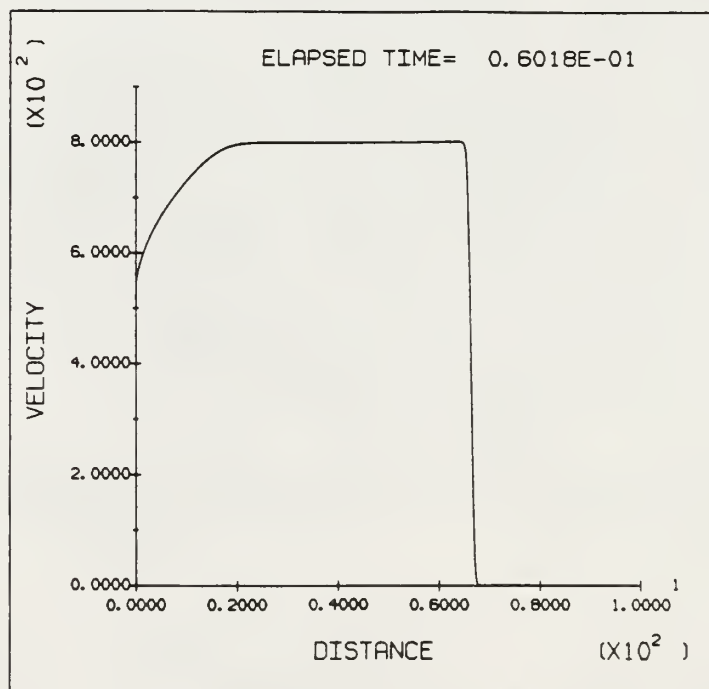
The purpose of Cases 1 & 2 was to determine the effect of the time step reduction factor and damping. Figures 4.7 and 4.8 show the pressure and velocity results for Cases 1 & 2. The flow in the crack

<u>Case</u>	Initial		time	damping	Δx	<u>losses</u>
	Borehole	Crack				
	Pressure	Pressure	step			
	(MPa)	(MPa)	<u>reduction</u>	<u>factor</u>	(m)	
1	40E6	1E6	1	0.99	0.205	none
2	40E6	1E6	0.9	0.8	1.01	none
3	40E6	1E6	0.9	0.8	1.01	f,v,q

Table 4.2: Verification Problems

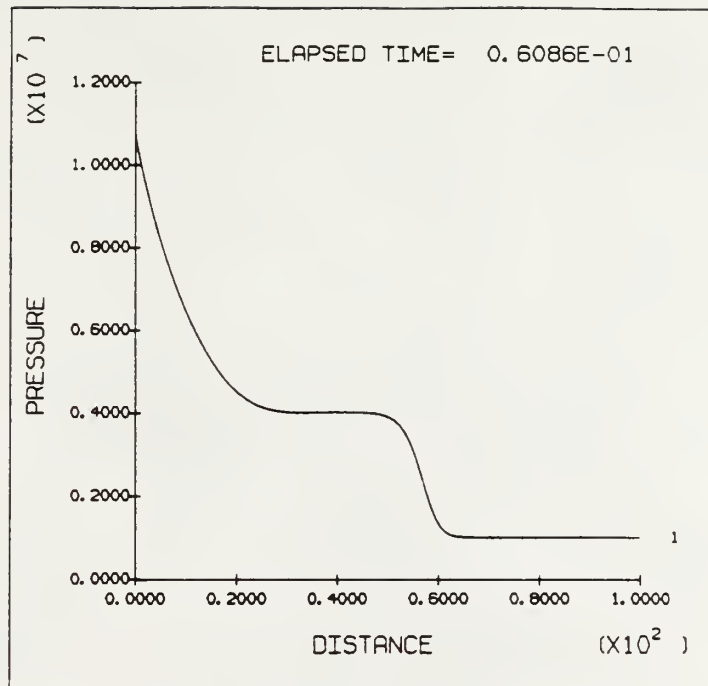


a. Pressure

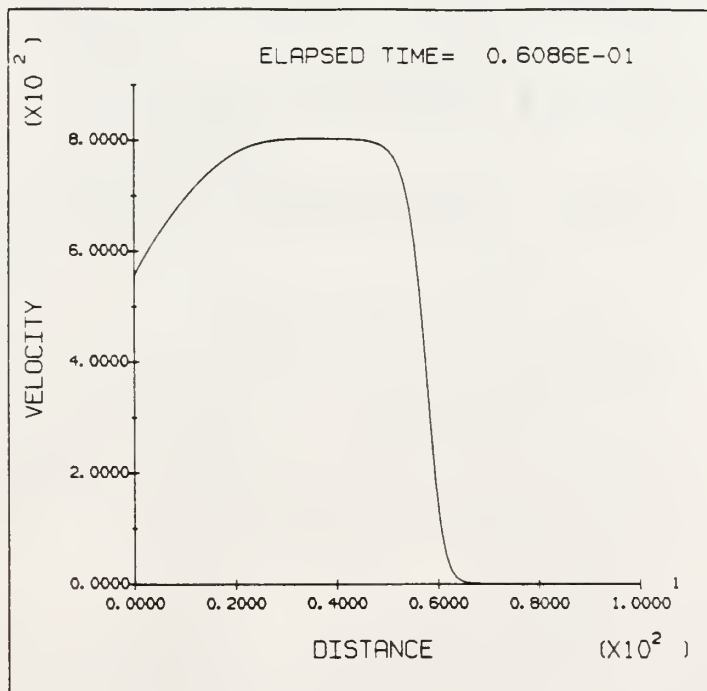


b. Velocity

Figure 4.7: Profiles for Verification Case 1



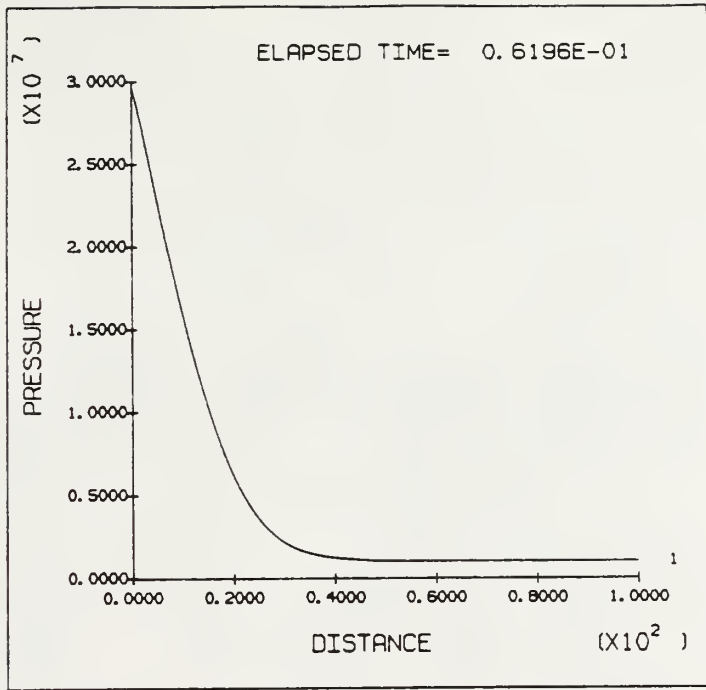
a. Pressure



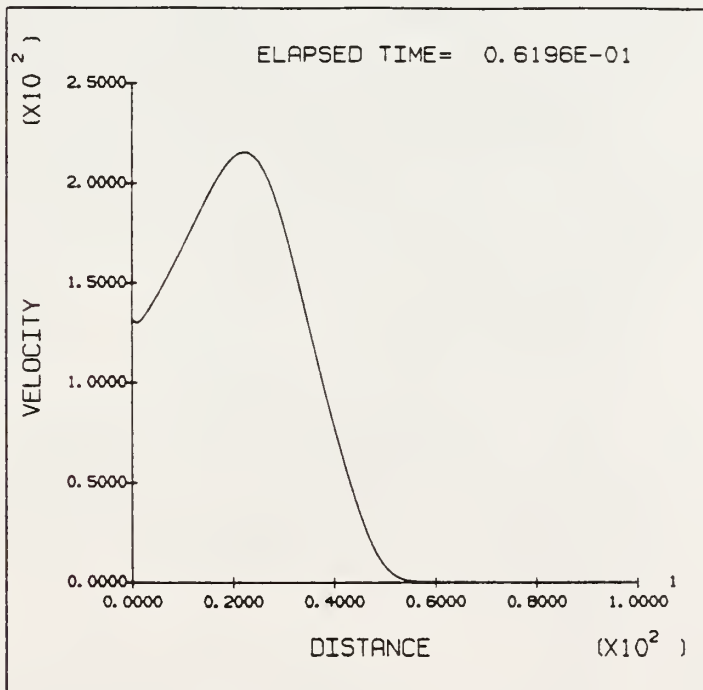
b. Velocity

Figure 4.8: Profiles for Verification Case 2

is supersonic, and the rarefaction wave is moving into the crack mouth. This causes the reduction from the borehole pressure at the crack entrance. Although the shock wave isn't as distinct in Case 2, the effect of the pressure wave is still present. Figure 4.9 shows the pressure and velocity profiles for Case 3. The velocity remains subsonic and the pressure decreases rapidly from the crack mouth. The smoothing of the shock wave with the introduction of friction, heat transfer, and seepage is typical of what is expected when propagating a crack.



a. Pressure



b. Velocity

Figure 4.9: Profiles for Verification Case 3

CHAPTER 5

APPLICATIONS

In this chapter we address the question of possible fracture length for realistic burn conditions. To do this, we use a quarter model of a borehole with symmetry conditions imposed. Therefore, the model represents a borehole with four radial cracks. Several different borehole pressures and loading rates, using either a burn model for a propellant or specified pressure time histories, are used.

The model geometry, shown in Figure 5.1, was used in Cases 3 & 4. This geometry was used to minimize the required computer run time after it was realized long fractures were not going to be seen. The other problems used a square geometry that extended 70 meters. The material properties for sandstone are shown in Table 5.1. The rock and gas values needed by the gas model are shown in Table 5.2. No dynamic critical stress intensity data is known for sandstone, so the estimated dynamic curve was based on the static value. The curve used is shown in Figure 5.2.

A borehole diameter of 0.2 meters was assumed with an initial 0.146 meter fracture extending at 45 degrees to the X and Y axis. Since symmetry was present in these cases, this actually represents four fractures in a radial pattern. The outer boundary was at least 35 meters from the borehole in all cases to prevent interference from a reflected stress wave.

To set up the problem, the initial in-situ stresses were first applied uniformly to the mesh. For all cases, the in-situ stresses

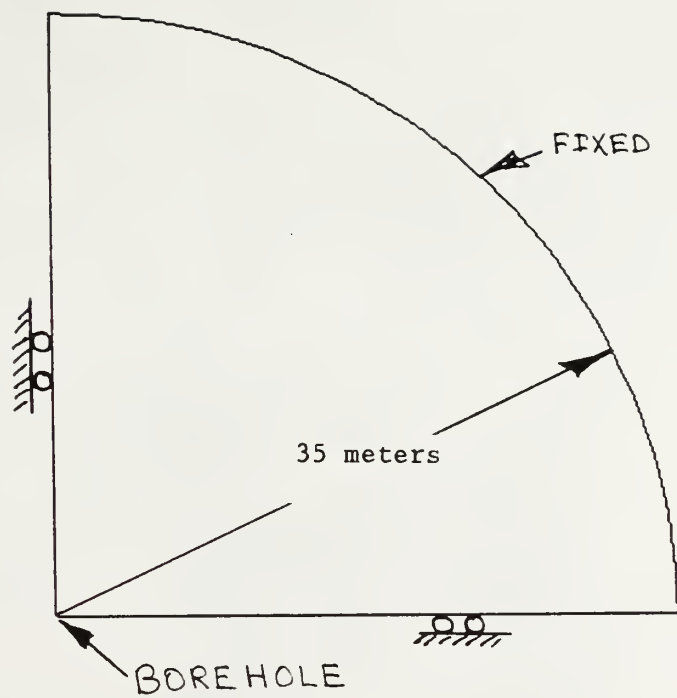


Figure 5.1: Model Geometry

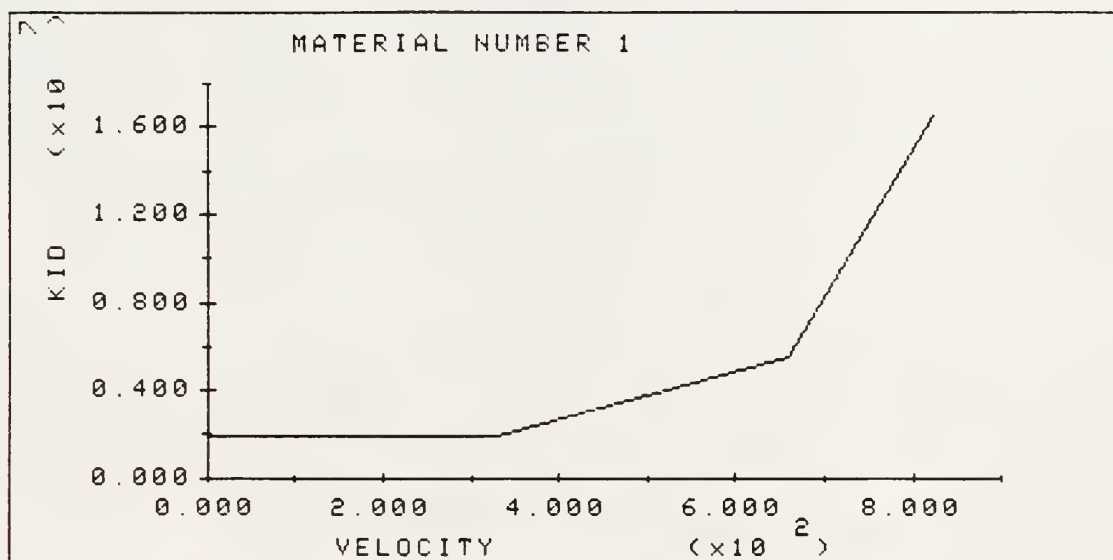


Figure 5.2: Assumed Dynamic Stress Intensity for Sandstone

$$E = 24.82E9 \text{ Pa}$$

$$\nu = 0.22$$

$$\rho = 2600 \text{ Kg/m}^3$$

$$KIc = 1.978E6 \text{ Pa}\sqrt{\text{m}}$$

$$c_1 = 3048 \text{ m/sec}$$

$$c_2 = 1806 \text{ m/sec}$$

$$c_R = 1651 \text{ m/sec}$$

Table 5.1: Material properties for sandstone

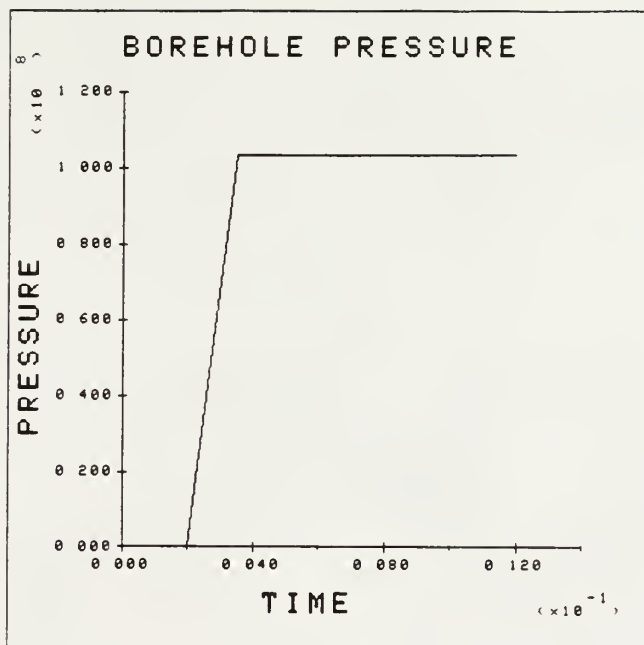
Initial crack pressure	100 KPa
Initial crack temperature	300 deg K
Specific heat ratio	1.4
Ideal gas constant	296.8 J/Kg/K
Borehole volume(qtr symmetry)	0.007854 m ³
Charge volume(qtr symmetry)	0.0019635 m ³
Solid density	1650 J/Kg
Pack density	700 J/kg
Form coefficient	0.62
Burn rate coefficient	$0.53968\text{E-}7 \text{ m sec}^{-1}\text{Pa}^{-.8}$
Burn rate exponent	0.8
Covolume	0.001 m ³ /Kg
Web thickness	0.000762 m
Propellant energy density	1038.7E3 J/Kg
Surface roughness	5-20 μm
Permeability	0.1E-14 m ²
Porosity	0.02
Far field pressure	100 KPa
Far field temperature	300 deg K
Conductivity	2 J/m/K/sec
Thermal diffusivity	0.4E-5 m ² /sec

Table 5.2: Parameters used in gas model

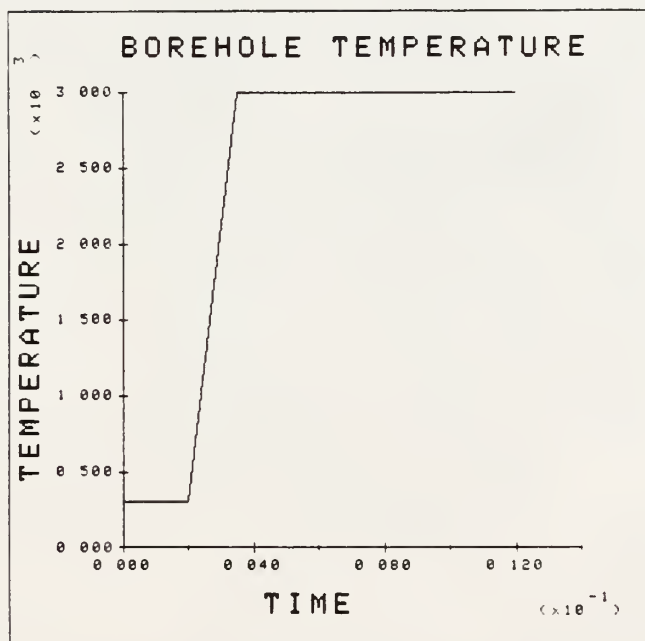
were $\sigma_x = \sigma_y = -17.23\text{MPa}$. No overburden stress was assumed. A short test using $\sigma_z = -6.89\text{MPa}$ found that there was a 10-14% difference in crack length and K_I when σ_z was ignored. Before beginning the dynamic analysis, static equilibrium was achieved by introducing a small amount of damping and allowing the problem to run until there was negligible change in node displacement. This allows the stresses around the borehole to come to equilibrium before proceeding with the pressure loading. For the cases presented here, equilibrium occurred at $t = 0.002$ sec. The reader should keep this in mind when evaluating time plots since the actual dynamic problem starts at 2 msec.

5.1 Case 1 - Specified Borehole Pressure With No Losses In The Fracture

Case 1 will be used as the reference case with which other results will be compared. Although a no-loss case is not realistic, it does give the easiest case for comparison. The borehole pressure was ramped to 103.4 MPa and the borehole temperature was ramped to 3000 deg. K. These time histories are shown in Figure 5.3. Figure 5.4 shows the displaced mesh results at 12 msec. At this time the crack is about 8.5 meters long and the crack opening displacement at the borehole is approximately 0.01 meters. Plots of crack opening and crack length are shown in Figures 5.5 and 5.6. The crack tip velocity, Figure 5.7, reaches the limiting crack velocity of 0.5 of the Rayleigh wave speed during propagation. This limit is imposed by the numerical solution scheme. In reality, bifurcation would probably occur at this large loading. The significant point is that without



a. Pressure



b. Temperature

Figure 5.3: Borehole Time Histories

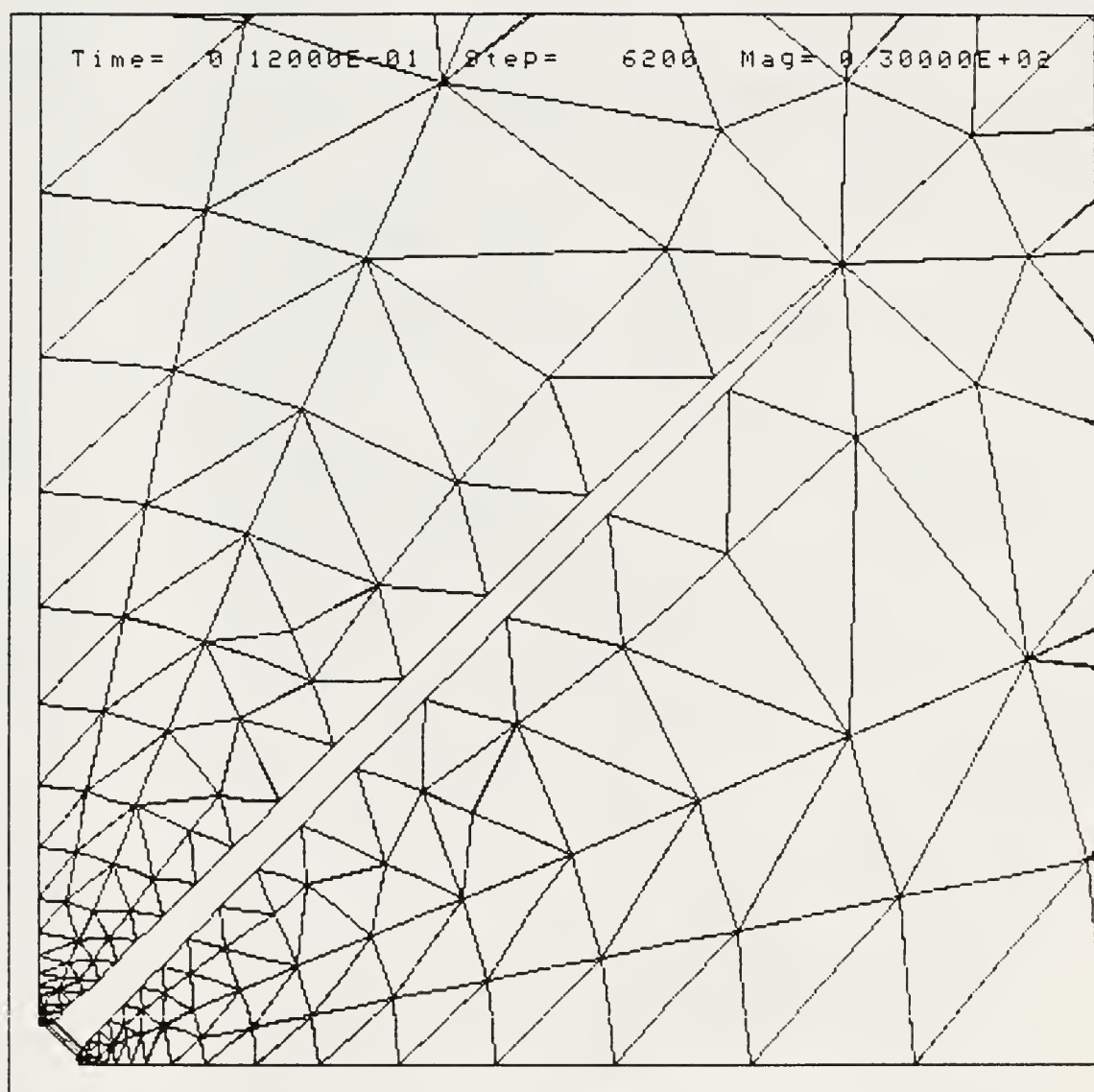


Figure 5.4: Displaced Mesh Results for Case 1 at 12 msec

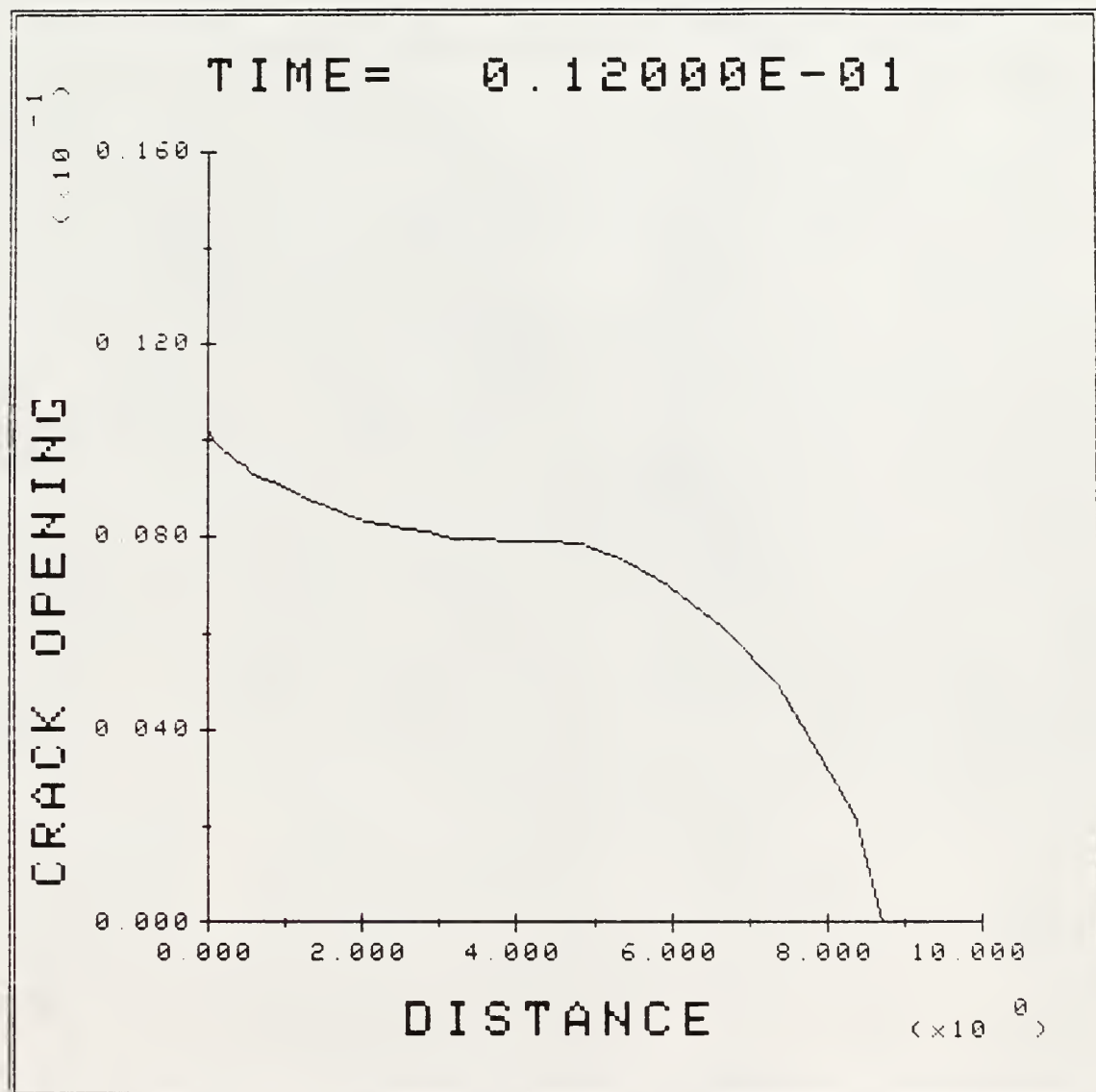


Figure 5.5: Crack Opening Displacement for Case 1 at 12 msec

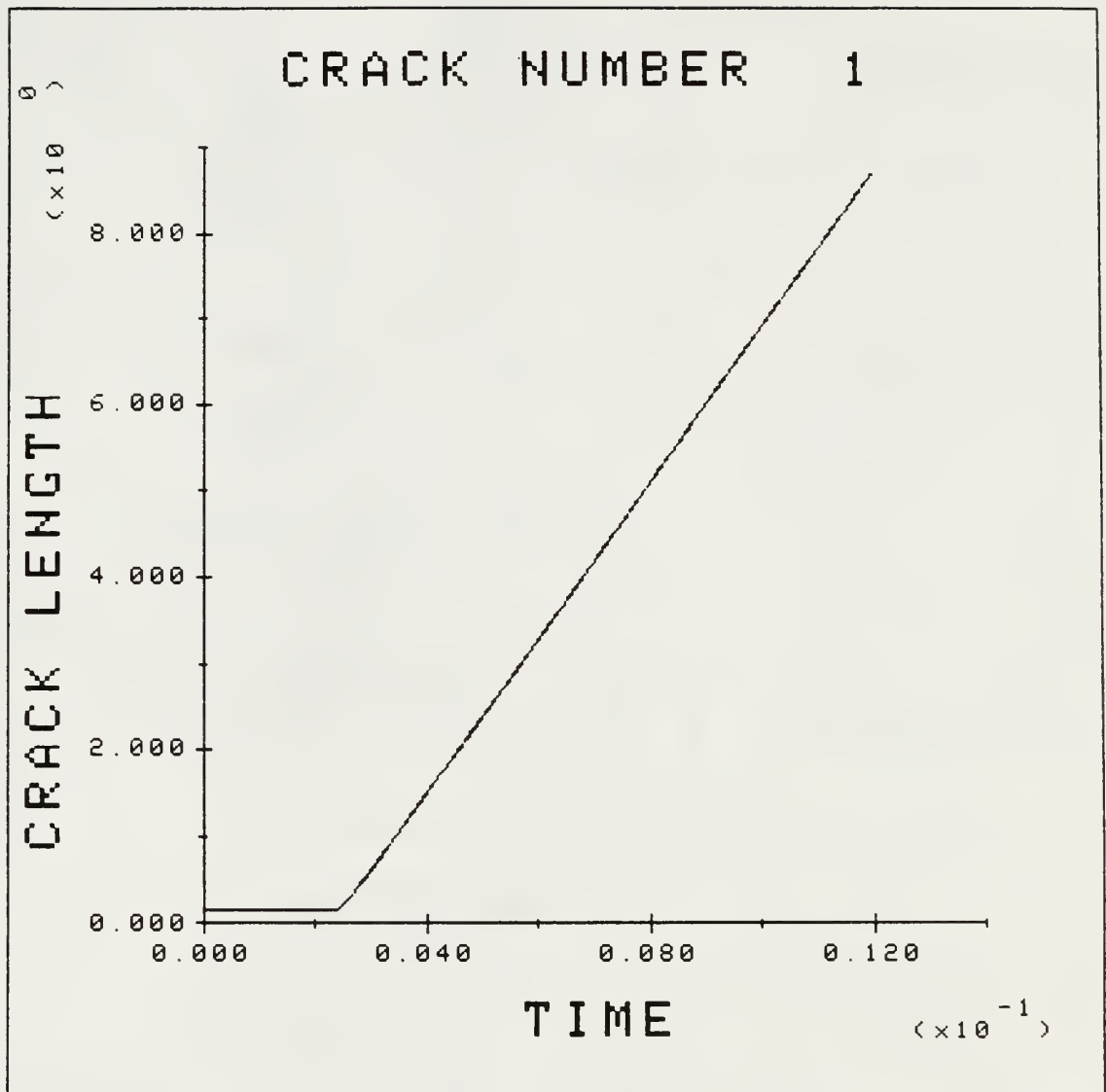


Figure 5.6: Crack Length for Case 1

losses, the limit on crack velocity is due to the rock response. The gas is attempting to over-drive the crack. Plots of K_{ID} and K_{IID} during propagation are shown in Figures 5.8 and 5.9. Comparing the crack tip velocity to the gas velocity shown in Figure 5.10, it can be seen that the pressure wave has reached the crack tip and is partially reflected. This will result in the large K_{ID} and the fact that the crack is driven hard enough to probably bifurcate. Temperature, pressure, density, and mach number plots are shown in Figures 5.11 through 5.14. Note that the gas flow is supersonic for a significant portion of the crack length. Since the pressure wave has reached the crack tip, all the property values are relatively constant along the crack face. It will be seen that when losses are introduced, there are large variations between property values at the crack mouth and crack tip.

To illustrate that the gas pressure is being correctly applied to the crack face, Figure 5.15 shows the normal stress along a line parallel to the crack. The normal stress distribution is similar to the gas pressure in the fracture.

An interesting result of this analysis is shown in Figure 5.16. From this plot, the net energy that has left the borehole up to a given time can be found. In future reference, this plot will be called the crack entrance energy plot. At 6 msec, about 0.96×10^6 J entered the crack and has driven the fracture about 3.0 meters. It should be kept in mind that some of this energy has not been used to drive the crack, but has instead been used to increase the kinetic and internal energy of the gas in the fracture. This stored energy will

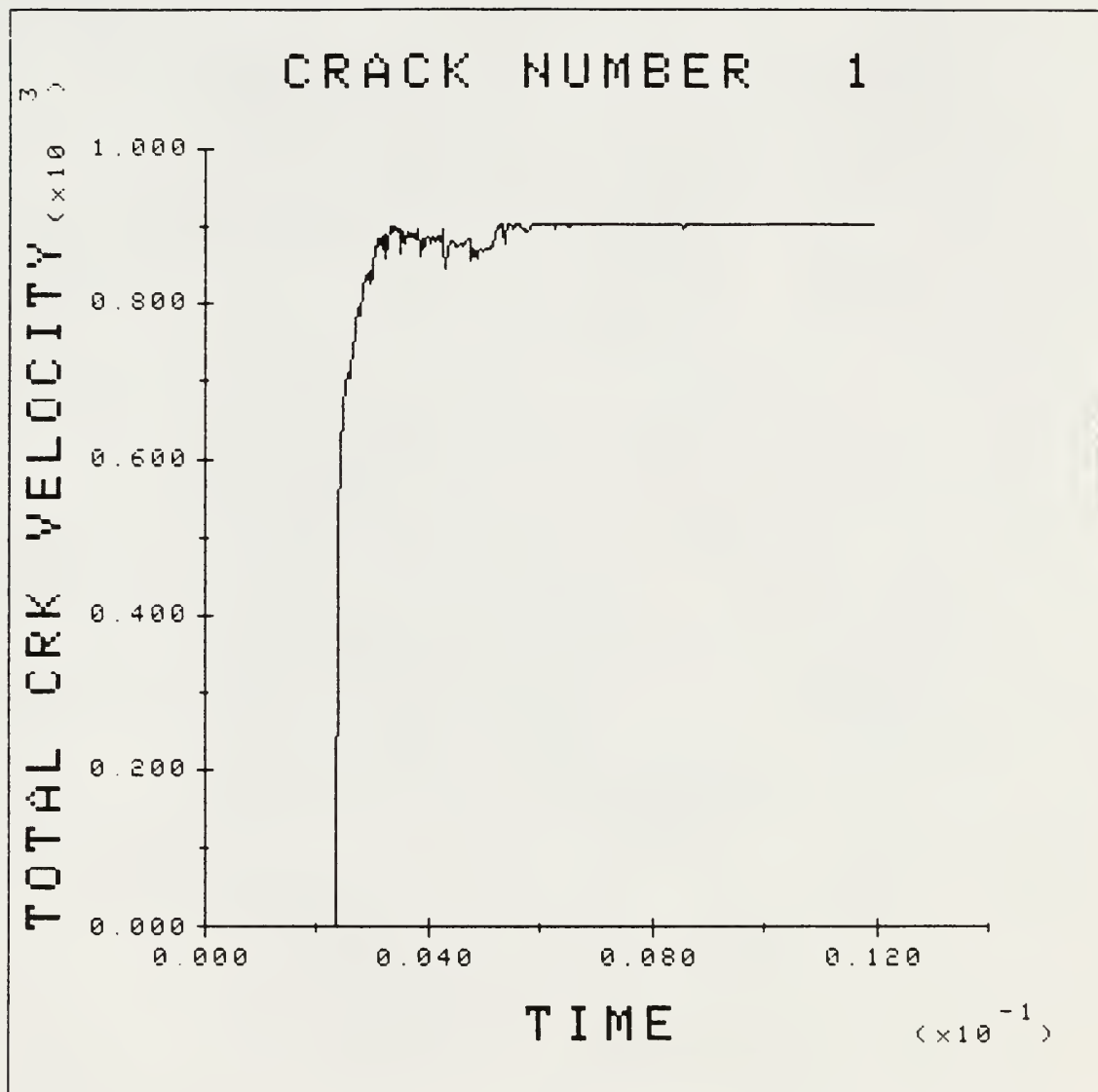


Figure 5.7: Crack Velocity for Case 1

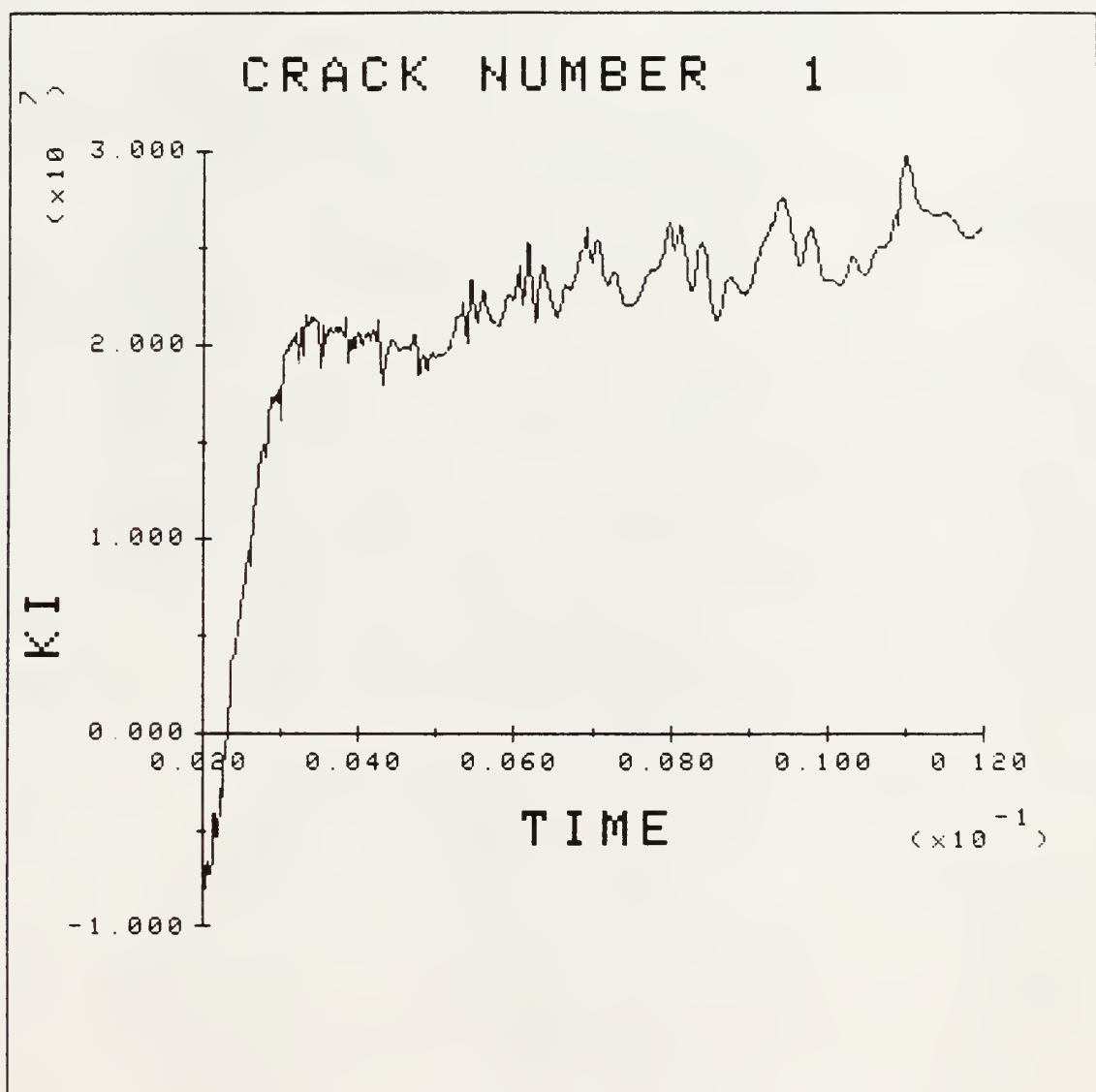


Figure 5.8: KID During Propagation for Case 1

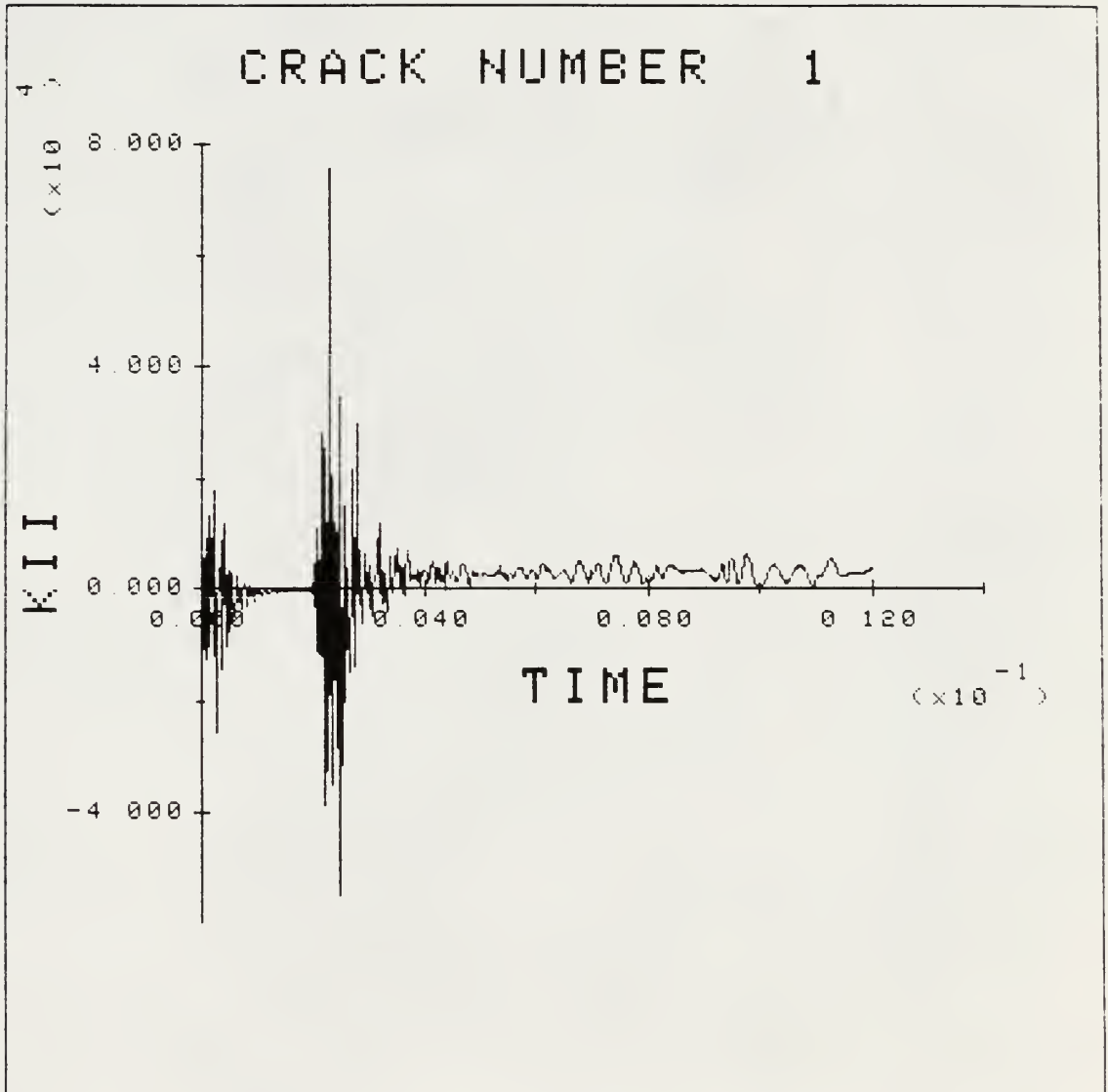


Figure 5.9: KIID During Propagation for Case 2

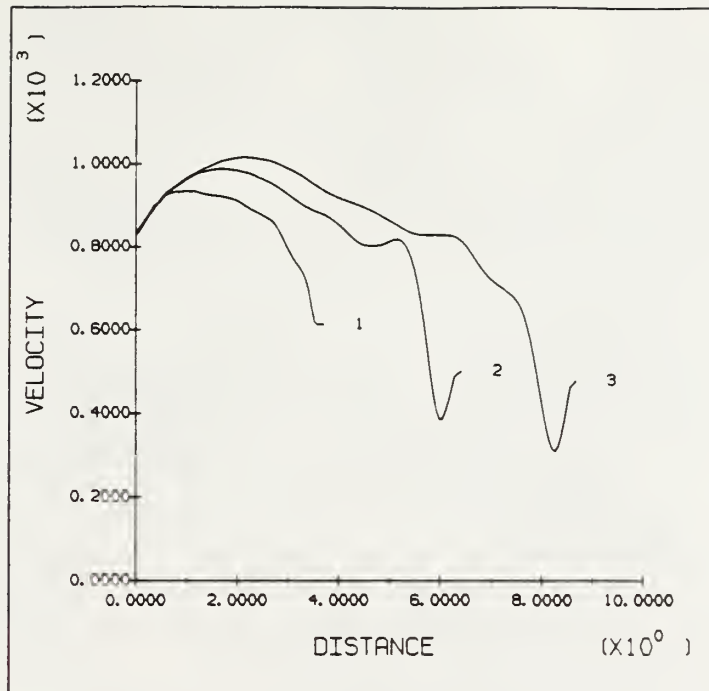


Figure 5.10: Gas Velocity for Case 1 at 6.5, 9.5, and 12 msec

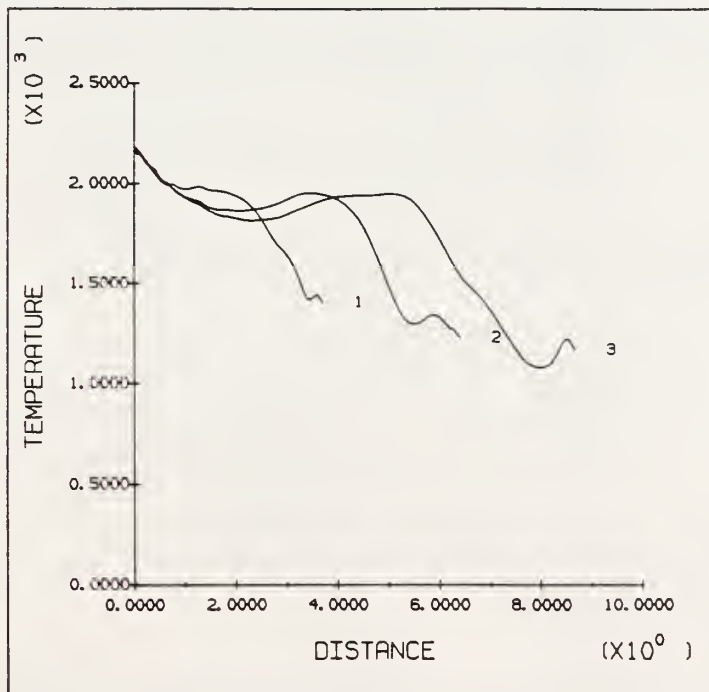


Figure 5.11: Gas Temperature for Case 1 at 6.5, 9.5, and 12 msec

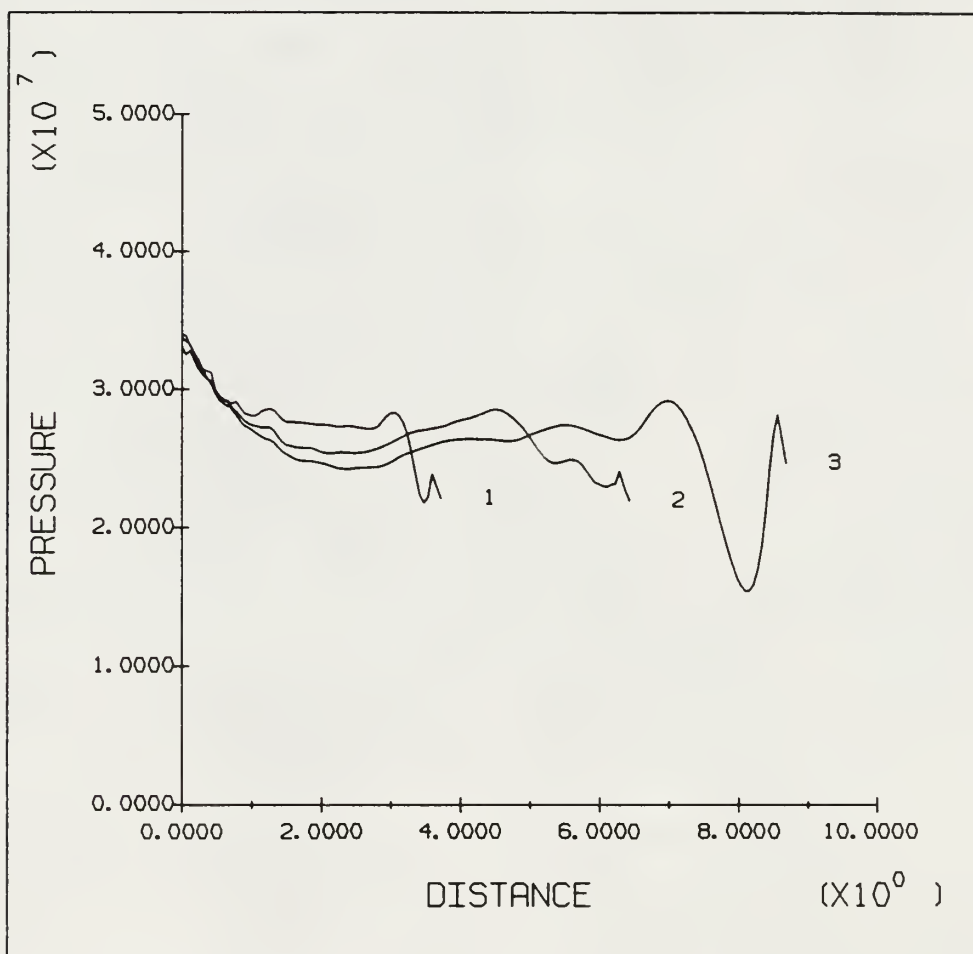


Figure 5.12: Gas Pressure for Case 1 at 6.5, 9.5, and 12 msec

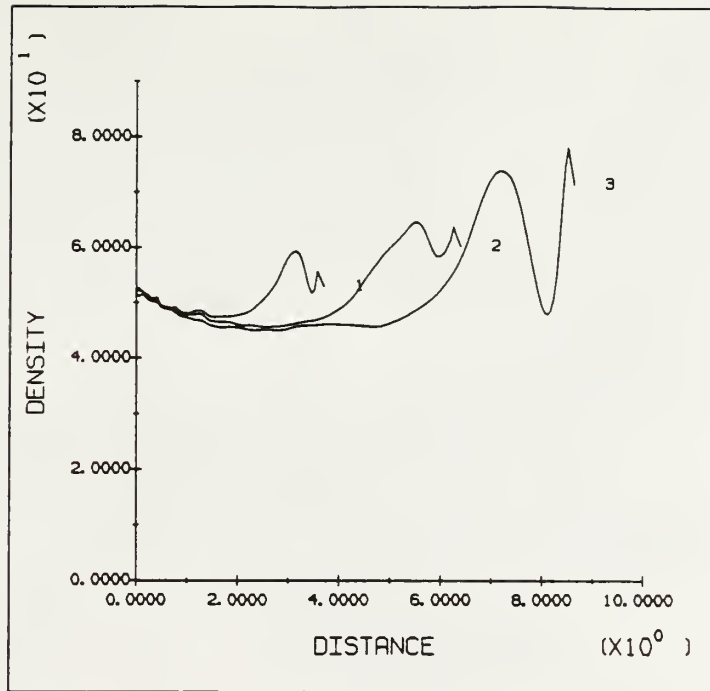


Figure 5.13: Gas Density for Case 1 at 6.5, 9.5, and 12 msec

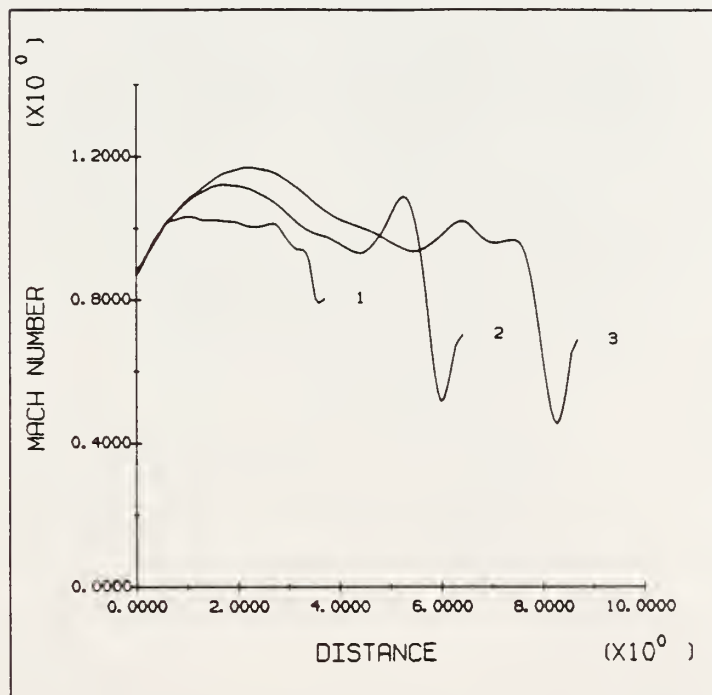


Figure 5.14: Mach Number for Case 1 at 6.5, 9.5, and 12 msec

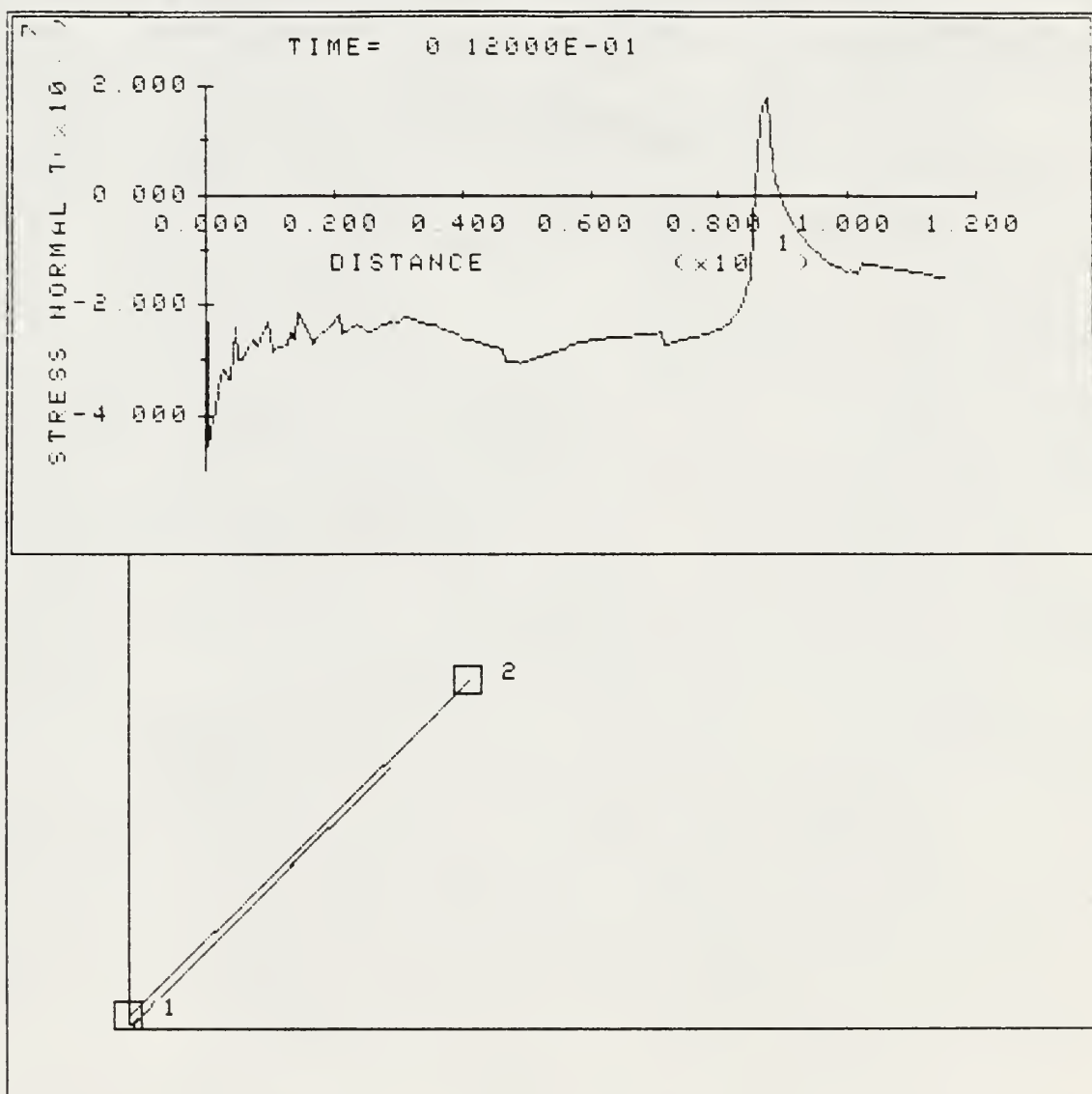


Figure 5.15: Normal Stress along Crack Face at 12 msec

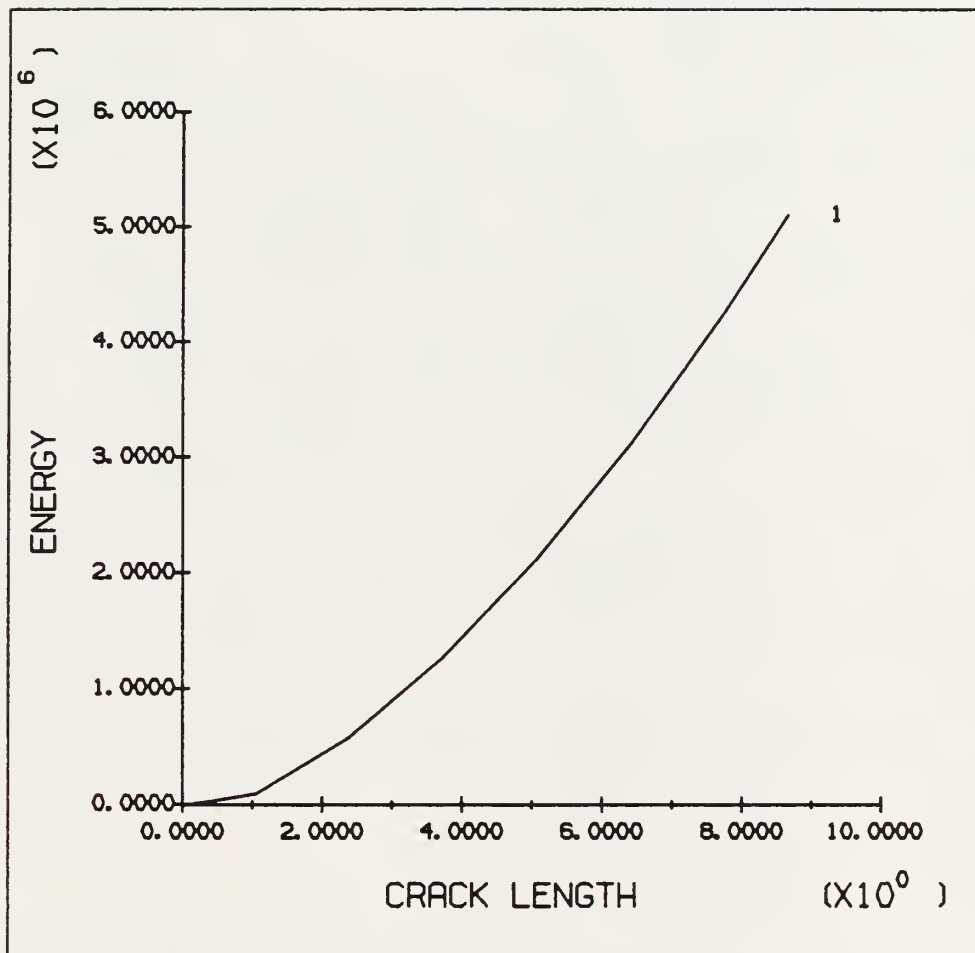


Figure 5.16: Crack Entrance Energy for Case 1

later become available to further drive the crack. Figure 5.17 shows the work done to move the boundaries of the problem. Although the work done to expand the borehole is included, its contribution should be minimal. At $t=0$, this value is initialized by using the combined initial values of strain and kinetic energy ($E_{t=0} = 45.7 \times 10^6 \text{ J}$). Subtracting this initial value from the value shown in Figure 5.17 at 6 msec will give us the boundary work done of $0.3 \times 10^6 \text{ J}$. If we subtract the energy doing boundary work from the supplied energy, an approximation of the energy present in the gas of $0.93 \times 10^6 \text{ J}$ can be found. Comparing this value to the calculated value of gas energy at 6 msec, shown in Figure 5.18, we can find there is a 3 per cent difference. The majority of this error is caused by the inclusion of the borehole expansion work. Even with this error, the conservation of energy is confirmed to hold true in this analysis.

5.2 Case 2 - Specified Borehole Pressure With Friction, Heat Transfer, And Seepage Included

For case 2, the borehole pressure and temperature were again ramped to the maximum values, as in case 1. At 12 msec, the crack mouth opening and crack length are about 0.85 cm and 4 meters, respectively. Plots of crack opening and crack length are shown in Figures 5.19 and 5.20. In contrast to case 1, the crack speed is controlled by the gas flow into the crack. The crack is not being overdriven. The displaced mesh is shown in Figure 5.21. From the crack entrance energy plot shown in Figure 5.22, we can see that about 67% of the energy required in Case 1 is used to run a crack that is

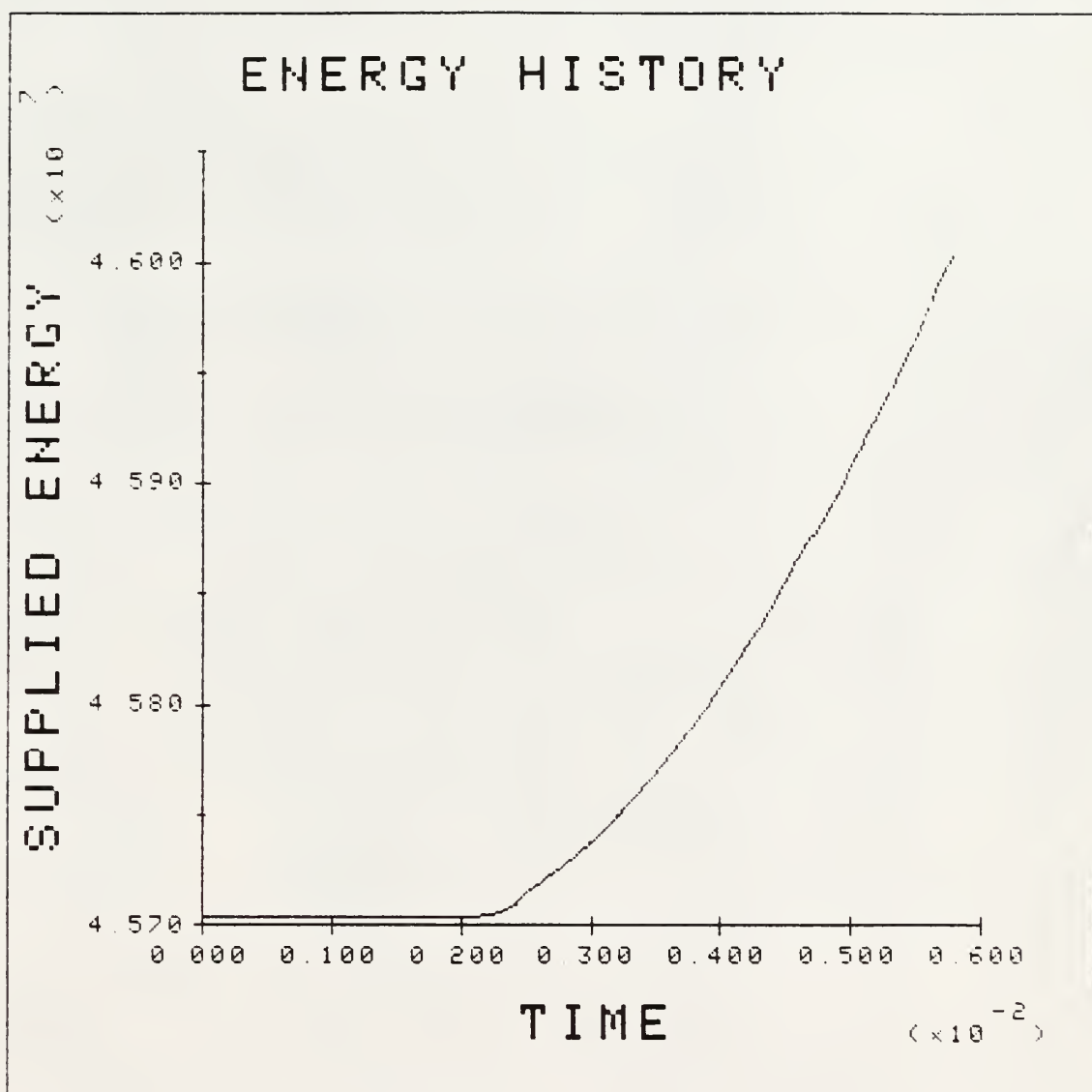


Figure 5.17: Energy Required to Perform Boundary Work for Case 1
(Initialized at 45.7E7 J)

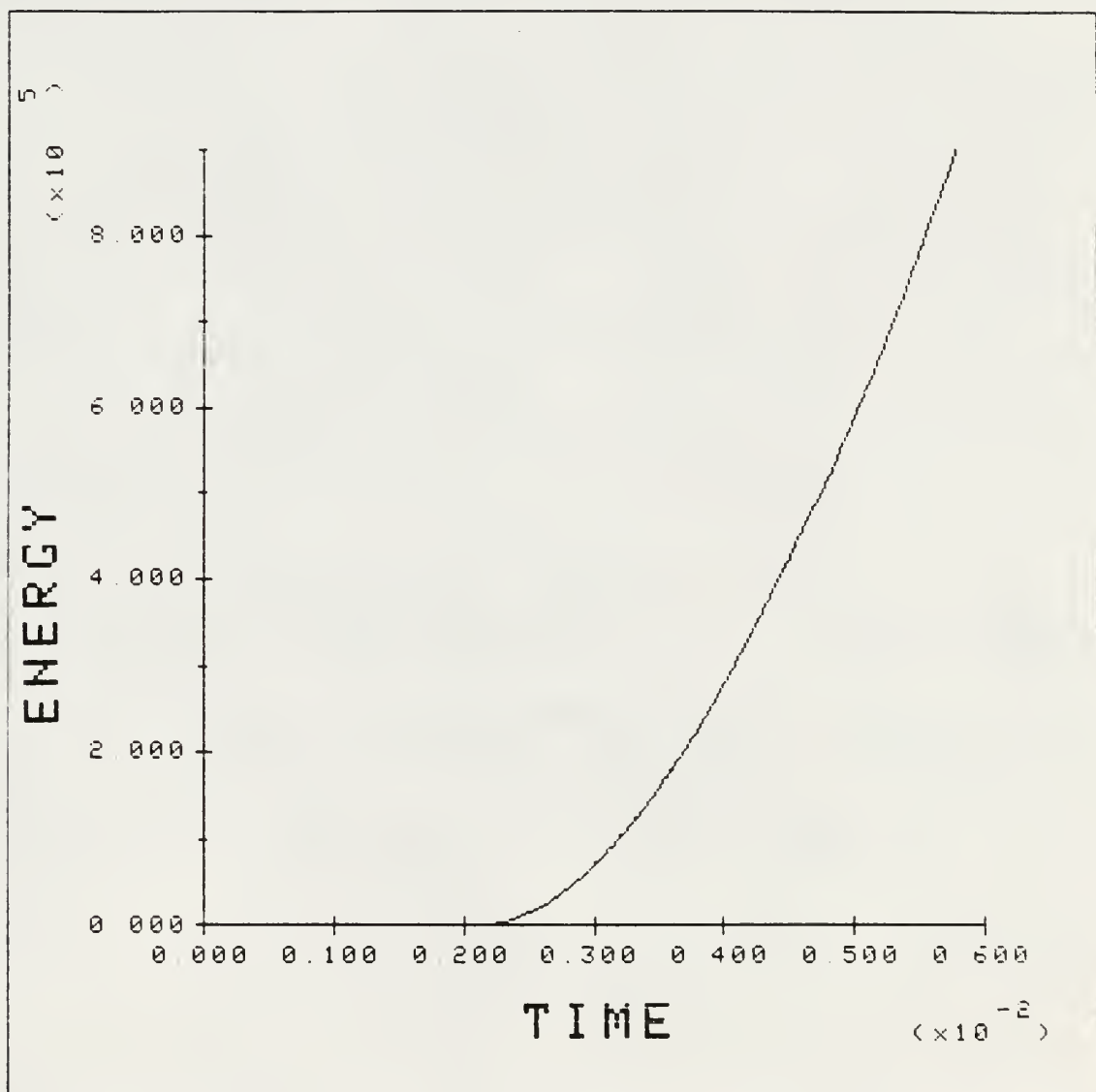


Figure 5.18: Energy Present in Gas for Case 1

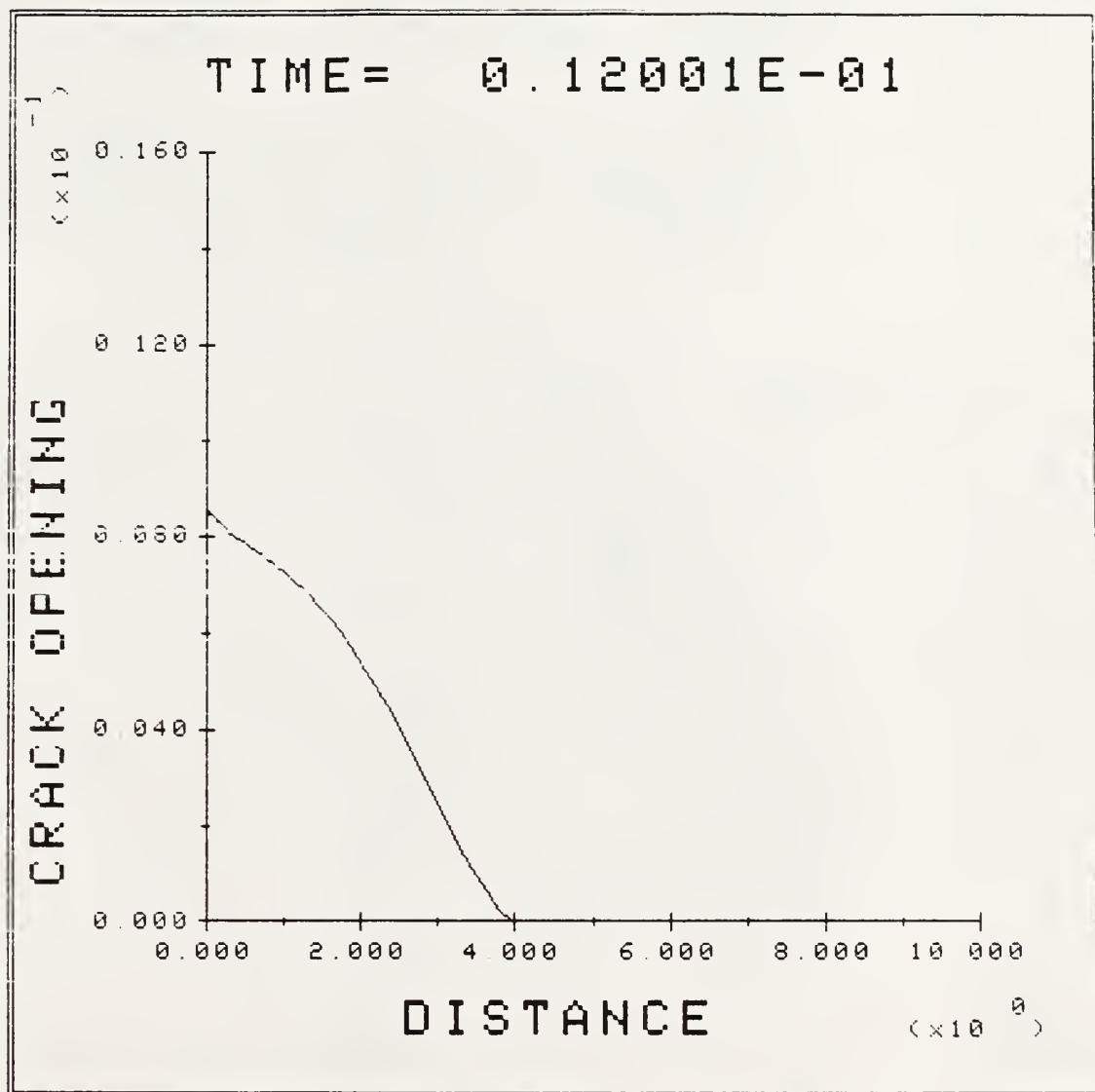


Figure 5.19: Crack Opening Displacement for Case 2 at 12 msec

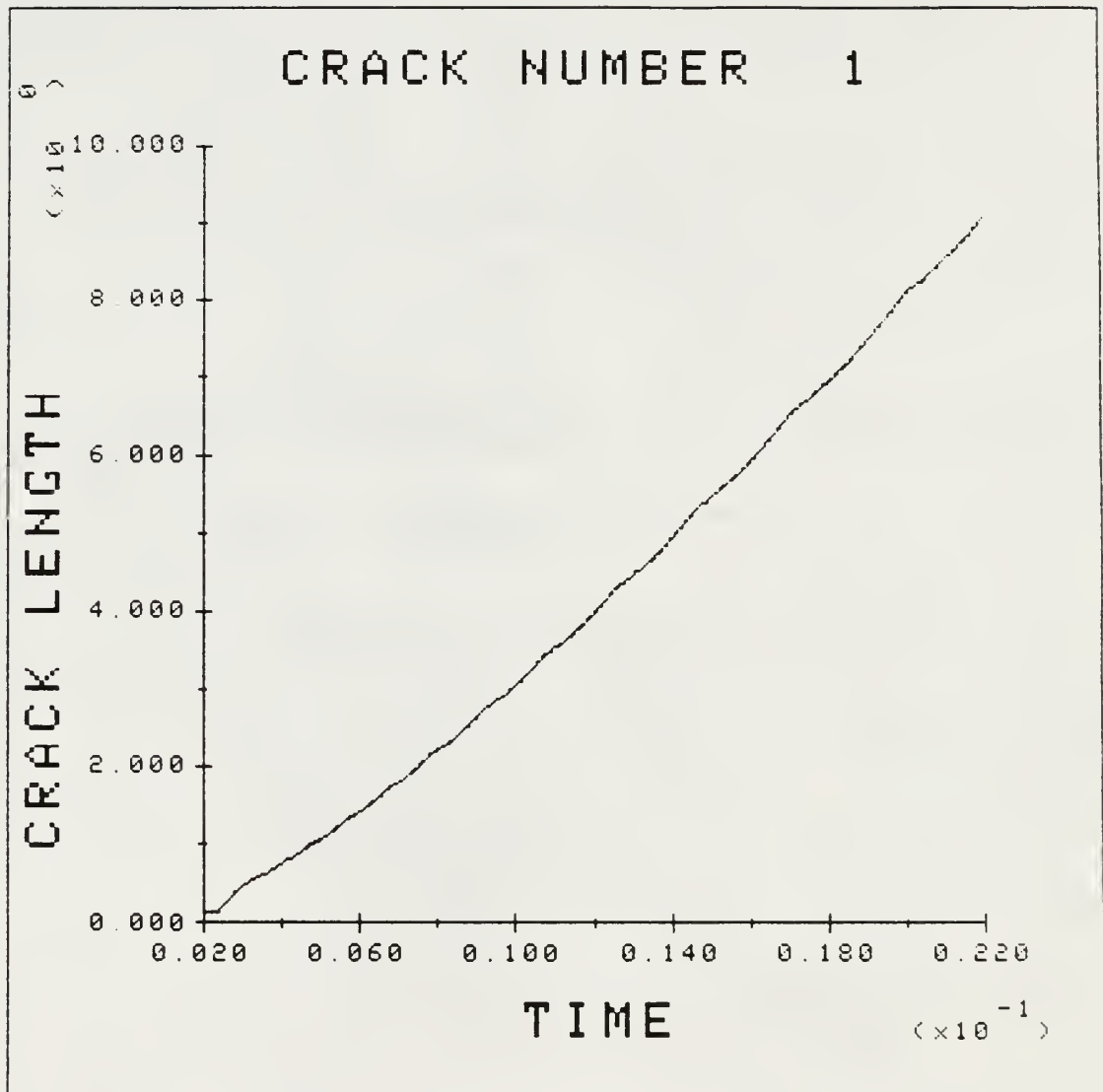


Figure 5.20: Crack Length for Case 2

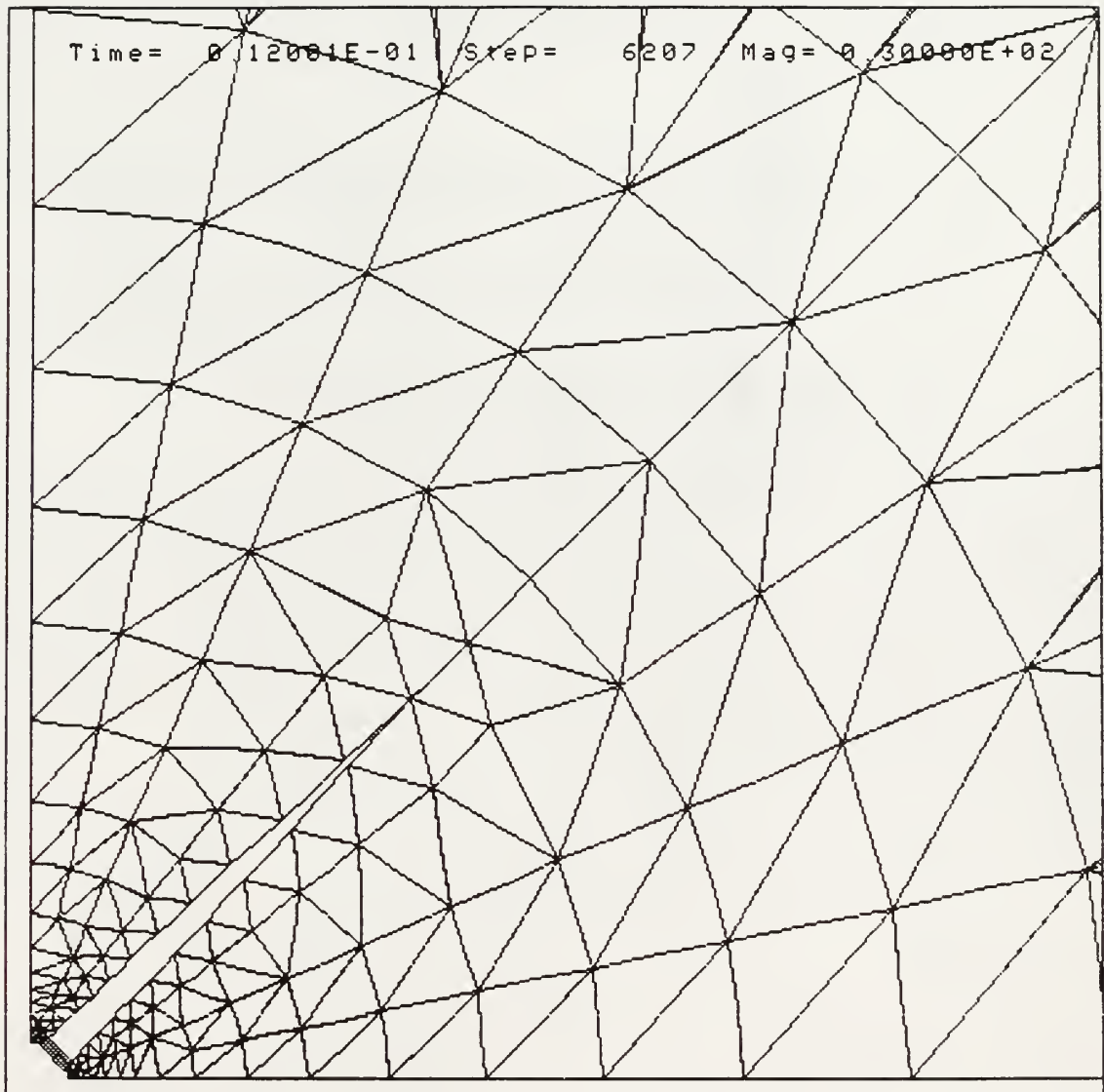


Figure 5.21: Displaced Mesh Results for Case 2 at 12 msec

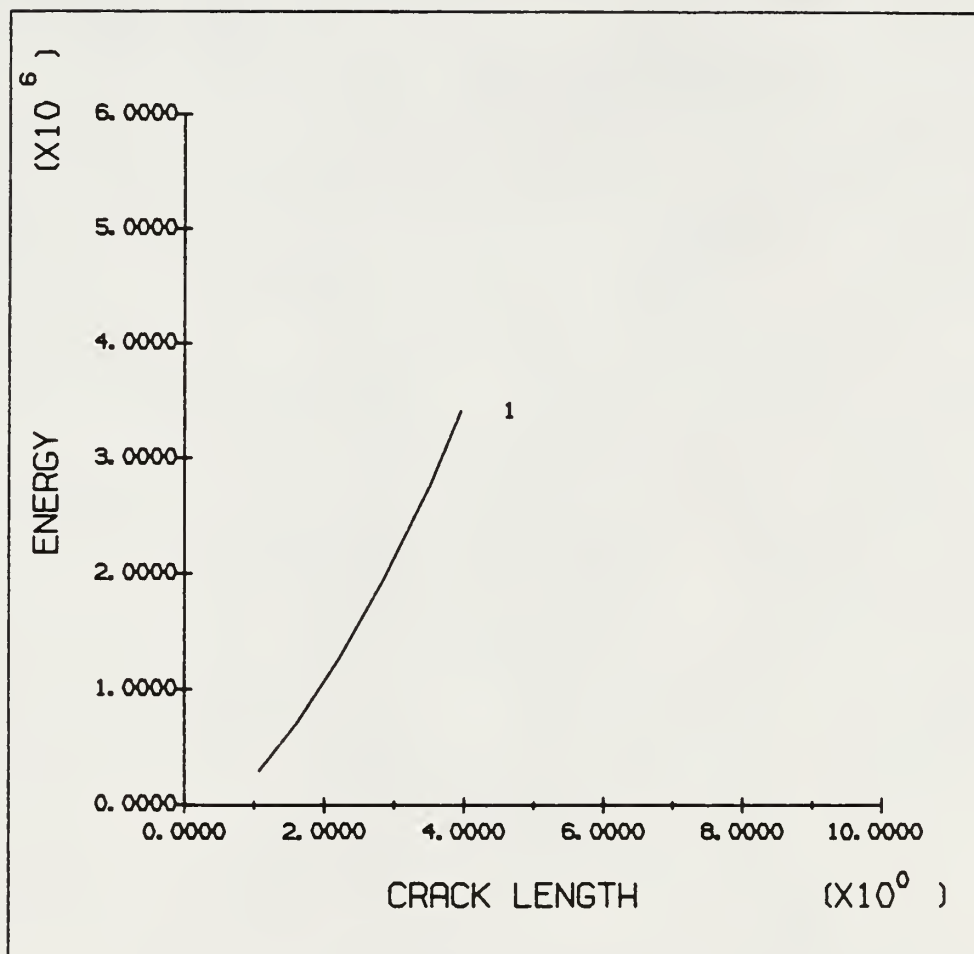


Figure 5.22: Crack Entrance Energy for Case 2

about 47% the length found in Case 1. This difference in fracture length is caused by heat transfer, seepage, and friction losses. Figures 5.23 and 5.24 show heat transfer and seepage losses. Note the decreasing values as a function of time. The loss mechanisms introduced in this case tend to convert more of the kinetic energy present at the crack mouth to internal energy. This results in the large variation of gas property values from the crack mouth to the crack tip. This can be seen in Figures 5.25 through 5.29 where gas properties are shown. While the pressures and temperatures at the crack mouth are higher than those found in Case 1, the velocities are lower illustrating this energy conversion. Figure 5.30 shows a plot of K_{ID} during propagation.

5.3 Case 3 - Specified Borehole Pressure With Friction In The Fracture Included ($\epsilon = 20\mu\text{m}$)

This case is identical to the previous case except that the effects of seepage and heat transfer are not included. By comparing these results to Case 2, we can determine the individual effect of friction, and the combined effect of heat transfer and seepage.

At 12 msec the crack length is about 7 meters. Plots of crack length and K_{ID} are shown in Figures 5.31 and 5.32. Again, the limit on crack velocity is a result of reduced gas flow into the crack. The displaced mesh is shown in Figure 5.33. Figure 5.34 shows the crack tip velocity during propagation. Figure 5.35 shows a crack entrance energy plot for Case 3. The slopes of this graph and the crack entrance energy plot for Case 2 are similar. This would imply that about the same percentage of the energy available in Case 3 is being

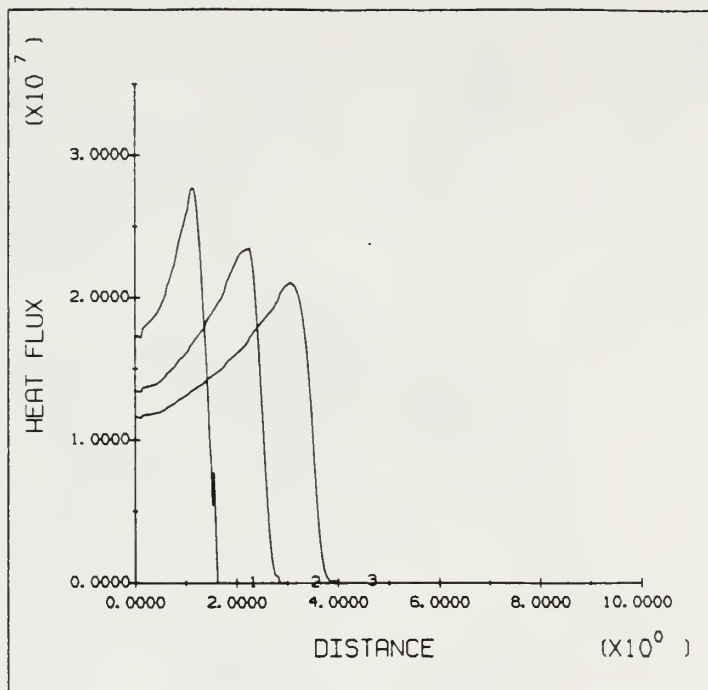


Figure 5.23: Heat Transfer Results for Case 2 at 6.5, 9.5, and 12 msec

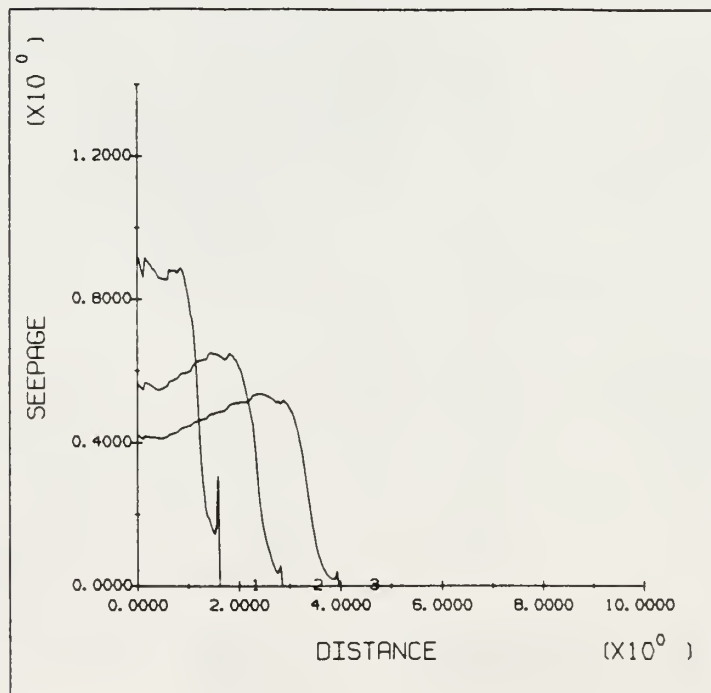


Figure 5.24: Seepage Results for Case 2 at 6.5, 9.5, and 12 msec

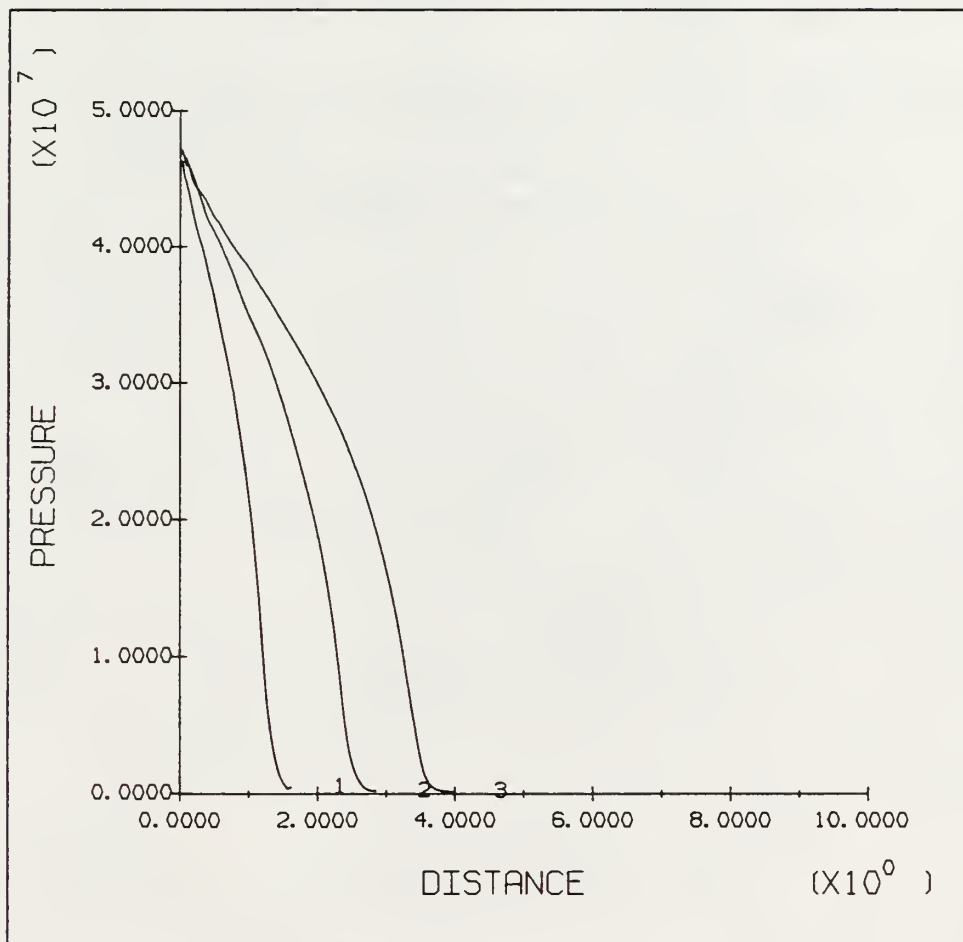


Figure 5.25: Gas Pressure for Case 2 at 6.5, 9.5, and 12 msec

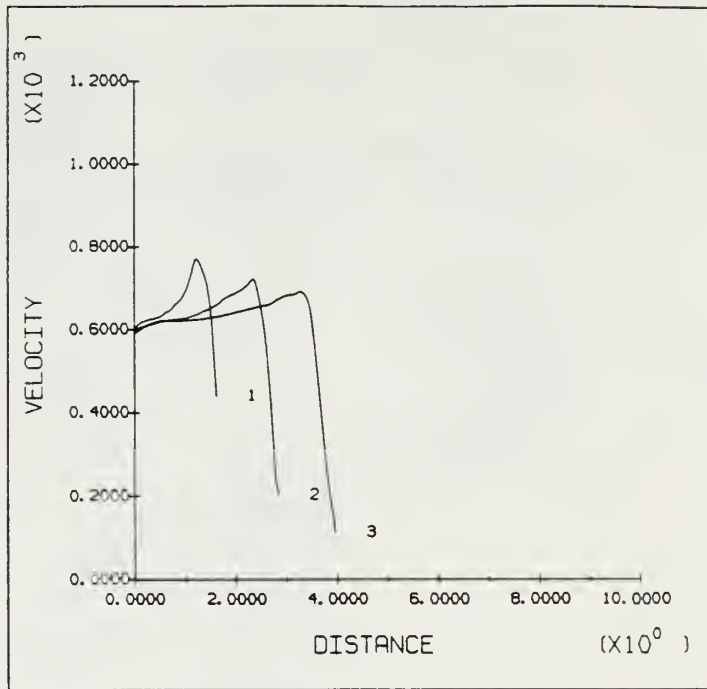


Figure 5.26: Gas Velocity for Case 2 at 6.5, 9.5, and 12 msec

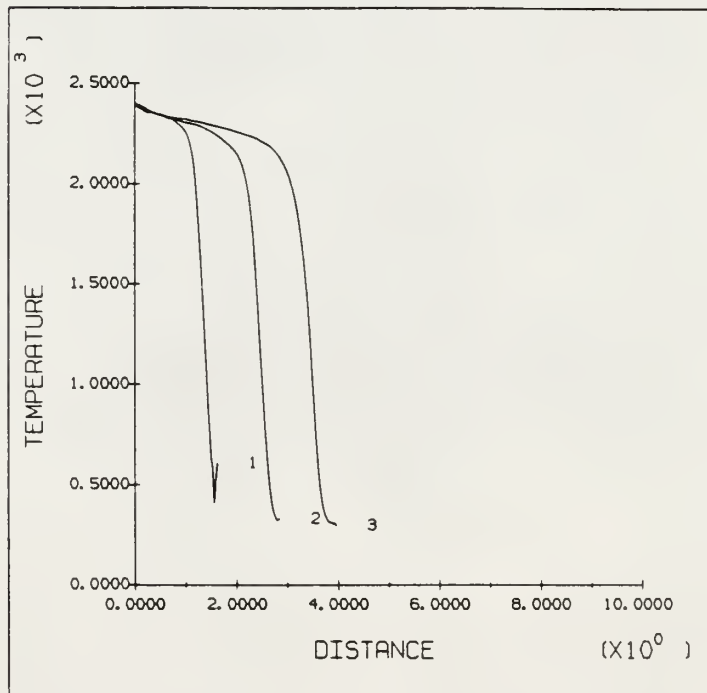


Figure 5.27: Gas Temperature for Case 2 at 6.5, 9.5, and 12 msec

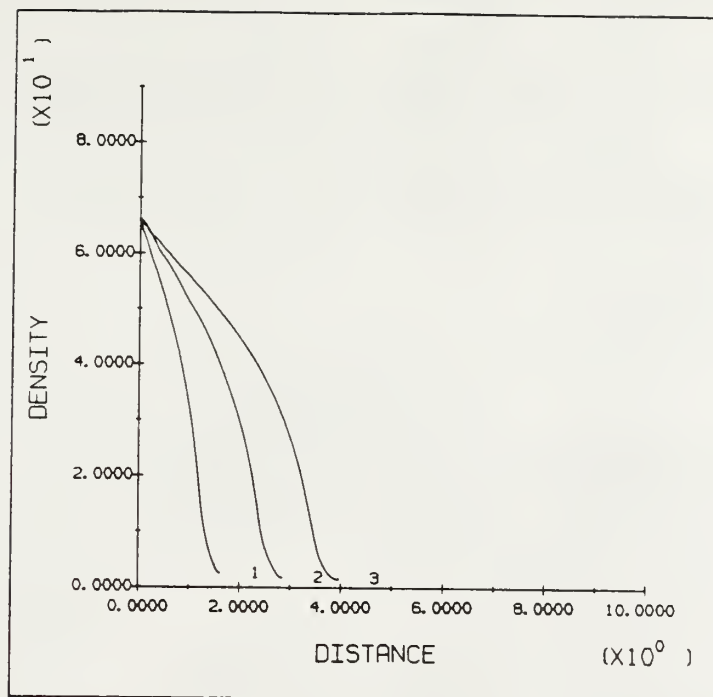


Figure 5.28: Gas Density for Case 2 at 6.5, 9.5, and 12 msec

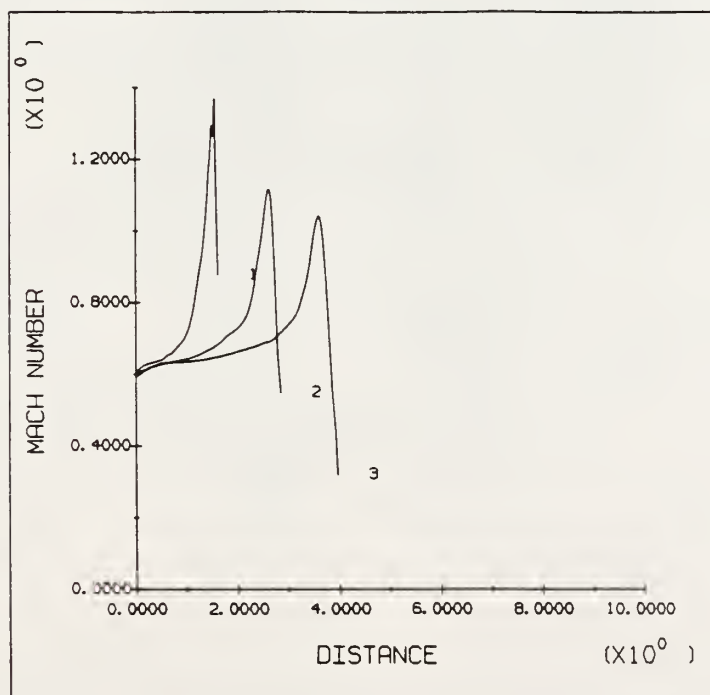


Figure 5.29: Mach Number for Case 2 at 6.5, 9.5, and 12 msec

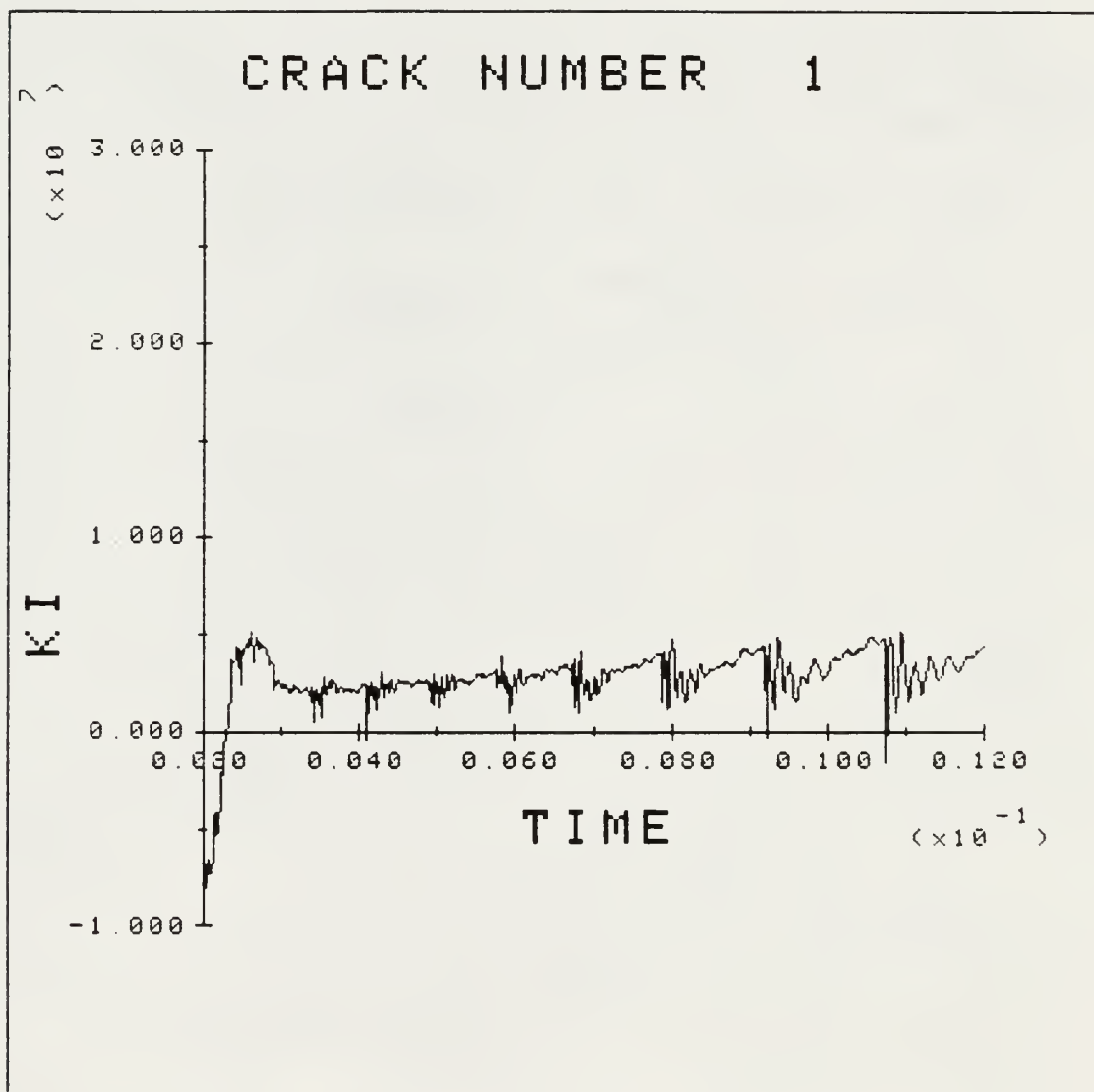


Figure 5.30: KID During Propagation for Case 2

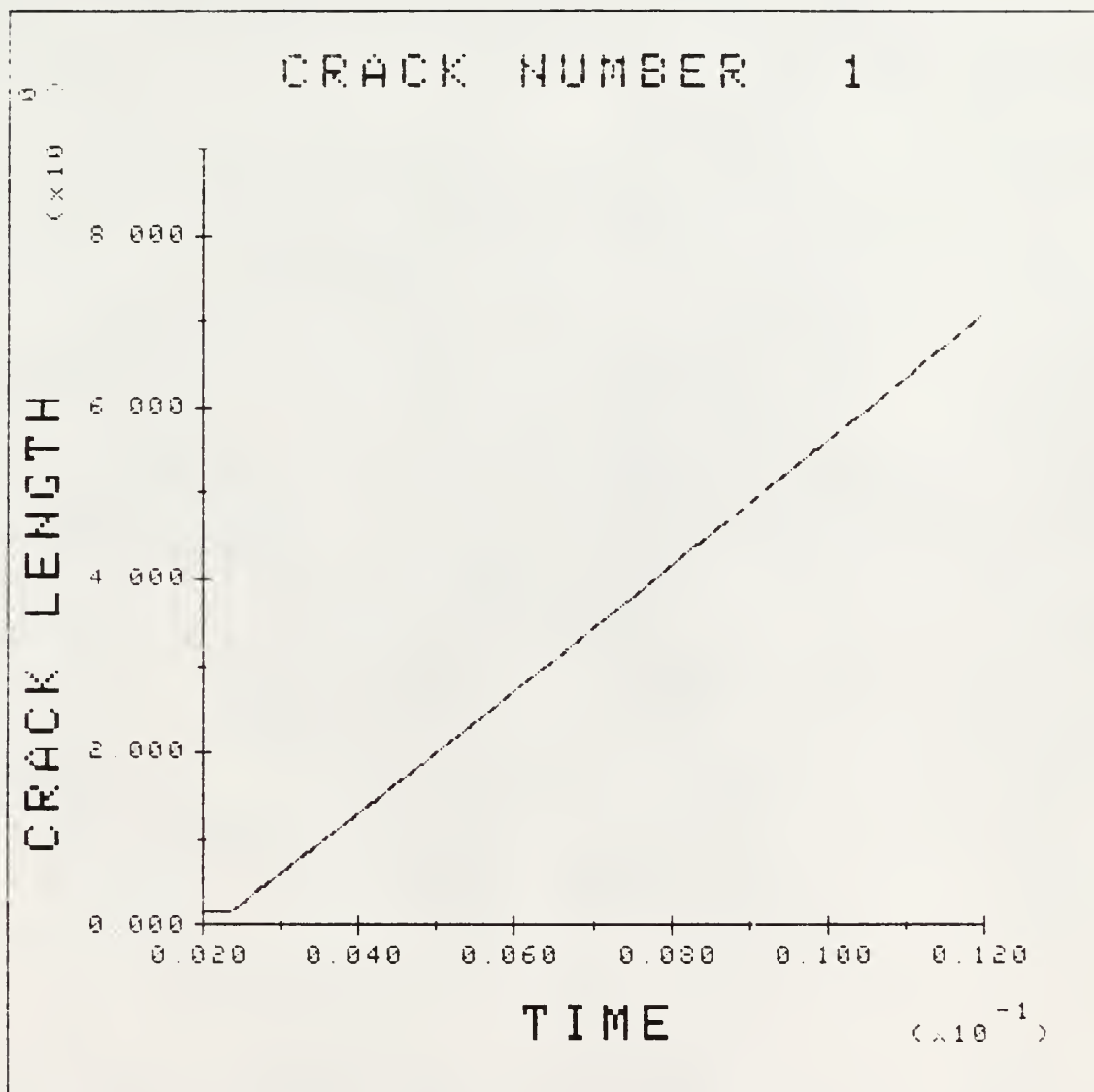


Figure 5.31: Crack Length for Case 3

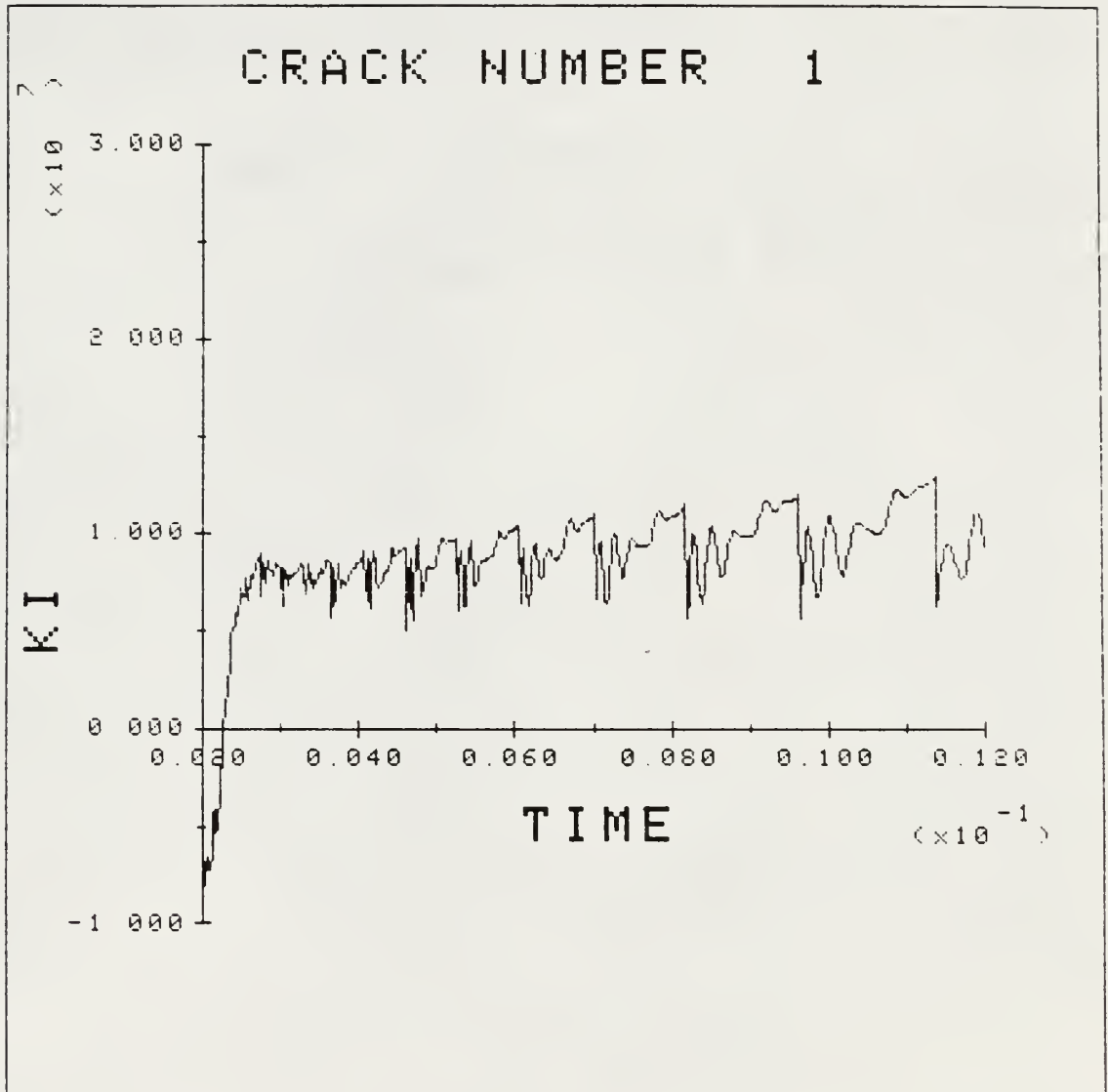


Figure 5.32: KID During Propagation for Case 3

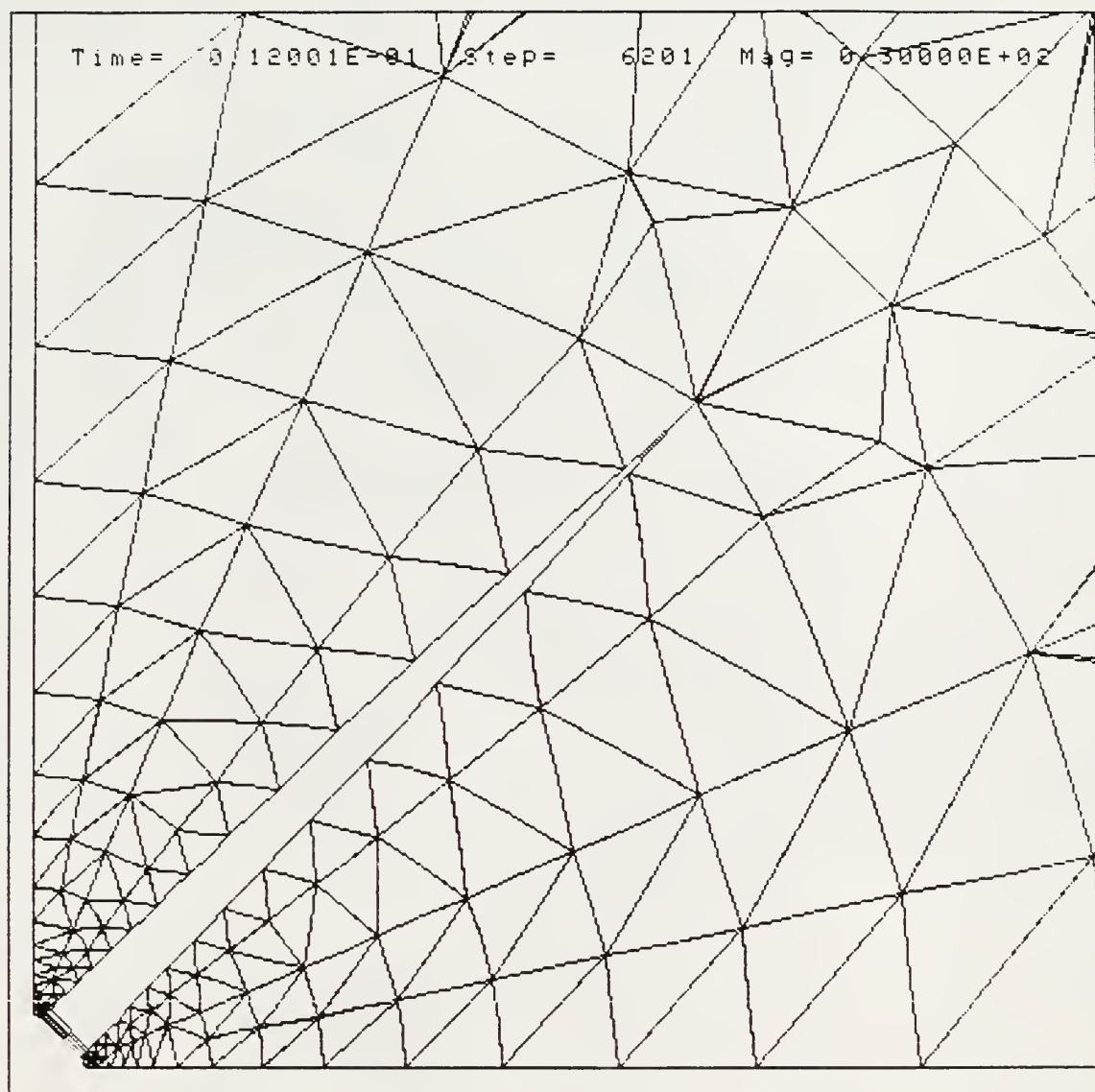


Figure 5.33: Displaced Mesh Results for Case 3 at 12 msec

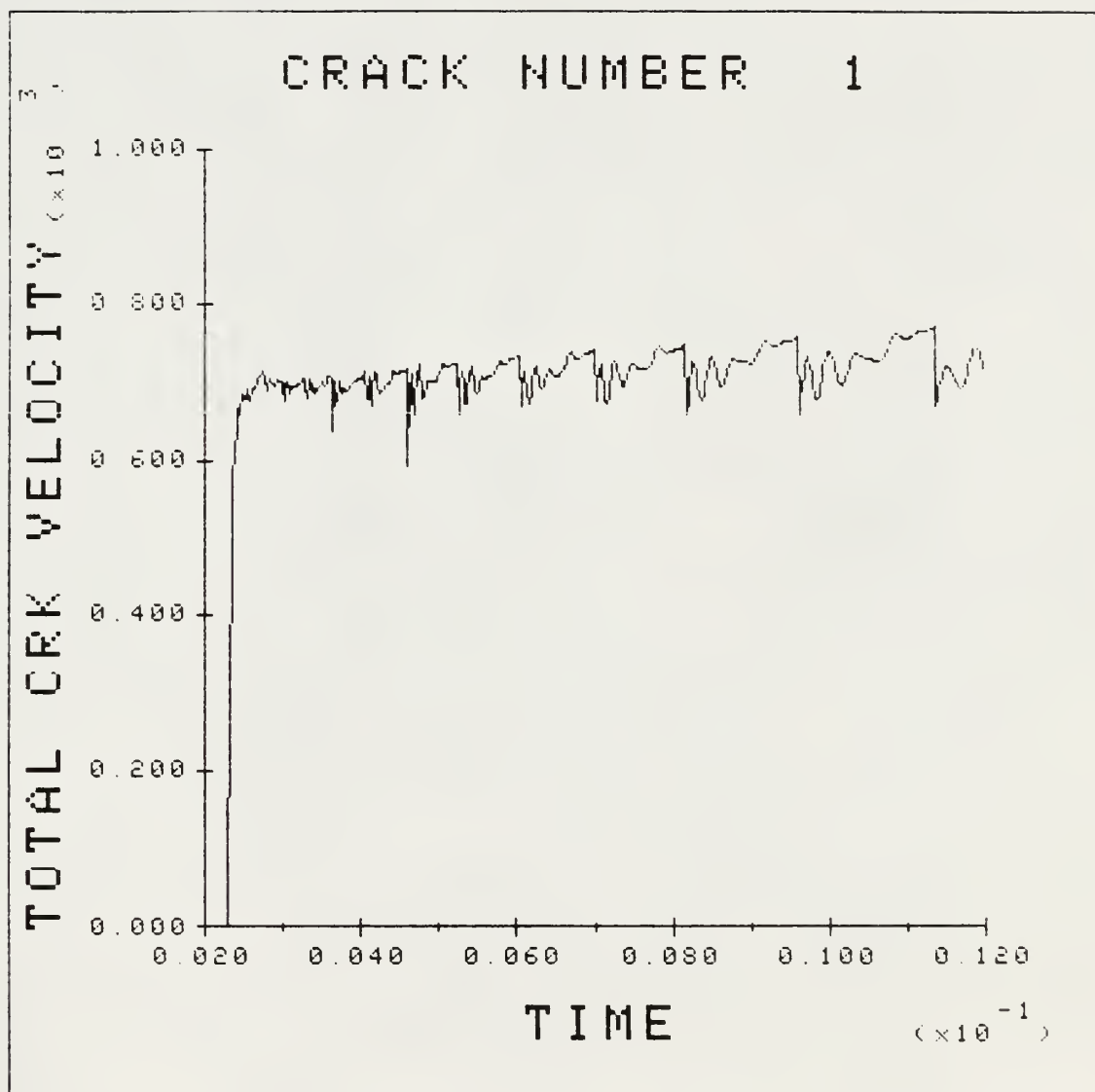


Figure 5.34: Crack Velocity for Case 3

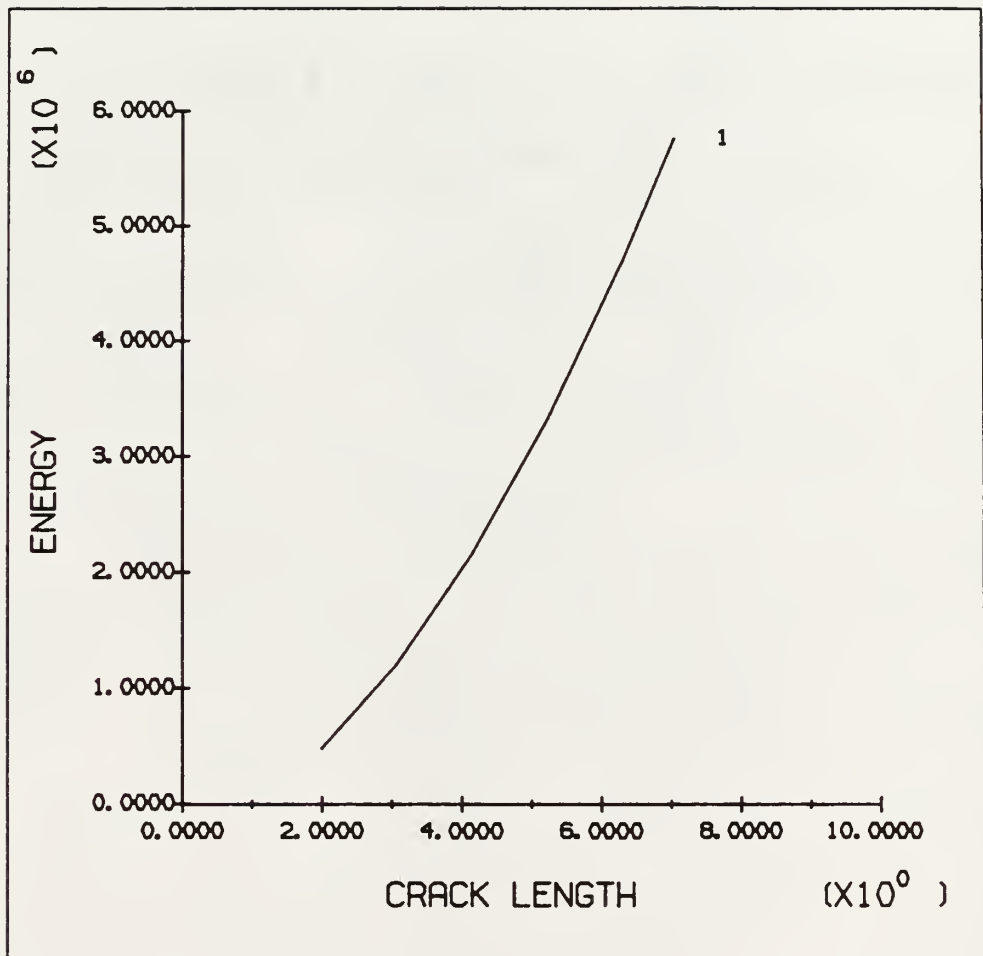


Figure 5.35: Crack Entrance Energy for Case 3

converted to kinetic and internal energy. This should result in similar gas property plots as can be seen in Figures 5.36 through 5.40.

When comparing Cases 2 & 3, it can be seen that seepage and heat transfer have a greater effect on crack length than does friction alone (for the current parameters). This effect should become less dominant at later times since there is an inverse time relationship for both losses.

5.4 Case 4 - Specified Borehole Pressure With Friction In The Fracture Included ($\epsilon = 4\mu\text{m}$)

This case is identical to Case 3 except a smaller roughness is used in the friction factor calculations. The displaced mesh for Case 4 is shown in Figure 5.41. The crack is about 7.3 meters long and the crack opening displacement at the borehole is about .0134 meters. Crack length and opening results are shown in Figure 5.42 and 5.43. K_{ID} during propagation is shown in Figure 5.44. Crack tip velocity results are shown in Figure 5.45. Referring to Eqn 2.36, it can be seen that a factor of five decrease could result in a greater than two decrease in the friction factor, for predominantly turbulent flow. The turbulent term should dominate for the cases examined in this thesis. The decreased roughness has a minimal effect on the pressure, but has less than minimal effect on the temperature when compared to Case 3. Figures 5.46 through 5.50 show the gas properties at various times for Case 4. This effect is due to the fact that an ideal gas is assumed and a small change in pressure will have a large effect on the

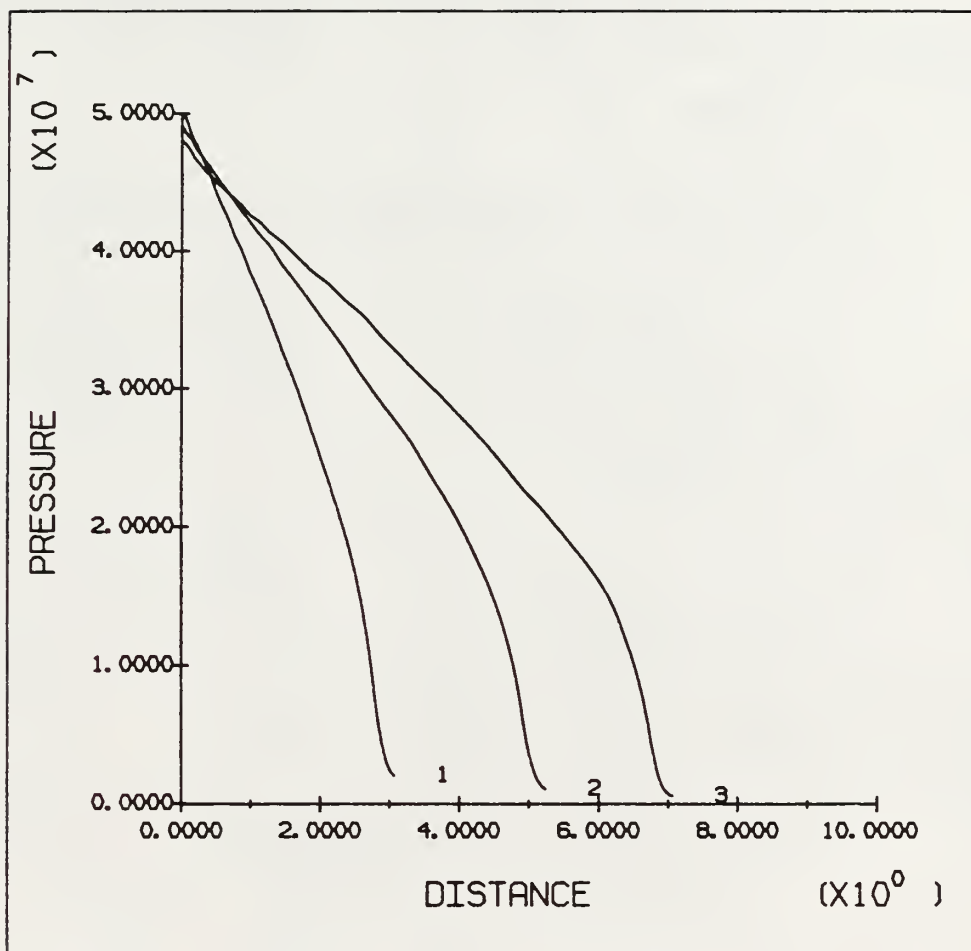


Figure 5.36: Gas Pressure for Case 3 at 6.5, 9.5, and 12 msec

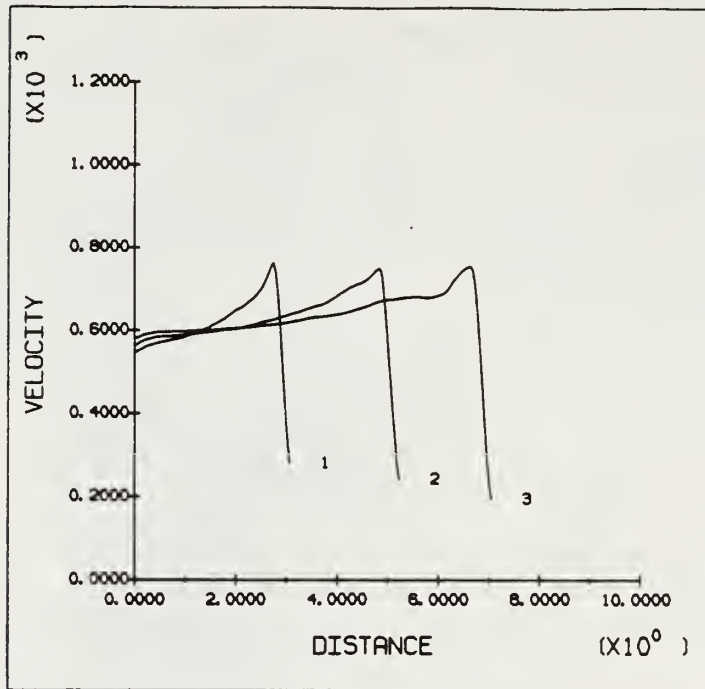


Figure 5.37: Gas Velocity for Case 3 at 6.5, 9.5, and 12 msec

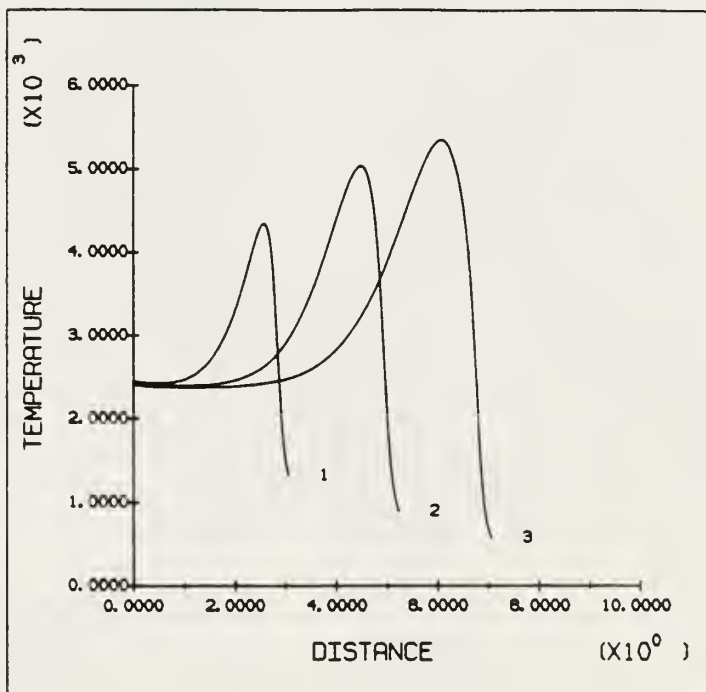


Figure 5.38: Gas Temperature for Case 3 at 6.5, 9.5, and 12 msec

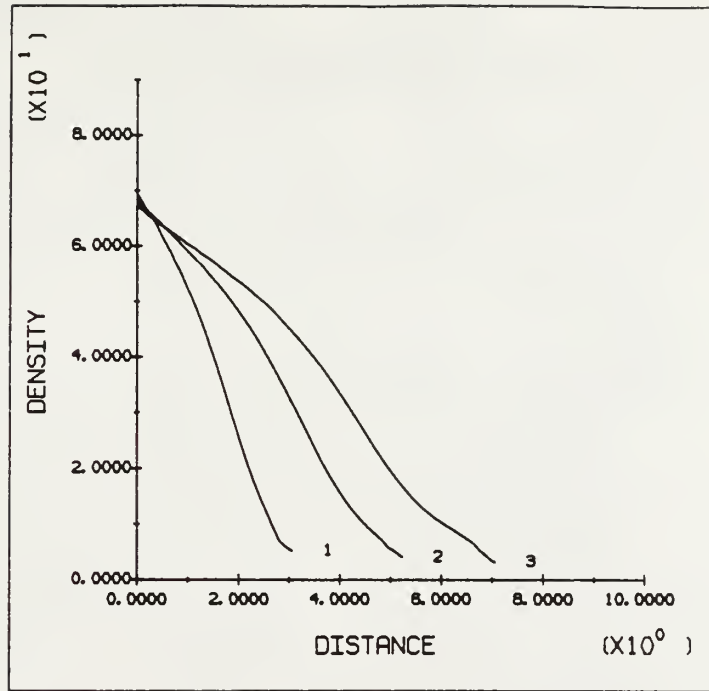


Figure 5.39: Gas Density for Case 3 at 6.5, 9.5, and 12 msec

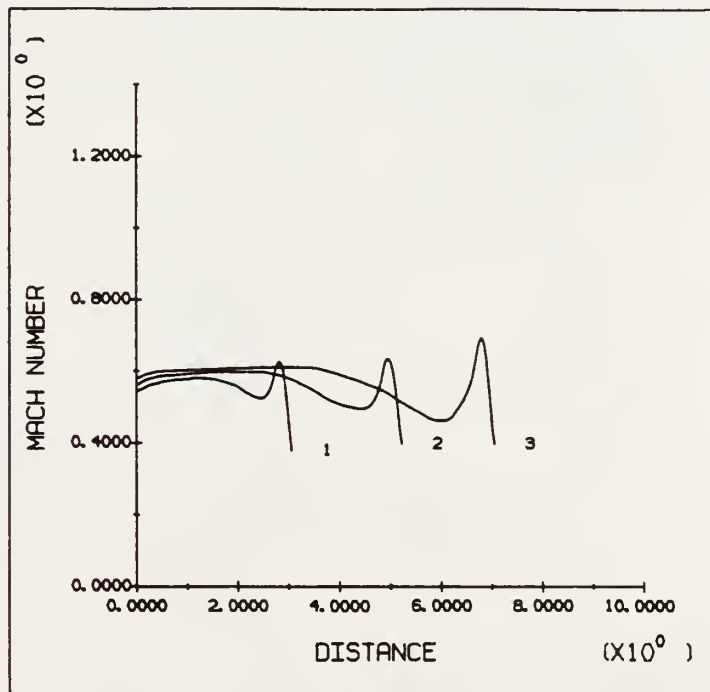


Figure 5.40: Mach Number for Case 3 at 6.5, 9.5, and 12 msec

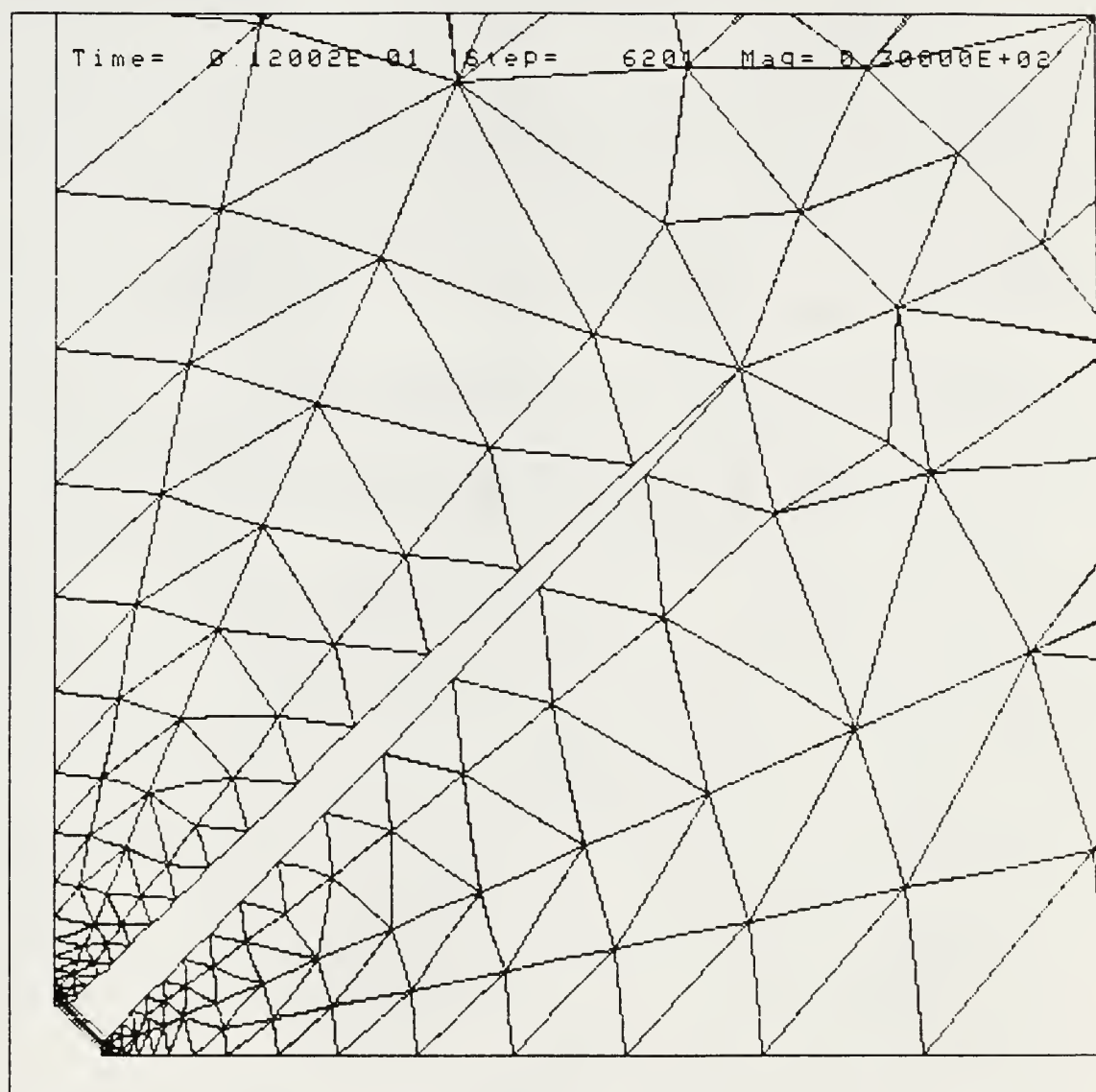


Figure 5.41: Displaced Mesh Results for Case 4 at 12 msec

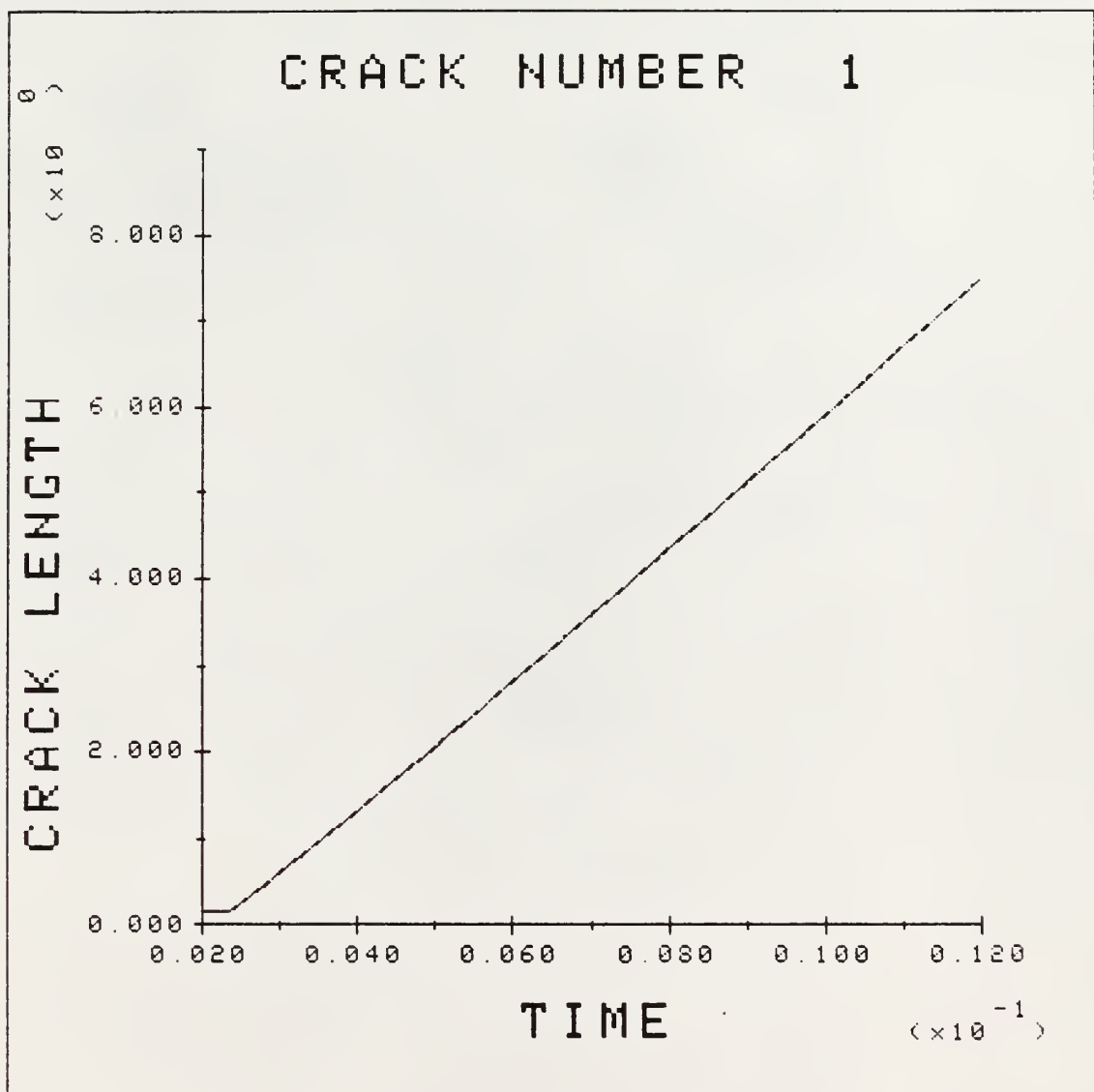


Figure 5.42: Crack Length for Case 4

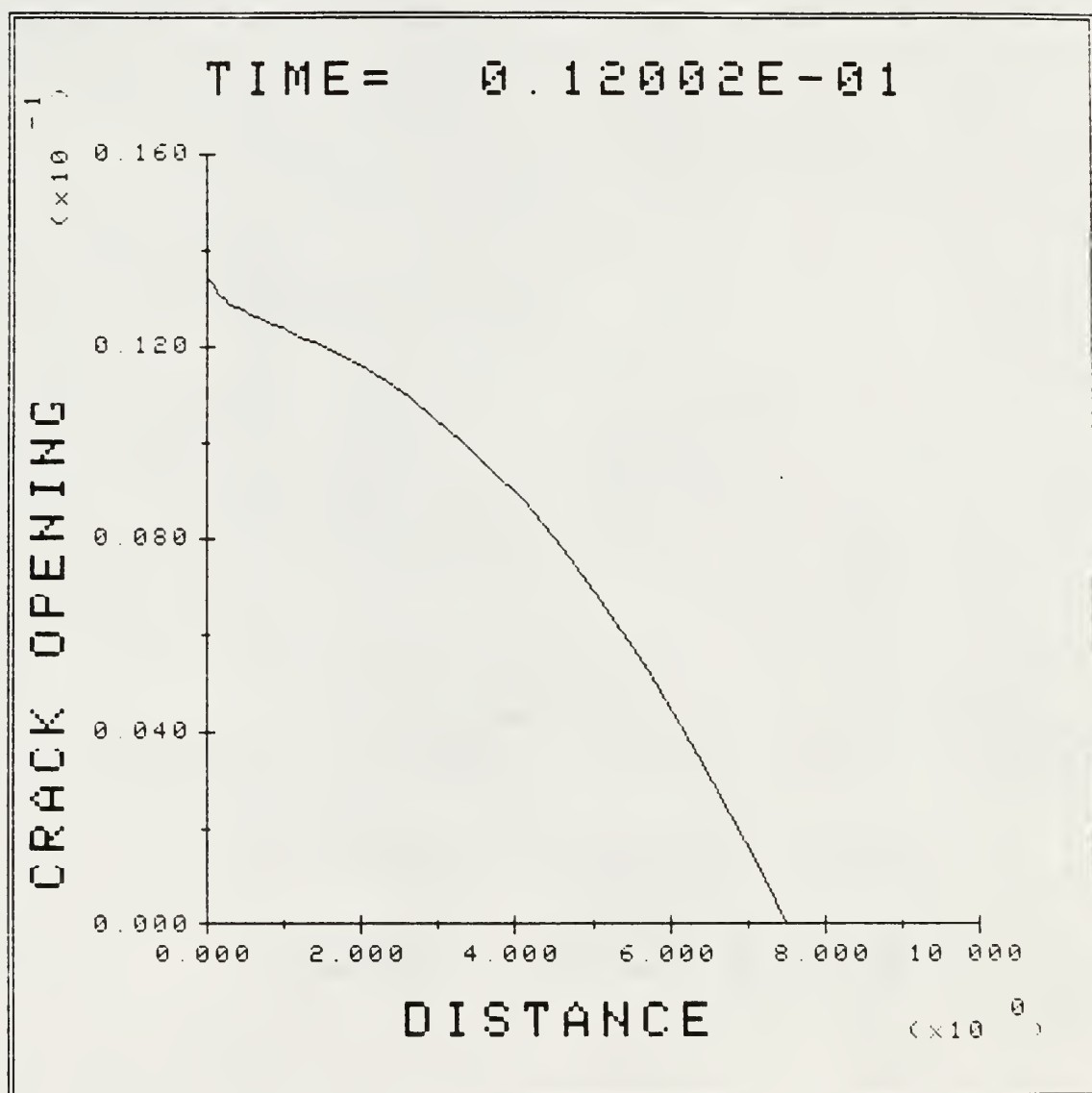


Figure 5.43: Crack Opening Displacement for Case 4 at 12 msec

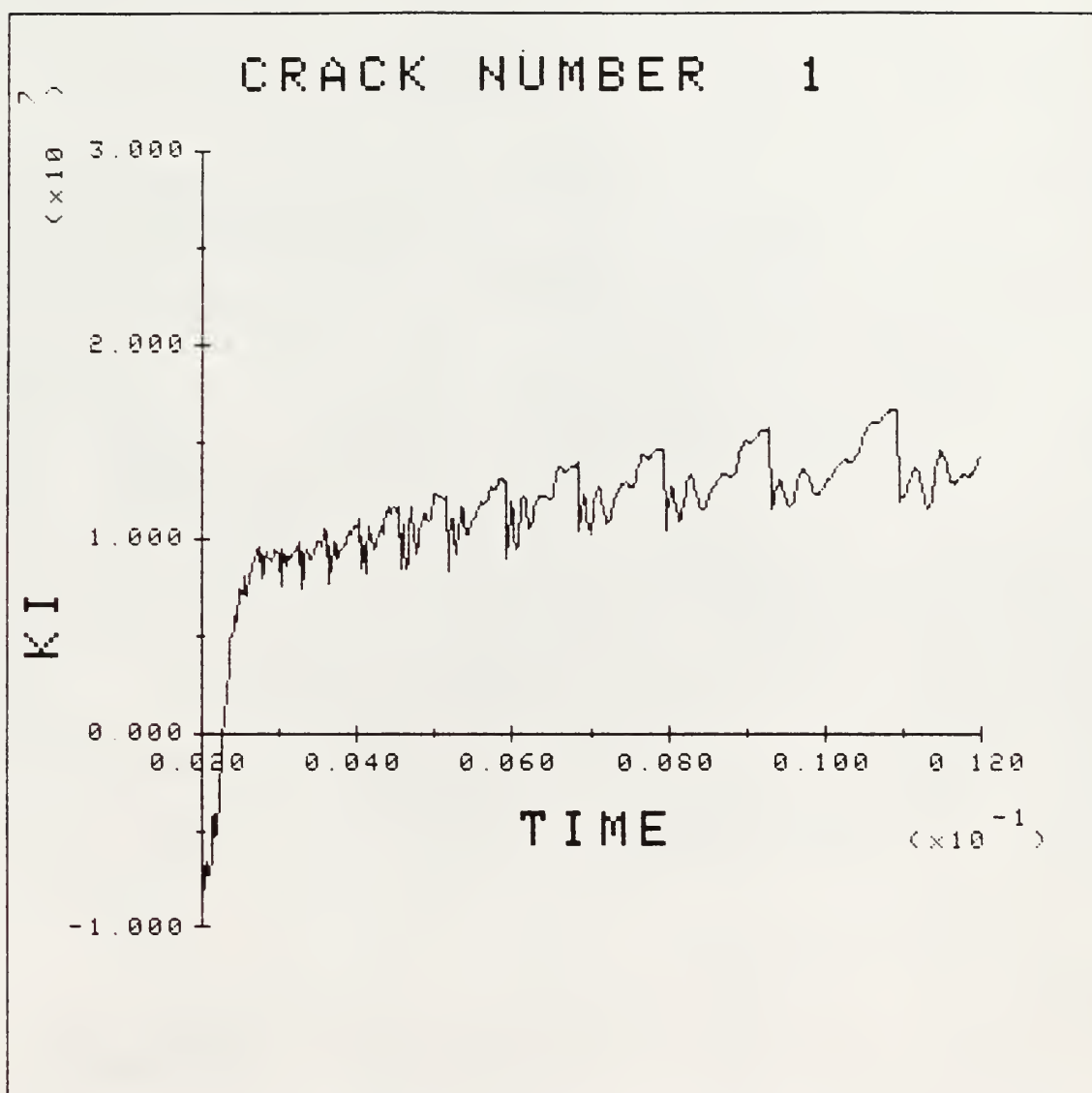


Figure 5.44: KID During Propagation for Case 4

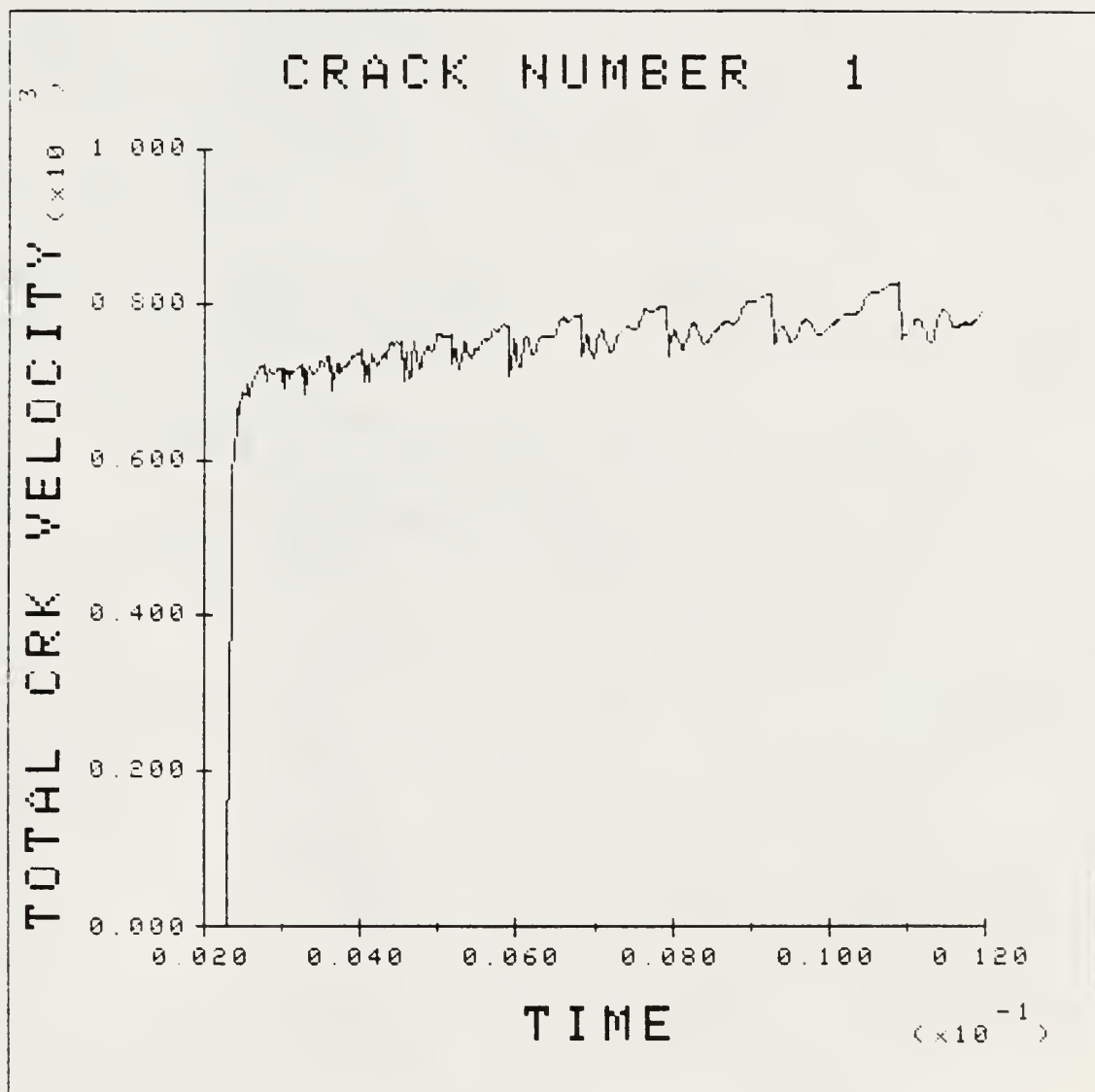


Figure 5.45: Crack Velocity for Case 4

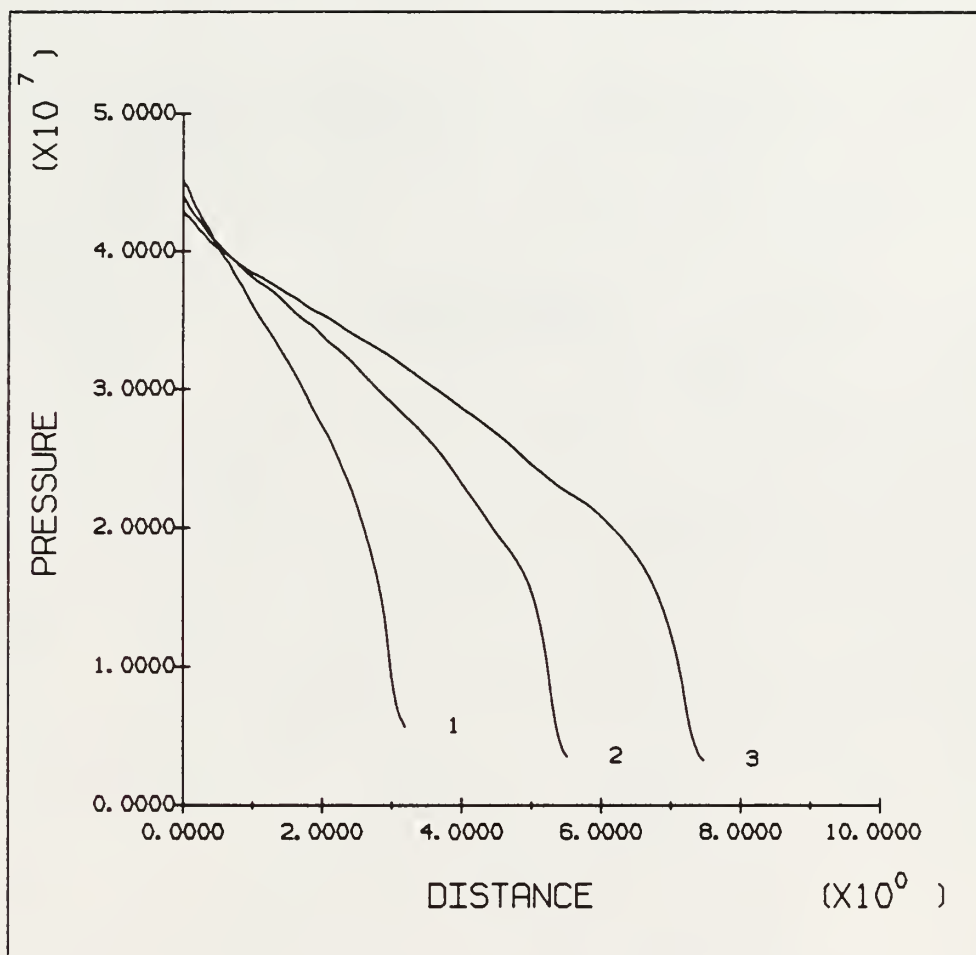


Figure 5.46: Gas Pressure for Case 4 at 6.5, 9.5, and 12 msec

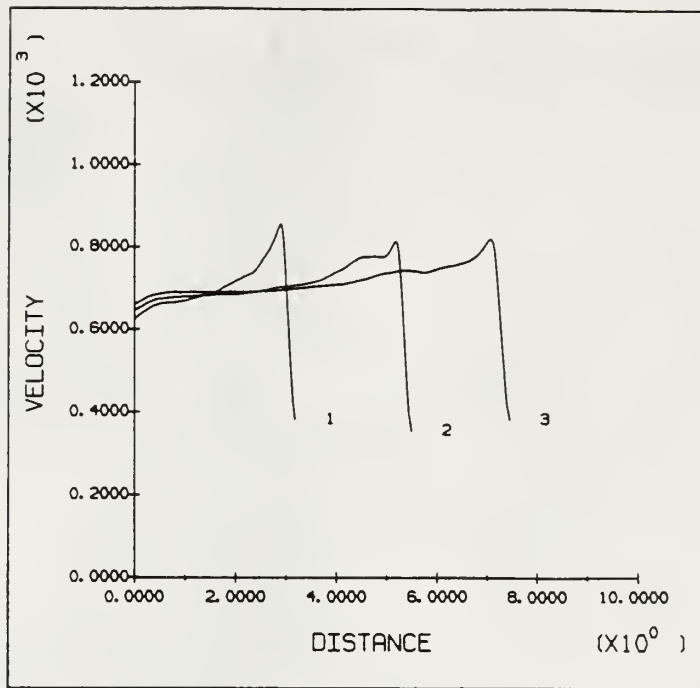


Figure 5.47: Gas Velocity for Case 4 at 6.5, 9.5, and 12 msec

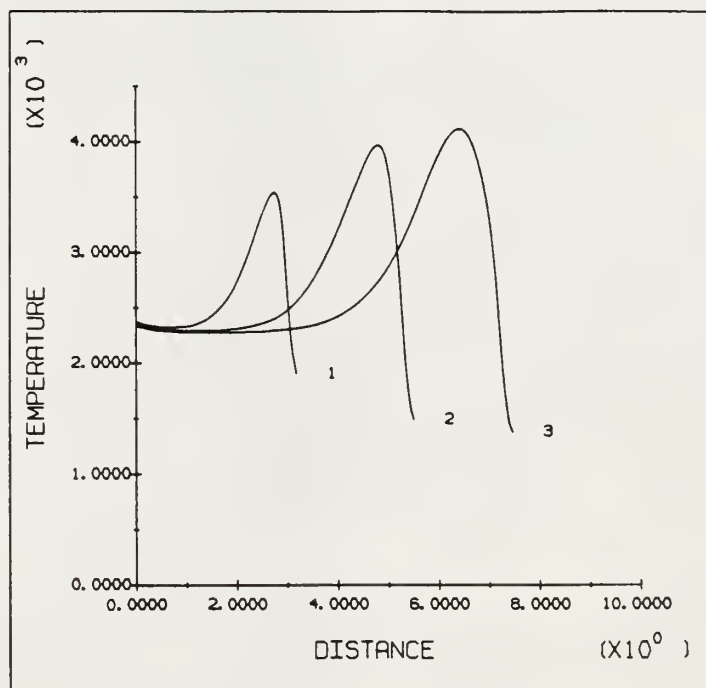


Figure 5.48: Gas Temperature for Case 4 at 6.5, 9.5, and 12 msec

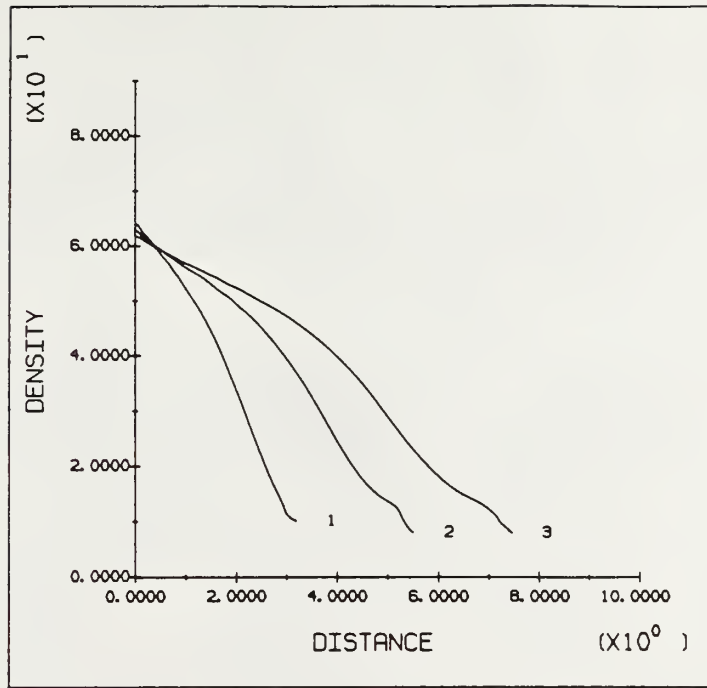


Figure 5.49: Gas Density for Case 4 at 6.5, 9.5, and 12 msec

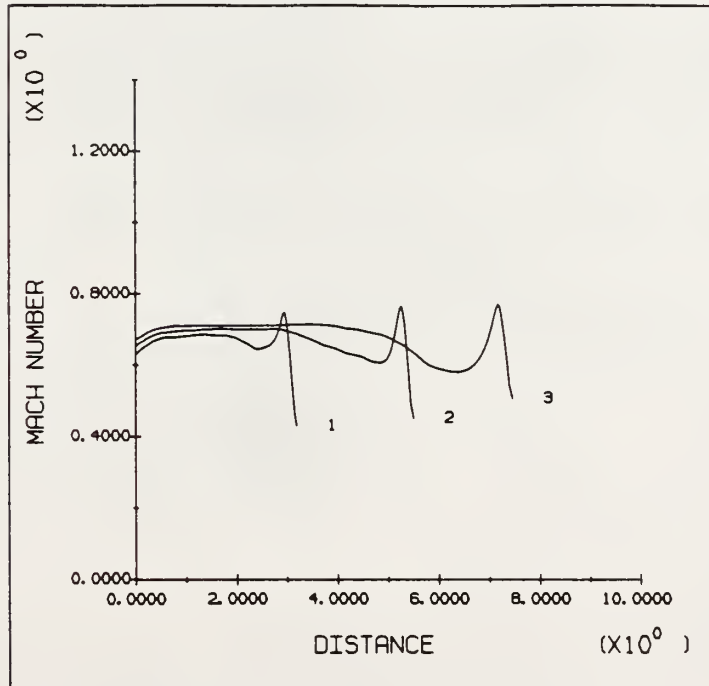


Figure 5.50: Mach Number for Case 4 at 6.5, 9.5, and 12 msec

temperature. Since the pressures away from the crack mouth are slightly higher for Case 4, the temperatures are higher. This stored energy will have an effect later in the analysis. However, at this point in time the similar pressure distributions for both cases will result in similar crack lengths. The crack entrance energy plot is shown in Figure 5.51.

5.5 Case 5 - Burn Model With Friction, Heat Transfer, And Seepage Included

Case 5 is similar to Case 2 since all losses are included. However, this case attempts to model a real problem by using a propellant burn model. Propellant properties are found in Table 5.2. The displaced mesh is shown in Figure 5.52. At 12 msec, the crack is about 4.0 meters long and the crack opening displacement at the borehole is about 0.0045 meters. Plots of crack opening and length are shown in Figures 5.53 and 5.54. The borehole pressure history is shown in Figure 5.55. While the borehole pressure is increasing, the crack tip velocity, Figure 5.56, and K_{ID} , Figure 5.57, are also increasing. After the borehole pressure peaks at 60 msec, the crack tip velocity and K_{ID} also peak and decrease. If the borehole pressure were allowed to decrease further, crack arrest would occur. To prevent this, the borehole pressure should probably be maintained above 50 MPa.

The gas plots are shown in Figures 5.58 through 5.64. As is typical of the cases with losses included, there is large variation of properties from the crack mouth to the crack tip.

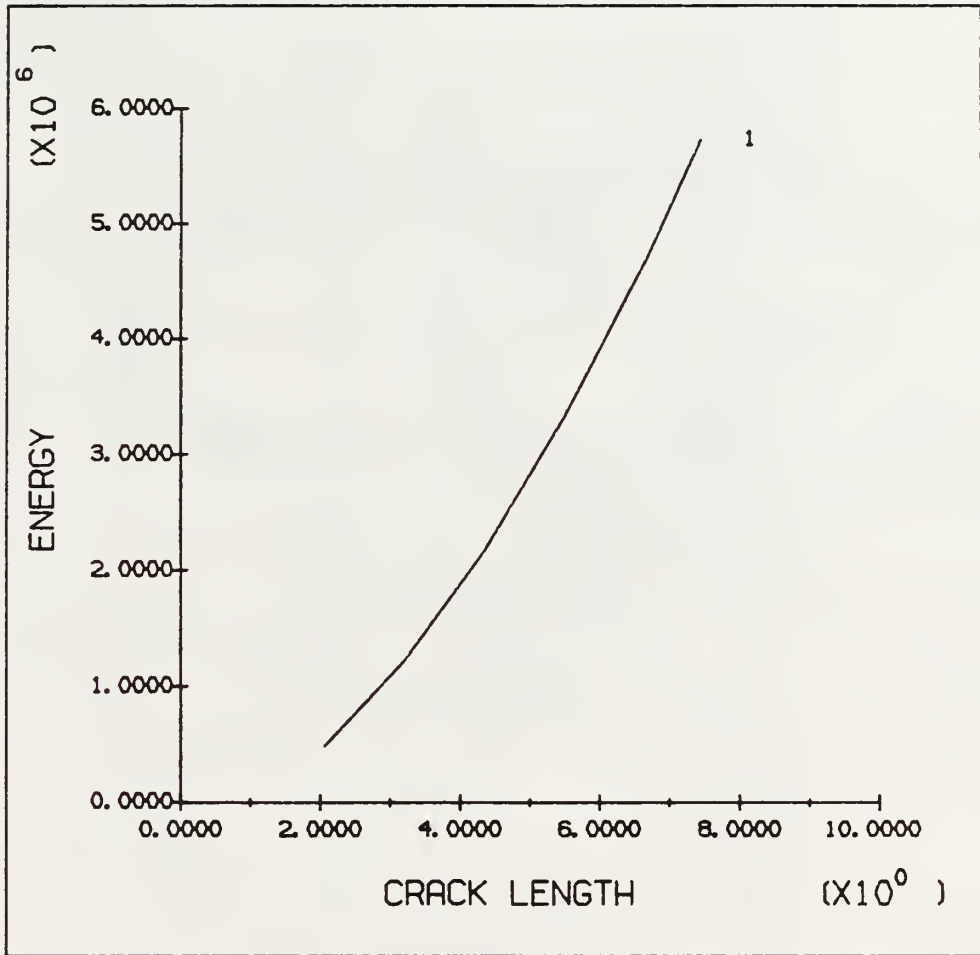


Figure 5.51: Crack Entrance Energy for Case 4

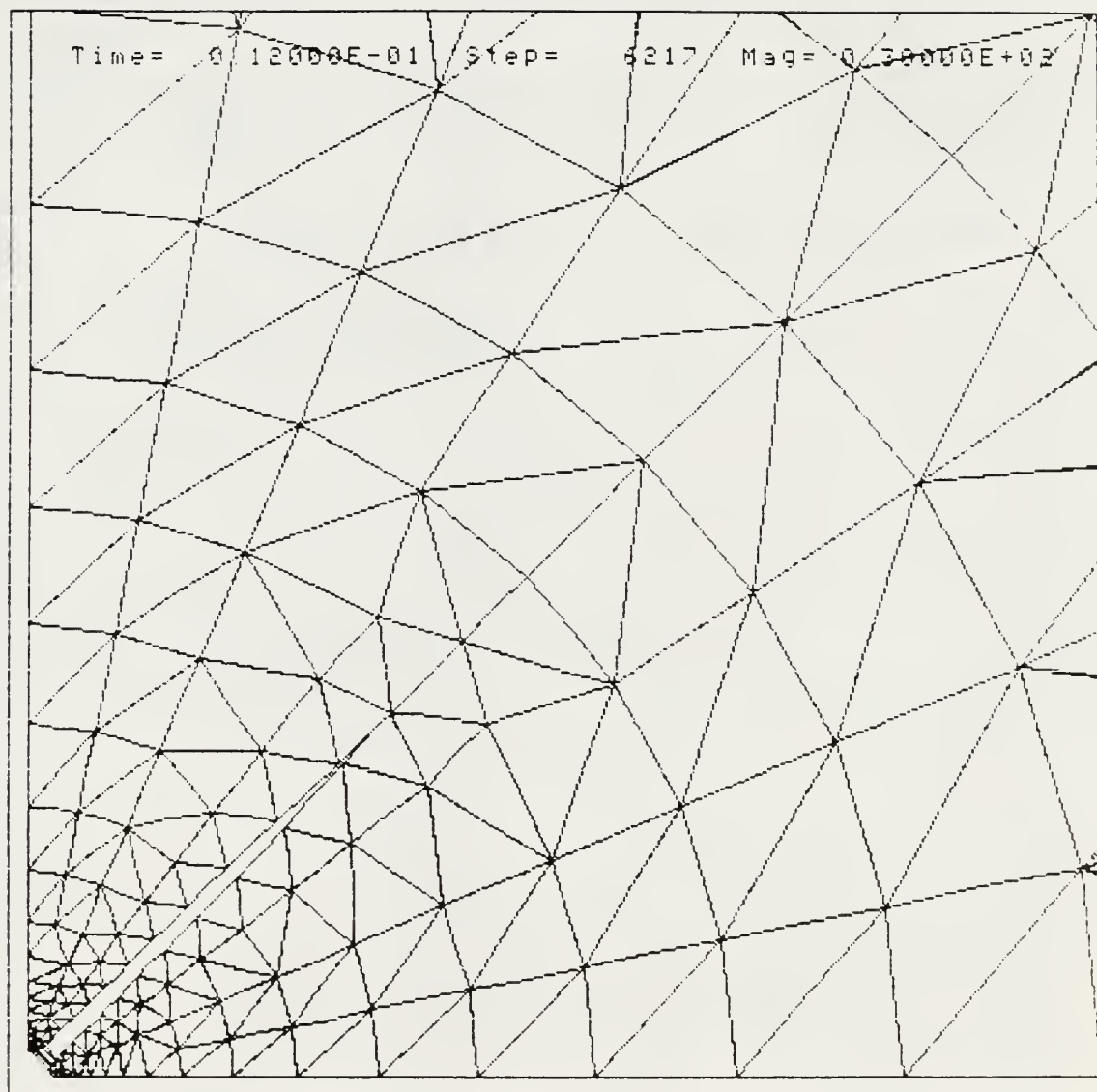


Figure 5.52: Displaced Mesh Results for Case 5 at 12 msec

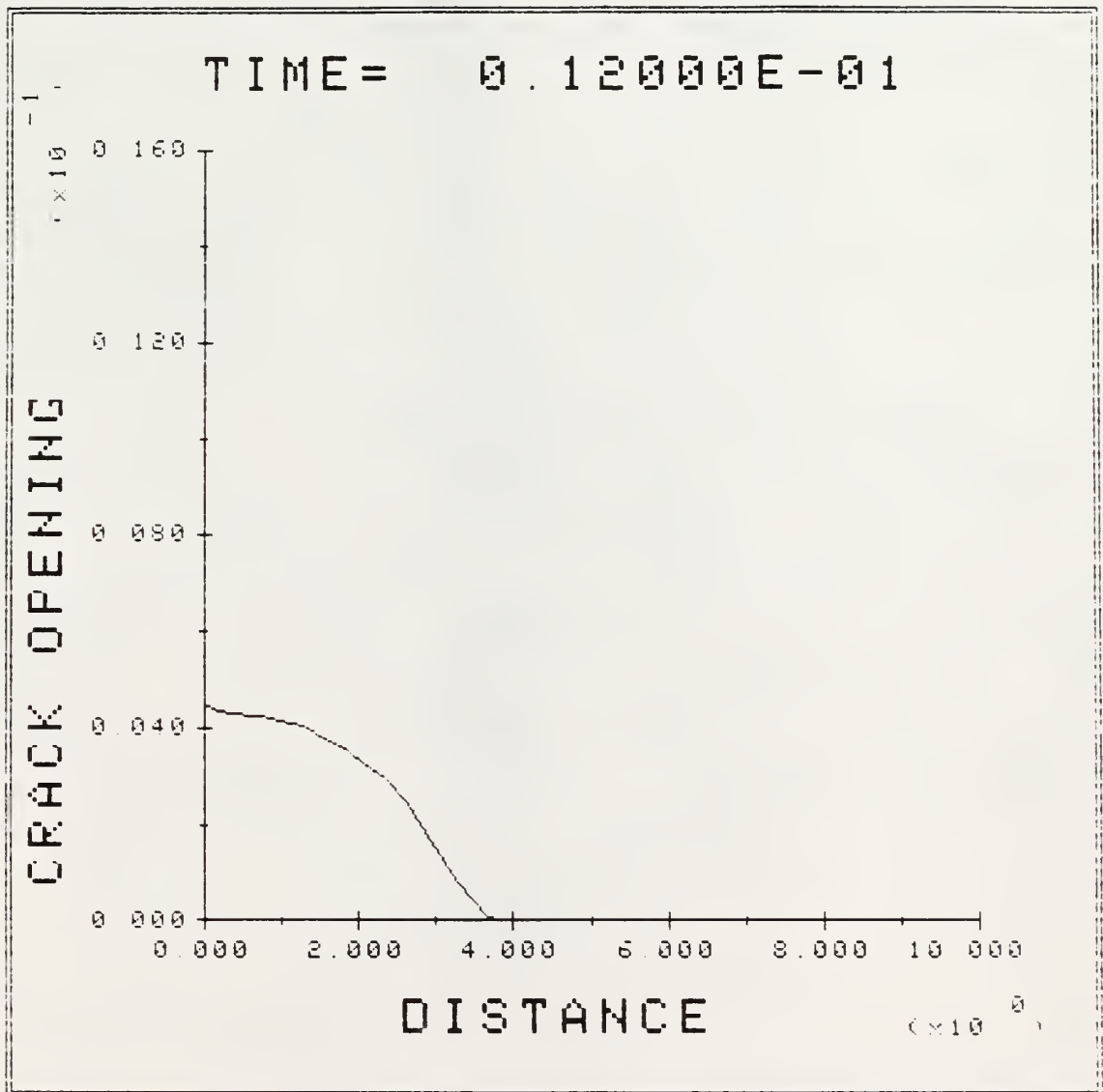


Figure 5.53: Crack Opening Displacement for Case 5 at 12 msec

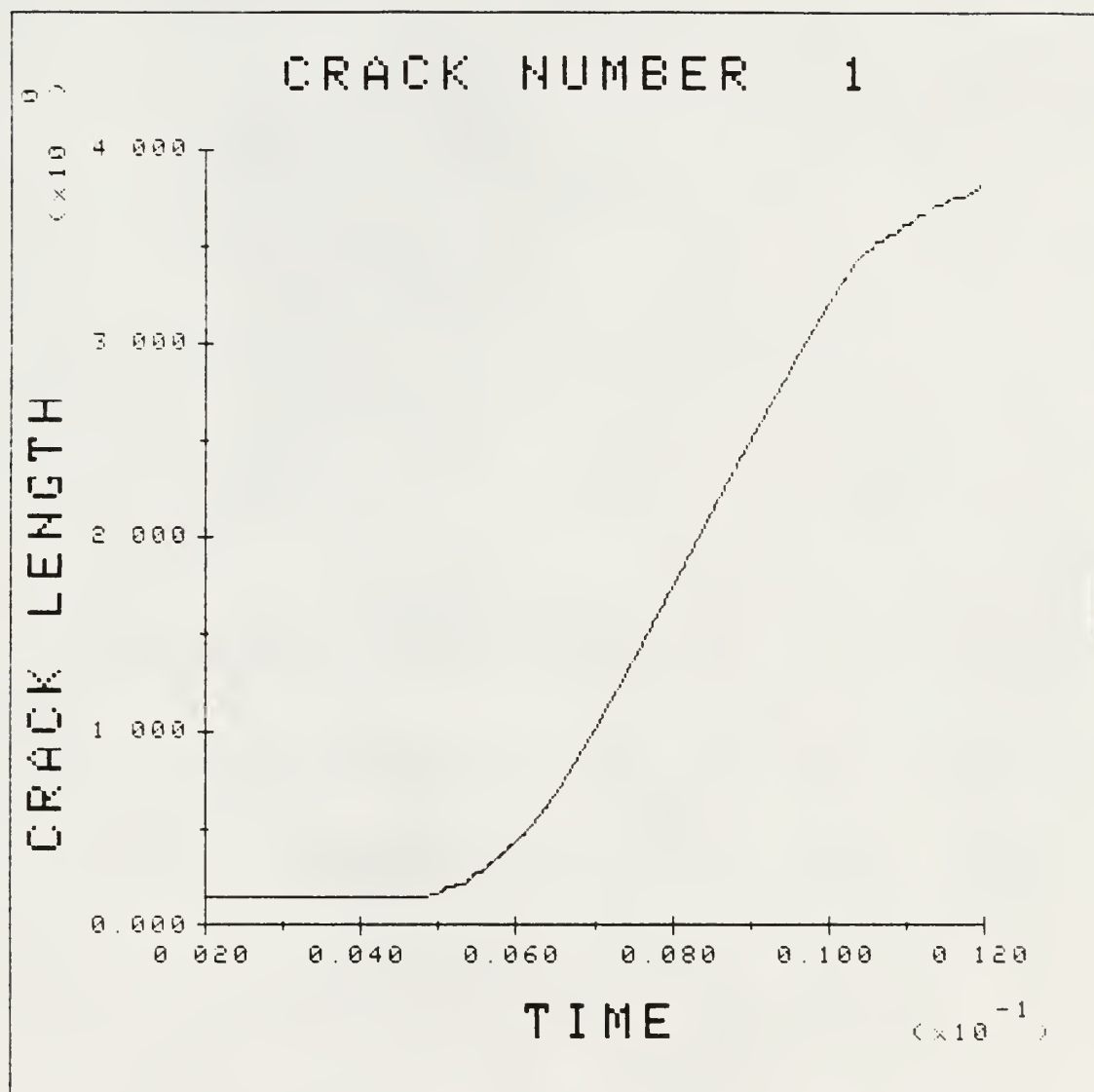


Figure 5.54: Crack Length for Case 5

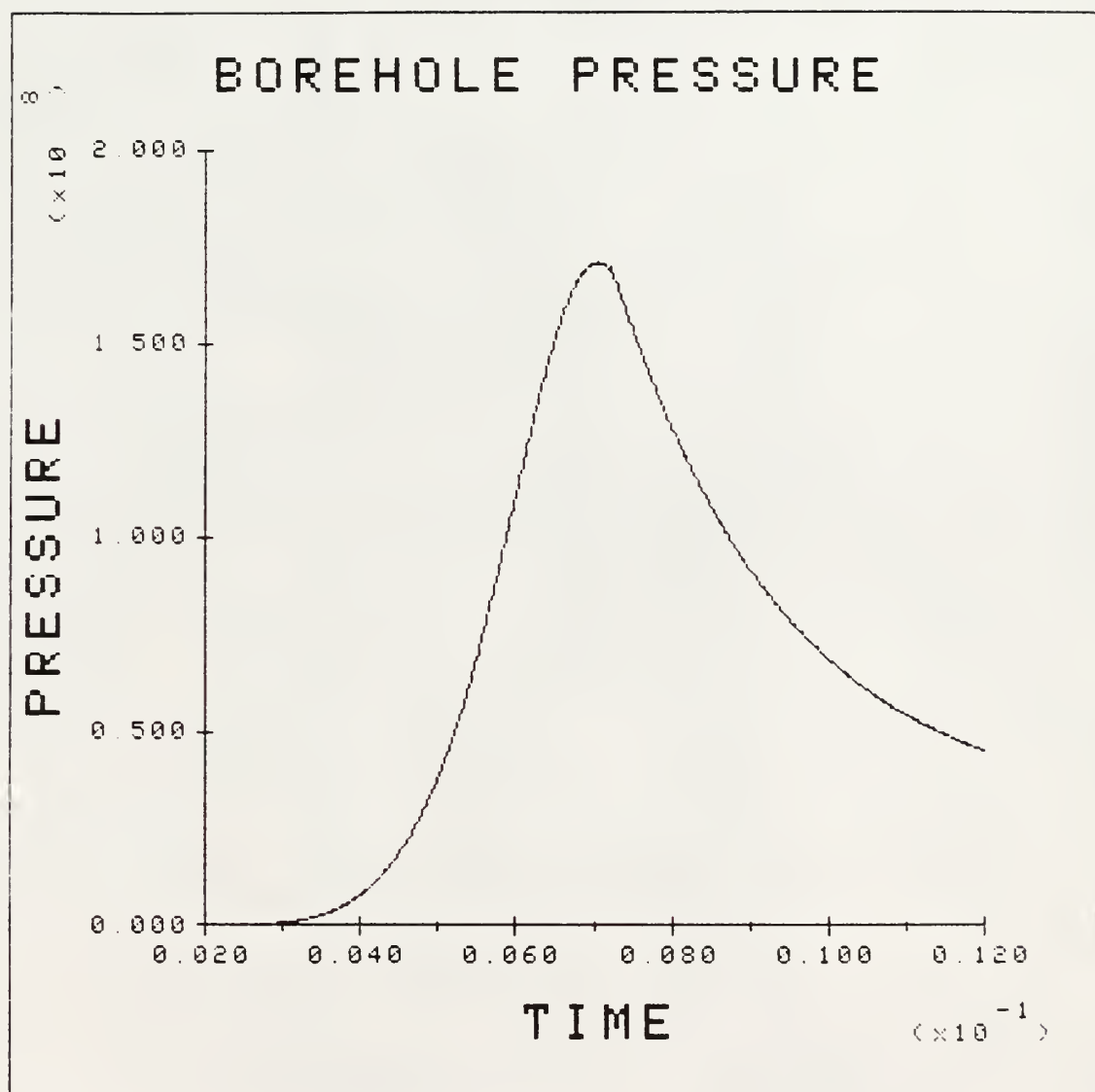


Figure 5.55: Borehole Pressure History

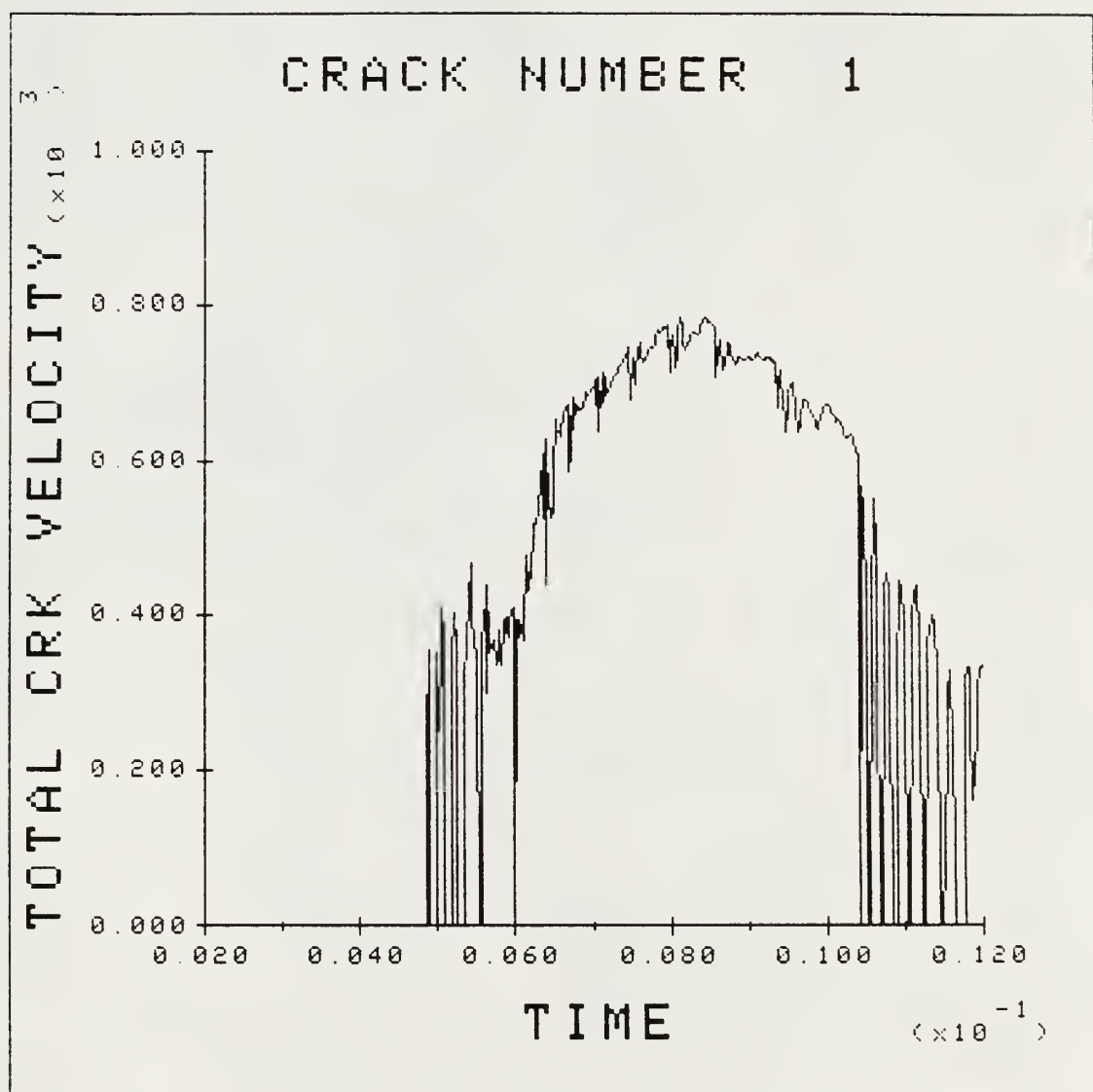


Figure 5.56: Crack Velocity for Case 5

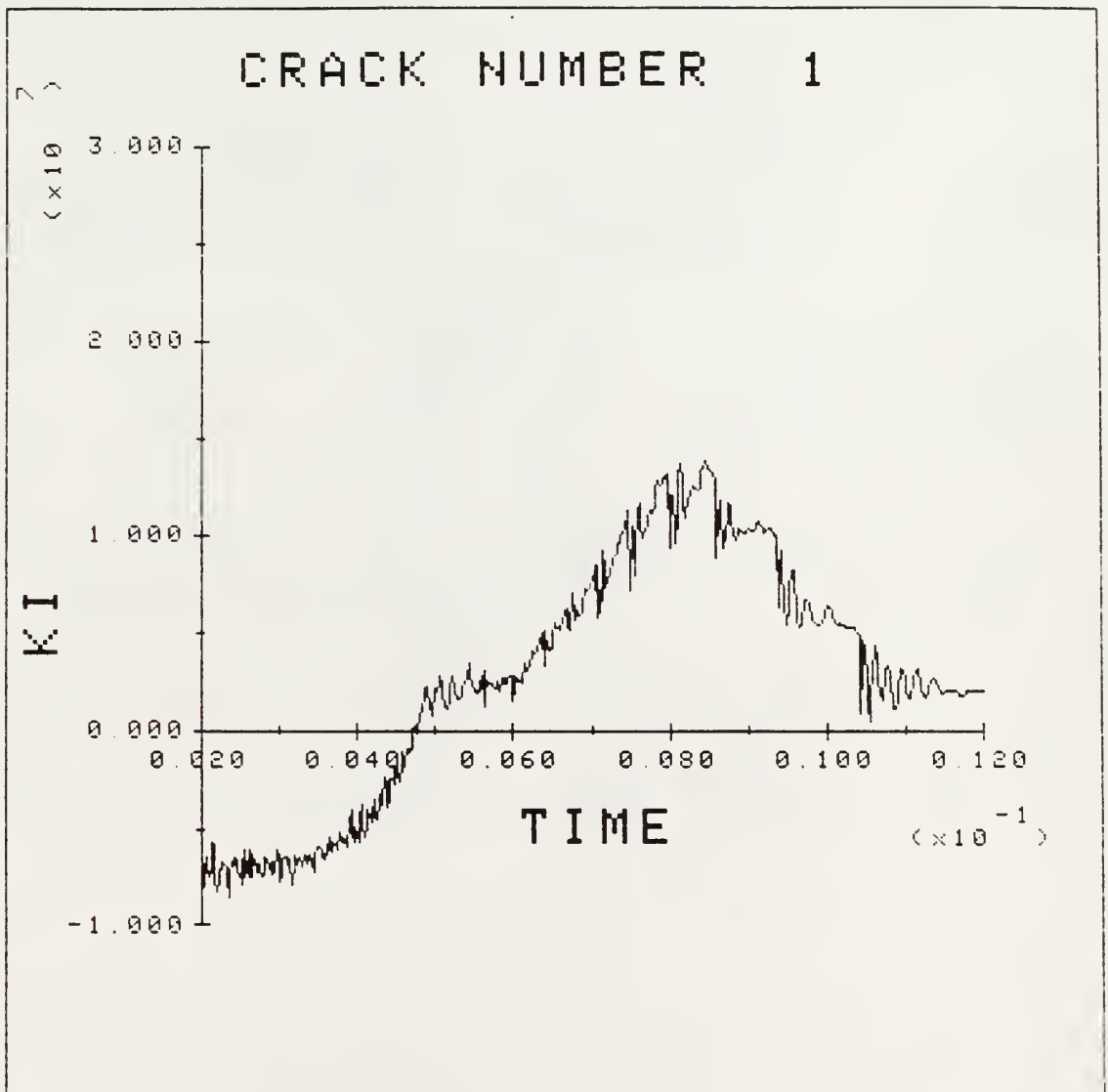


Figure 5.57: KID During Propagation for Case 5

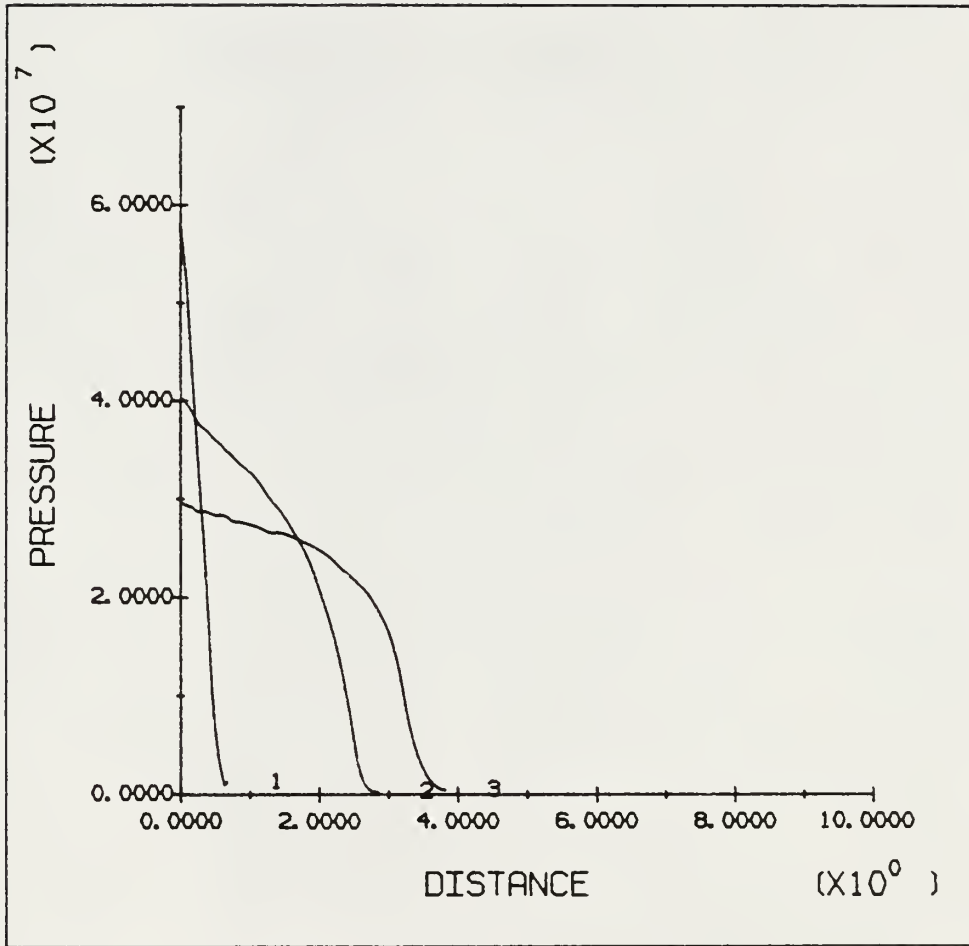


Figure 5.58: Gas Pressure for Case 5 at 6.5, 9.5, and 12 msec

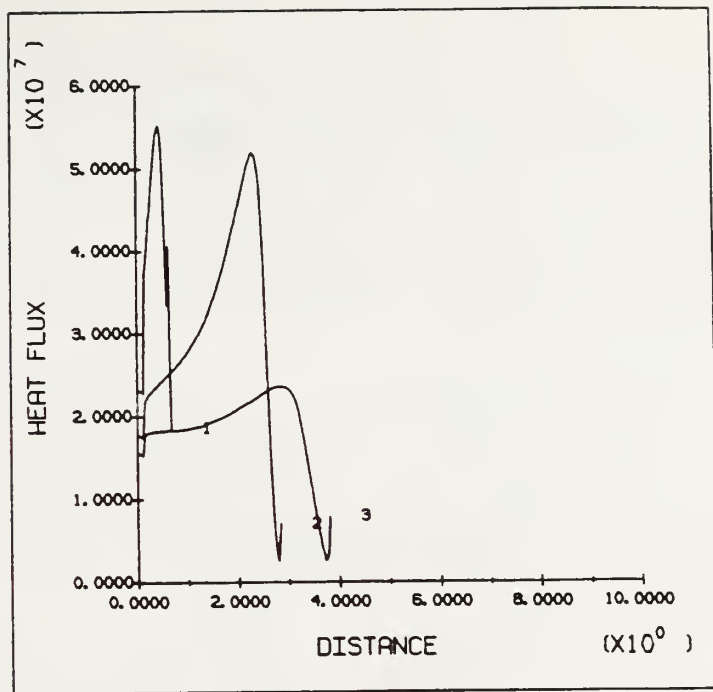


Figure 5.59: Heat Flux for Case 5 at 6.5, 9.5, and 12 msec

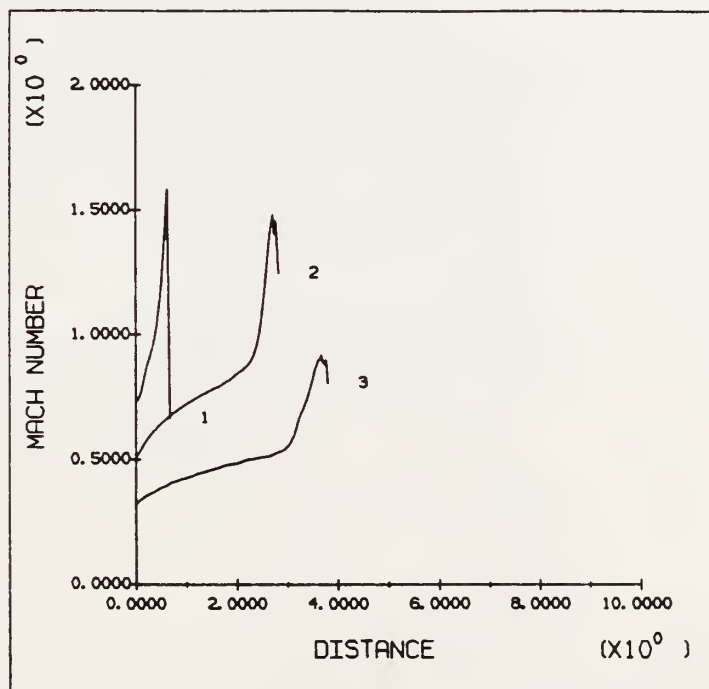


Figure 5.60: Mach Number for Case 5 at 6.5, 9.5, and 12 msec

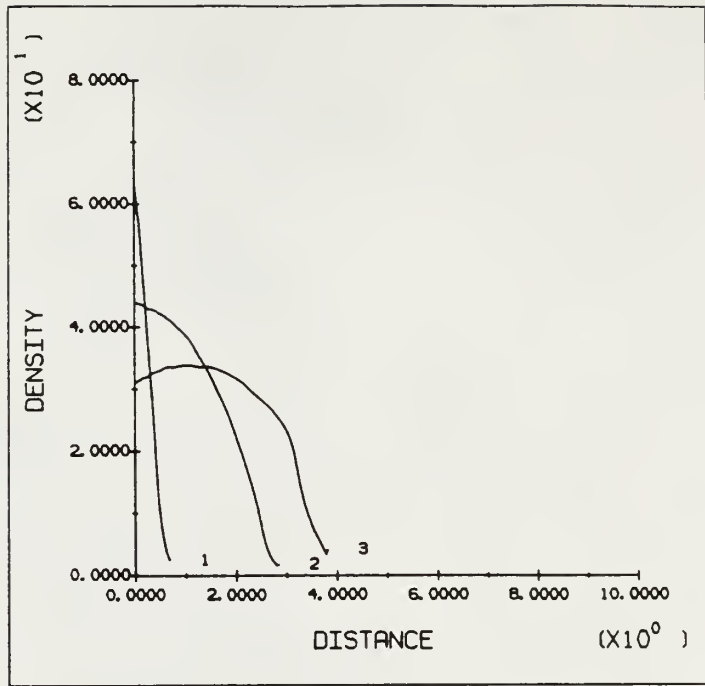


Figure 5.61: Gas Density for Case 5 at 6.5, 9.5, and 12 msec

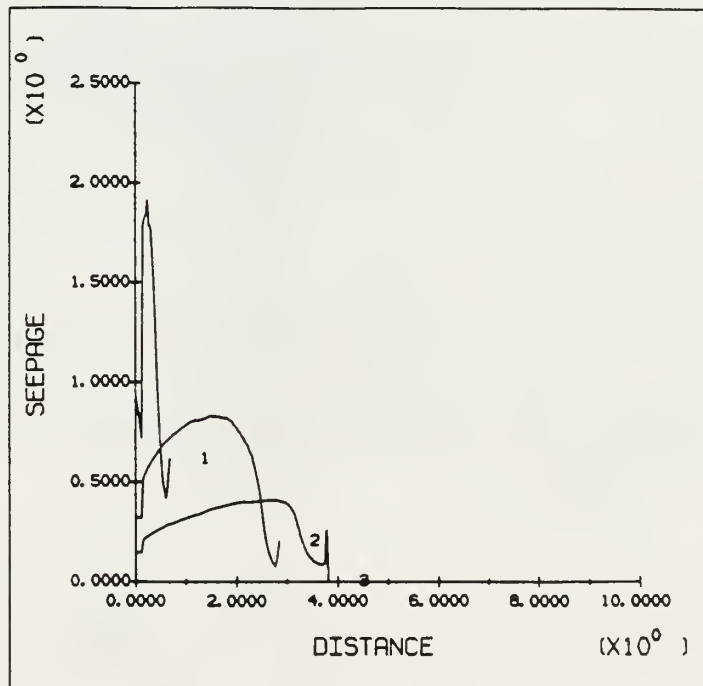


Figure 5.62: Gas Seepage for Case 5 at 6.5, 9.5, and 12 msec

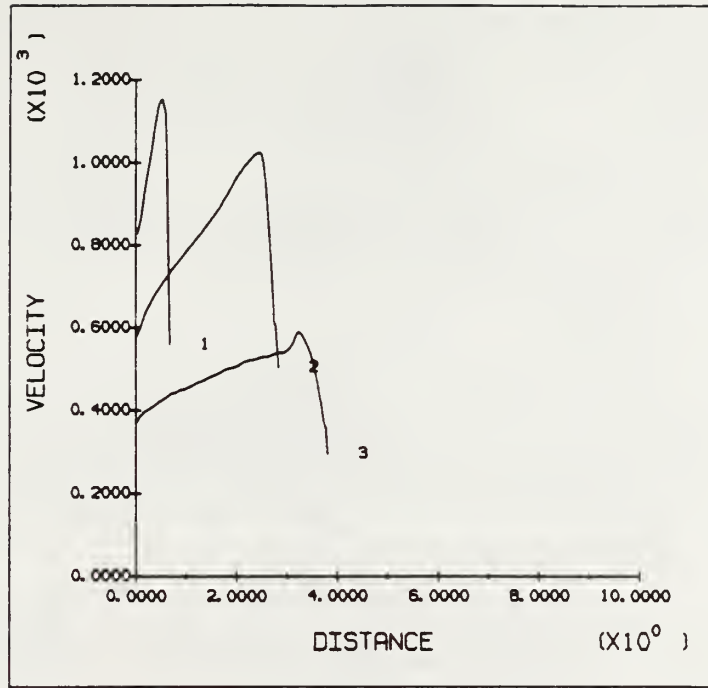


Figure 5.63: Gas Velocity for Case 5 at 6.5, 9.5, and 12 msec

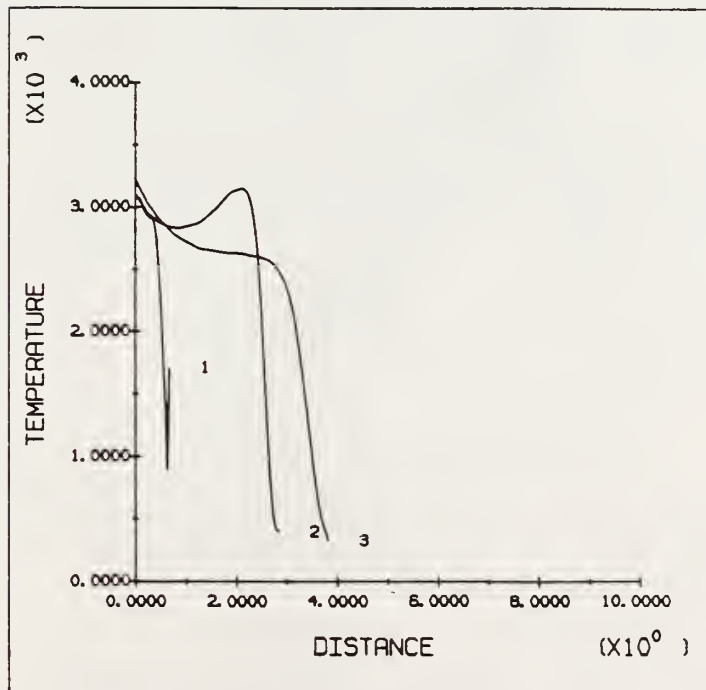


Figure 5.64: Gas Temperature for Case 5 at 6.5, 9.5, and 12 msec

Figure 5.65 shows the crack entrance energy plot for Case 5 at 12 msec. Since its slope is less than that for Case 2, it seems that less of the available energy is converted to kinetic energy than is the case for Case 2. For about the same crack length as found in Case 2, about 26% less energy was required.

For Case 5, the maximum crack tip velocity was approximately 500 m/sec. To have a successful stimulation of 100 meters, the crack will need to be driven at least 200 msec. Figure 5.55, in addition to experimental data (Schmidt et al, 1981), illustrates that this 200 msec driving time will not be the result of using conventional propellants alone.

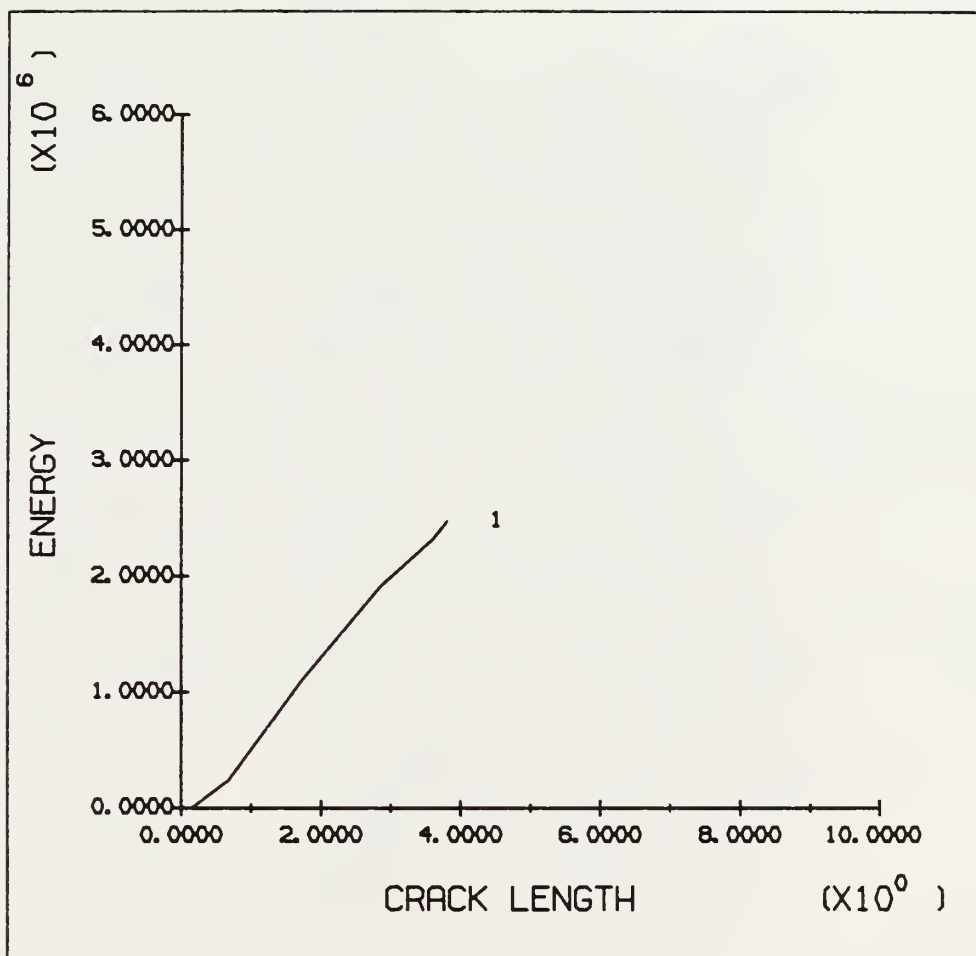


Figure 5.65: Crack Entrance Energy for Case 5

CHAPTER 6

CONCLUSIONS AND RECOMMENDATIONS

6.1 Conclusions

Cases 1 through 4 allowed us to compare the effects of changing parameters. The most striking result is the large effect of friction, seepage, and heat transfer. Without these losses, the gas flow into the crack drives the crack at the limiting speed of the rock and would lead to bifurcation. When the losses are included, gas flow into the crack is reduced. This reduced flow limits the crack velocity to the range of 500-600 m/sec. From this, we can estimate the necessary pressure loading time to drive a fracture a given length.

The analysis using a propellant (Case 5) allows comparison with field tests and the work of Nilson and Hanson. The most significant result is that the predicted crack length is approximately 4 meters. This is much smaller than the 100-200 meter length envisioned for successful stimulation. This fracture length is consistent with experimentally observed lengths. As was mentioned earlier, no field test has resulted in a fracture longer than 10 meters. Our results from Case 5 agree with this experimental result. Nilson (et al., 1985) agrees with this result to a large degree.

These calculations and supporting experiments show that long fractures cannot be obtained by simple propellant burns. The energy stored in the propellant is only sufficient to drive short fractures. As illustrated in Case 5, the crack velocity and K_{TD} both started to decrease after the propellant was past its peak pressure. To maintain

crack growth, the borehole pressure would need to be sustained and not allowed to drop.

One possible solution would be to use additional propellant (or other stored energy source) above the region being stimulated. This would allow sufficient energy to be supplied and would maintain the borehole pressure at a high level.

6.2 Recommendations For Future Work

Since the pressure loading on the crack is the dominate feature of the tailored pulse stimulation technique, more work should be applied to the gas model solution algorithm. With the current method (Lax), it was necessary to apply damping and a time reduction factor. To avoid this, other solution methods such as upwind differencing, Lax-Wendroff, and staggered leapfrog should be considered. Finite element implementation is also a possibility.

To model a complete problem, a full model geometry with the borehole in the center should be used. This would allow the use of unsymmetrical in-situ stresses, and therefore allow crack curvature to occur. With this type of model geometry, a complete multiple fracture analysis can be accomplished.

In addition to the more complete model geometry, more parameter studies should be conducted. The effects of different:

1. in-situ stresses,
2. permeabilities,
3. and propellants

should be considered.

REFERENCES

1. Ames, W.F., 1977, Numerical Methods for Partial Differential Equations, 2nd ed., Academic Press, New York.
2. Fournery ,W.L., D.B. Barker and D.C. Holloway, 1983, "Model Studies of Well Stimulation Using Propellant Charges," Int. J. Rock Mech. Min. Sci. & Geomech. Abstr., Vol 20, 91-101.
3. Fournery ,W.L., D.B. Barker and D.C. Holloway, 1981, "Model Studies of Explosive Well Stimulation Techniques," Int. J. Rock Mech. Min. Sci. & Geomech. Abstr., Vol 18, 113-127.
4. Griffiths, S.K., Nilson, R.H., and Morrison, F.A., 1986, "Hybrid Analytical/Numerical Computation of Heat Transfer in a Gas-Driven Fracture, "Journal of Heat Transfer, Vol. 108, 585-590.
5. Halter, K.E., "A Fast Solver for Riemann Problems, 1985, "Math. Meth. in the Appl. Sci., Vol 7, 101-107.
6. John, J.E., 1984, Gas Dynamics, 2nd ed., Allyn and Bacon, Inc, Boston, MA.
7. Mniszewski, K. and Napadensky, H., "The Characterization of High Energy Chemical Sources For Fracturing Of Devonian Shale," Final report prepared by ITT Research Institute, Chicago, IL., and submitted to Gas Research Institute, Chicago, IL.
8. Nilson, R.H. and Griffiths, S.K., 1986, "Similarity Analysis of Energy Transport in Gas-Driven Fractures," International Journal of Fracture, 30, 115-134.
9. Nilson, R.H., Proffer, W.J., and Duff, R.E., 1985, "Modelling of Gas-Driven Fractures Induced by Propellant Combustion Within a Borehole," Int. J. Rock Mech. Min. Sci. & Geomech. Abstr., Vol. 22, No. 1, 3-19.
10. Press, W.H., Flannery, B.P., Teukolsky, S.A., Vetterling, W.T., 1986, Numerical Recipies, Cambridge University Press.
11. Rogiers, J.C., Dowell Schlumberger, Tulsa, Oklahoma, conversation with Daniel Swenson, April 1987.
12. Schatz, J.F., Bennett, J.Z., Bellman, R.A., and Hanson, J.M.(Consultant)., "Prediction and Interpretation of Multiple Radial Fracture Stimulations," Final report prepared by ITASCA Consulting Group, San Diego, CA., and submitted to Gas Research Institute, Chicago, IL.

13. Schlichting, H., 1979, Boundary-Layer Theory, 7th ed., McGraw-Hill.
14. Schmidt, R.A., Warpinski, N.R., Finley, S.J., and Shear, R.C., "Multi-Frac Test Series Final Report," SAND81-1239, Sandia National Laboratories, Albuquerque, NM, November, 1981.
15. Sneddon, I.N. and Lowengrub, M., 1969, Crack Problems in the Classical Theory of Elasticity, John Wiley, New York.
16. Sod, G.A., 1978, "A Survey of Several Finite Difference Methods For Systems of Nonlinear Hyperbolic Conservation Laws," J. Computational Phys., Vol 27.
17. Swenson, D.V., and Taylor, L.M., 1983, "A Finite Element Model For The Analysis Of Tailored Pulse Stimulation Of Boreholes," International Journal for Numerical & Analytical Methods in Geomechanics, Vol 7, 469-484.
18. Swenson, D.V., "Modeling Mixed-Mode Crack Propagation Using Finite Elements," Dept. of Structural Engineering Report, Number 85-10, Cornell University, Ithaca, NY.
19. Swift, R.P. and Kusubov, A.S., "Tailored-Pulse Loading Conditions For Multiple Fracturing Of Boreholes," presented at the 22nd U.S. Symposium on Rock Mechanics, MA, June 29-July 2, 1981.

A NUMERICAL MODEL OF GAS-DRIVEN
DYNAMIC FRACTURES WITH AN APPLICATION
TO BOREHOLE STIMULATION

BY

JEFFERY M. ROBERTS
B.S. Emporia State University

AN ABSTRACT OF A MASTER'S THESIS

submitted in partial fulfillment of the
requirement for the degree

MASTER OF SCIENCE

Department of Mechanical Engineering
KANSAS STATE UNIVERSITY
Manhattan, Kansas

1988

ABSTRACT

Gas-driven fractures are of practical importance in the stimulation of gas and oil wells, rock blasting with explosives, and the containment of nuclear explosions. There is at present no general analytical tool to predict the fracture length and propagation direction under transient loading conditions.

We develop a coupled model of gas-driven dynamic fracture and use the model to analyze well stimulation. The model consists of two parts: (1) a finite element model used to calculate dynamic crack propagation, and (2) a finite difference model of compressible, dynamic gas flow. The finite element model assumes that the fractures are discrete parts of the mesh, with automatic remeshing performed as the cracks propagate. The compressible gas model is developed using the conservation of mass, energy, and momentum equations. Losses due to friction, seepage of the gas into the crack walls, and heat transfer to the walls are included in the analysis.

Results clearly show the importance of the loss terms. With losses included, the crack speed is limited by gas flow into the fracture. Calculations using a propellant burn model give a predicted crack length of 4 meters, which correlates with observed field tests.

